Optical Antennas for Biosensing Applications

Dissertation for the acquisition of the academic degree

Doktor der Ingenieurwissenschaften (Dr.-Ing.)

Submitted to the Faculty of Electrical Engineering and Computer Science

of the University of Kassel

Germany

By Abdul Aleem Jamali, M.Sc.

Kassel, March 2015

Erklärung

Hiermit versichere ich, dass ich die vorliegende Dissertation selbstständig, ohne unerlaubte Hilfe Dritter angefertigt und andere als die in der Dissertation angegebenen Hilfsmittel nicht benutzt habe. Alle Stellen, die wörtlich oder sinngemäß aus veröffentlichten oder unveröffentlichten Schriften entnommen sind, habe ich als solche kenntlich gemacht. Dritte waren an der inhaltlich-materiellen Erstellung der Dissertation nicht beteiligt; insbesondere habe ich hierfür nicht die Hilfe eines Promotionsberaters in Anspruch genommen. Kein Teil dieser Arbeit ist in einem anderen Promotions- oder Habilitationsverfahren verwendet worden.

March 25, 2015

Kassel, Germany .....

(Abdul Aleem Jamali)

Eingereicht am:	March 25, 2015
Tag der mündlichen Prüfung:	June 09, 2015
Gutachter:	Professor Dr. sc. tech. Bernd Witzigmann
	Professor Dr. Arno Ehresmann
Promotionskommission:	Professor Dr. sc. tech. Bernd Witzigmann
	Professor Dr. Arno Ehresmann
	Prof. Dr. rer. nat. habil. Hartmut Hillmer
	Prof. Dr.-Ing. habil. Peter Lehmann

Abstract

The aim of the thesis is to theoretically investigate optical/plasmonic antennas for biosensing applications. The full 3-D numerical electromagnetic simulations have been performed by using finite integration technique (FIT). The electromagnetic properties of surface plasmon polaritons (SPPs) and the localized surface plasmons (LSPs) based devices are studied for sensing purpose. The surface plasmon resonance (SPR) biosensors offer high refractive index sensitivity at a fixed wavelength but are not enough for the detection of low concentrations of molecules. It has been demonstrated that the sensitivity of SPR sensors can be increased by employing the transverse magneto-optic Kerr effect (TMOKE) in combination with SPPs. The sensor based on the phenomena of TMOKE and SPPs are known as magneto-optic SPR (MOSPR) sensors. The optimized MOSPR sensor is analyzed which provides 8 times higher sensitivity than the SPR sensor, which will be able to detect lower concentration of molecules. But, the range of the refractive index detection is limited, due to the rapid decay of the amplitude of the MOSPR-signal with the increase of the refractive indices. Whereas, LSPs based sensors can detect lower concentrations of molecules, but their sensitivity is small at a fixed wavelength. Therefore, another device configuration known as perfect plasmonic absorber (PPA) is investigated which is based on the phenomena of metal-insulator-metal (MIM) waveguide. The PPA consists of a periodic array of gold nanoparticles and a thick gold film separated by a dielectric spacer. The electromagnetic modes of the PPA system are analyzed for sensing purpose. The second order mode of the PPA at a fixed wavelength has been proposed for the first time for biosensing applications. The PPA based sensor combines the properties of the LSPR sensor and the SPR sensor, for example, it illustrates increment in sensitivity of the LSPR sensor comparable to the SPR and can detect lower concentration

of molecules due to the presence of nanoparticles.

Zusammenfassung

Das Ziel dieser Arbeit ist die theoretische Untersuchung von optischen/plasmonischen Antennen in Bezug auf deren Anwendung in der Biosensorik. Hierzu wurden dreidimensionale numerische Elektromagnetiksimulationen unter Verwendung der finiten Integrationstechnik (FIT) durchgefü hrt. Untersucht wurden die elektromagnetischen Eigenschaften von Sensoren, die auf Oberflächenplasmonen- (SPPs) bzw. lokalisierten Oberflächenplasmonen (LSPs) basieren. Biosensoren, die Oberflächenplasmonresonanzen (SPR) ausnutzen bieten bei einer festgelegten Wellenlänge eine sehr hohe Sensitivitt, sind jedoch nicht in der Lage geringere Molekülkonzentrationen zu detektieren. Es wurde gezeigt, dass die Sensitivität von SPR-Sensoren erhöht werden kann, wenn der transversale magnetooptische Kerr-Effekt (TMOKE) in Kombination mit SPPs genutzt wird. Sensoren, die auf diesem Prinzip beruhen werden als magnetooptische SPR (MOSPR) Sensoren bezeichnet. Die Analyse dieser optimierten MOSPR-Sensoren zeigten eine achtfach höhere Sensitivität als die SPR-Sensoren und sind somit geeignet auch geringere Molekülkonzentrationen zu detektiern. Jedoch ist der Bereich für die brechungsindexbasierte Detektion beschränkt, aufgrund eines schnellen Abfalls in der MOSPR-Signalamplitude fr ansteigende Brechungsindizes. Während LSP basierte Sensoren in der Lage sind geringe Molekülkonzentrationen zu detektieren, zeigen sie nur eine schwache Sensitivität bei einer festen Wellenlänge. Daher wurde eine weitere Sensorkonfiguration untersucht, die plasmonic perfect absorber (PPA) genannt wird und auf dem Prinzip eines Metall-Isolator-Metall (MIM) Wellenleiters beruht. Ein PPA besteht aus einer periodischen Anordnung von Goldnanopartikeln und einer dicken Goldschicht, die durch ein Dielektrikum getrennt sind. Die elektromagnetischen Moden eines solchen PPA wurden bezglich ihrer Sensortauglichkeit untersucht. Der PPA basierte Sensor bietet eine

erhöhte Sensitivität gegenüber den LSPR-Sensoren und ist darüber hinaus aufgrund der Verwendung von Nanopartikeln in der Lage eine geringe Anzahl von Molekülen zu detektieren. Somit vereint das PPA-Prinzip die Vorteile der beiden zuvor beschriebenen Sensorkonfigurationen.

Acknowledgments

I am sincerely thankful to all those peoples who helped, supported and motivated me during my research work.

I am grateful to Prof. Dr. sc.techn. Bernd Witzigmann for giving me the opportunity to carry out my research work at the Computational Electronics and Photonics (CEP) group. He has played a very important role by guiding me during my research work and by motivating me for better results. I would like to thank him personally for his support and enthusiastic role.

I would also like to thank personally to Prof. Dr. Arno Ehresmann for evaluating my thesis as a second reviewer. I am also thankful to other examiners, Prof. Dr. rer. nat. habil. Hartmut Hillmer and Prof. Dr.-Ing. habil. Peter Lehmann.

Moreover, I wish to thank to the whole team of the group Mrs. Regina Brylla, Dr.-Ing. Klaus Mayer, Dr.-Ing. Friedhard Römer, Dr.-Ing. habil. René Marklein, Mr. Daniel Bischof, M. Sc. Marko Bjelica, M. Sc. Andreas Engelhardt, M. Sc. Kristian Frank and M. Sc. Akshay, Shedbalkar. I am also thankful to the former group members Prof. i. R. Dr. Karl J. Langenberg, Dr. Felix Voigt, Dipl.-Ing. Yanna Mikhilina, Dipl.-Ing. Ugur Akcakoca, M. Sc. Zhelio Andreev, Dipl.-Ing. Gregor Ballier, Dr. Prashanth Kumar Chinta, Dr. Marcus Deppner, Dr. Mehbub-ur Rahman and Dr. Shuqing Yu for their cooperation.

Last but not the least, I would like to acknowledge my parents, brothers, sisters and especially my wife for their constant love and support.

Contents

List of Figures

List of Abbreviations

ADDL	Amyloid Derived Diffusible Ligand
ATR	Attenuated Total Reflection
CEA	Carcinoembryonic
CEM	Computational Electromagnetics
CFL	Courant-Friedrich-Levy
cTn	Cardiac Troponin
DE	Differential Equation
DNA	Deoxyribonucleic Acid
EM	Electromagnetic
FD	Finite Difference
FDTD	Finite Difference Time Domain
FEM	Finite Element Method
FIT	Finite Integration Technique
fM	Femtomolar
FWHM	Full Width at Half Minimum
GFR	Glomerular Filtration Rate
hHBV	Human Hepatitis B Virus
Ig	Immunoglobulin

LSP	Localized Surface Plasmon Polariton
LSPR	Localized Surface Plasmon Resonance
MIM	Metal-Insulator-Metal
MO	Magneto-Optic
MOKE	Magneto-Optic Kerr Effect
MOSPR	Magneto-Optic Surface Plasmon Resonance
nM	Nanomolar
PBC	Periodic Boundary Condition
PBS	Phosphate-Buffered Saline
pM	Picomolar
PML	Perfectly Matched Layer
PPA	Plasmonic Perfect Absorber
PSP	Propagating Surface Plasmon
RF	Radio Frequency
RI	Refractive index
RIU	Refractive Index Unit
SCCa	Squamous Cell Carcinoma Antigen
SERS	Surface Enhanced Raman Spectroscopy
SP	Surface Plasmon
SPP	Surface Plasmon Polariton
SPR	Surface Plasmon Resonance
TE	Transverse Electric
TM	Transverse Magnetic
TMM	Transfer Matrix Method

Chapter 1

Introduction

1.1 Introduction

Over the last two decades optical biosensors have been thoroughly explored in research laboratories for their remarkable applications such as to detect colorectal cancer marker carcinoembryonic antigen (CEA) with a detection limit of 0.5 ng/mL using a commercial SPR sensor Autolab Springle (1).

Optical antennas are booming as the state-of-the-art technology in the research of biosensors for real-time and label-free detection of biochemical interactions (2). They are designed for the efficient conversion of optical radiation to the localized energy, and vice versa (3). Optical antennas are different from RF and microwave antennas in their physical properties and scaling behavior. At optical frequencies metals act as strongly coupled plasmas (3). Optical antennas are metallic nanostructures operating in the visible and near-infrared regime also known as plasmonic antennas. Surface plasmons are oscillations of free conduction electrons at the metal-dielectric interface excited by optical waves (3). Properties of optical antennas are strongly dependent on the geometry and material properties of the nanoparticle and the surrounding medium, due to resonance of surface plasmons (4). Figure 1.1, shows a comparison of a classical antenna and an optical/plasmonic antenna (4). Surface plasmons are usually categorized in to surface plasmon polaritons (SPPs) and localized surface plasmons (LSPs). The SPPs are excited at the interface of planar metal and dielectric layers, whereas,

the LSPs are excited at the interface of metal and dielectric nanoparticles (5). The plasmonic resonances are highly dependent on the dimension and material properties of both the metal and the dielectric medium in its vicinity (5). The strong dependence on the surrounding dielectric medium is utilized for biosensing.

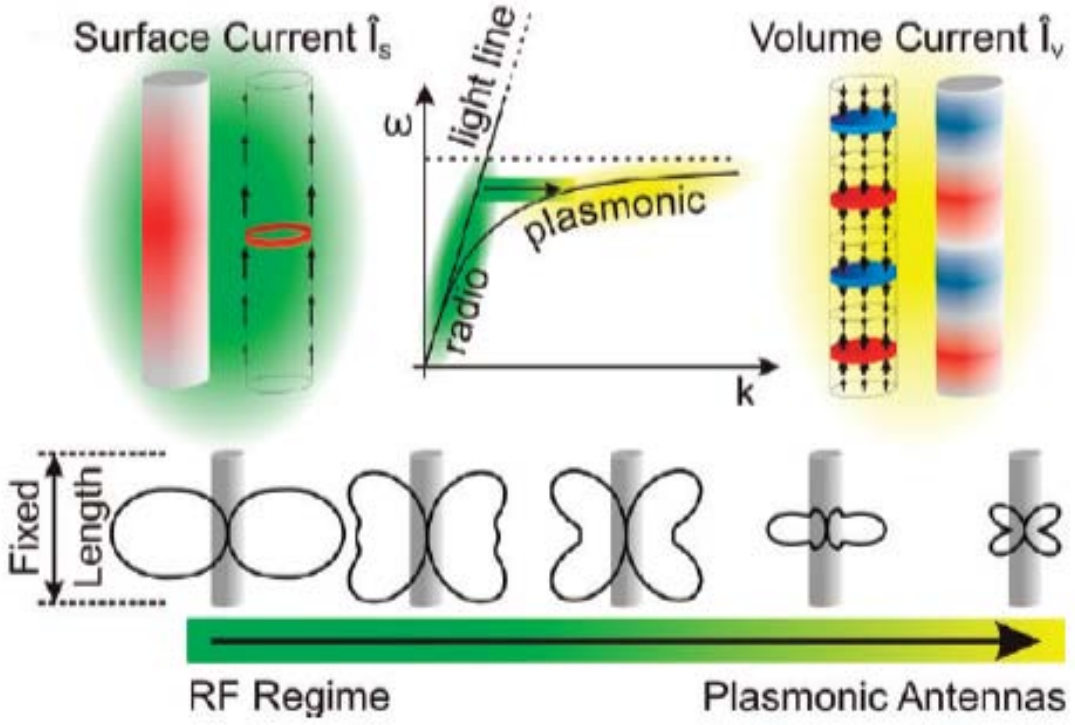

Figure 1.1: Difference in RF and plasmonic antenna theory. RF antenna with a surface current (left) and plasmonic antenna with a volume current (right) leading to shorter wavelength which can be seen in the dispersion relation (center). Transformation of fixed RF antenna to plasmonic antenna leads to different radiation patterns (bottom)[Reprinted (adapted) with permission from (4). Copyright (2010) American Chemical Society].

The surface plasmon resonance (SPR) biosensor is based on the phenomena of SPPs. Let us consider a SPR setup in Kretschmann configuration (6), as shown in Fig. 1.2. When *p*- polarized light is illuminated through a prism on a thin metal film, the incident light will be reflected by the metal layer. The metal layer acts as a mirror and the intensity of the reflected light is observed at the detector. By varying the incident angle of the light, minimum in the reflected intensity can be observed by the detector. The dip in the reflected intensity at the incident angle is caused due to the excitation of SPPs by the light. SPPs are

TM waves propagating along the metal-dielectric interface and are excited with the coupling of the incident light and oscillation of free conduction electron of the metal layer (7). The incident angle of light at which the reflected intensity becomes zero is called resonant angle or SPR angle. The position of the resonance angle is dependent on the optical properties of the SPR sensor, such as the refractive index of the dielectric medium adjacent to the metal layer (Fig. 1.2). The change in the refractive index of the dielectric medium changes the resonance condition of the SPPs, hence the resonance occurs at different incident angle of light. By this way, the refractive index change of the dielectric medium can be detected with the shift of the resonance angle. The intensity modulation sensitivity of a Kretschmann configuration based SPR sensor is 39 RIU^{-1} at $\lambda = 630\ nm$ and 150 RIU^{-1} at $\lambda = 850\ nm$ (8). Even though the sensitivity of this type of SPR sensor is very high, is still not enough for low concentrations of biomolecules ($< 1\ ng/mL$) (7). For this reason, several approaches have been used to improve the sensitivity using patterned metal nanoparticles for localized surface plasmon resonance (LSPR) (9; 10; 11), grating structures (8), the combination of SPR with magneto-optic Kerr effect (MOKE) (12; 13), and the latter is also combined with the patterned LSPR (14; 15; 16; 17; 18).

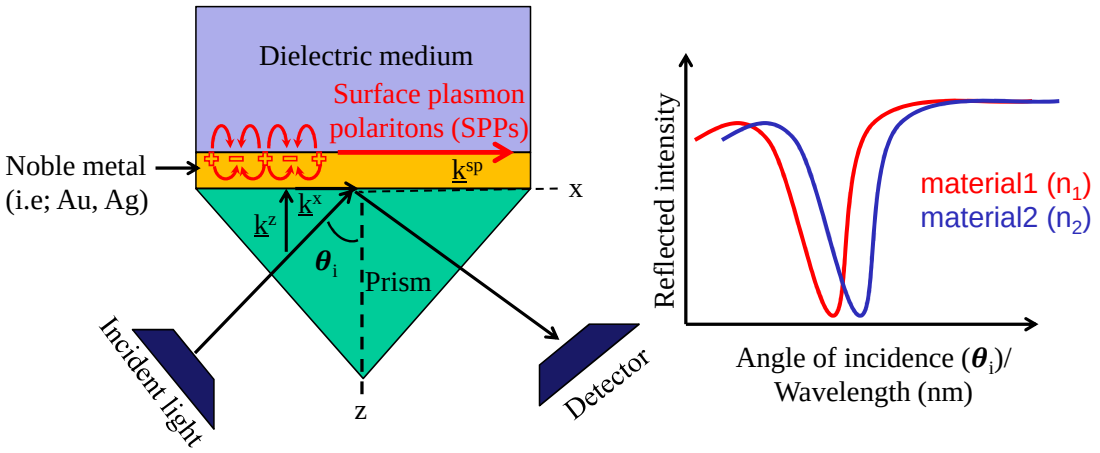

Figure 1.2: Representation of the surface plasmon resonance (SPR) system in Kretschmann configuration.

A new modulation technique has been employed which demonstrates three fold increment in the sensitivity of the standard SPR sensor (19). This technique combines the magneto-

optic (MO) activity of magnetic materials with external magnetic field and the SPR of the metallic layers; this combined effect is known as magneto-optic SPR (MOSPR) (12). The combination of the magnetic materials and metallic layers can create a sharp enhancement of the magneto-optic effects that highly depends on the optical properties of the adjacent dielectric medium, making it a suitable candidate for biosensing (12).

Localized surface plasmon resonance (LSPR) biosensors are based on the phenomena of LSPs. The surface plasmons of LSPR sensors are excited locally to the nanostructures, unlike the SPR sensors, where surface plasmons are excited at the planar metal-dielectric interfaces. The excitation of localized surface plasmon resonance (LSPR) on metallic nanoparticles results in the strong enhancement of the electromagnetic fields and the efficient scattering of electromagnetic radiation (20). Localized plasmon modes on nanoparticles are dependent on the size, shape and the surrounding dielectric medium. Therefore several structures of nanoparticles have been studied such as nanospheres (21), nanorods (22), nanodisks (23), nanocubes (24), and triangular nanoprims (25). Based on these characteristics, plasmonic nanoparticles are used for biosensing applications in optical and in near infrared regimes. In the applications of sensor and detector, a single and sharp resonance is required in the extinction spectrum. Changes in bulk refractive index of dielectric environment is detected through the shifts in the LSPR peak wavelength, which is given by the measurement of spectral extinction as shown in Fig. 1.3. The sensing performance of the LSPR sensors can be optimized by varying the size and shape of the nanoparticles (2). The LSPR sensors have been used for detecting smaller concentration of molecules in the range of zeptomole (26), but have very less wavelength interrogation sensitivity as compared to the SPR sensors (SPR sensitivity $= 2 \times 10^6\ nm\ RIU^{-1}$; LSPR sensitivity $= 2 \times 10^2\ nm\ RIU^{-1}$) (27). The other advantage of LSPR sensors to be more cost effective than the SPR sensors (cost of SPR sensors$->$ US \$ $150{,}000 - 300{,}000$; cost of LSPR sensors $->$ US \$ $5000 - 50{,}000$) (27).

Recently Liu et al. (28) and Li et al. (29) have demonstrated a novel device known as plasmonic perfect absorber for sensing application in infrared regime. The perfect absorber is composed of periodically arranged metallic nanoparticles on a gold layer separated by a dielectric spacer. The technique is based on the combination of LSPR and SPR effects. This

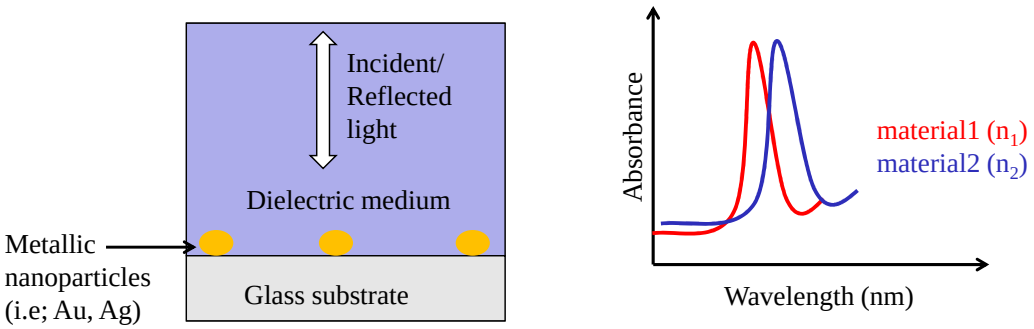

Figure 1.3: Representation of the localized surface plasmon resonance(LSPR) system.

work has motivated me to analyze the plasmonic perfect absorber for biosensing. The key idea of this research is to utilize the plasmonic perfect absorber setup for biosensing which combine the sensing properties of the LSPR and SPR sensor. The proposed novel approach provides a narrow band perfect optical absorber which will not only provide high sensitivity but can also be able to detect lower concentrations of biomolecules. In this thesis, gold (Au) noble metal is used as a potential metal for the excitation of surface plasmons, as it supports strong surface plasmons at the resonance wavelength and its surface is proved to be oxide free (30).

1.2 Current state of plasmonic biosensing

The intensive study of plasmonic antenna has started in the mid of 20th century by connecting theoretical assumptions and the existing experiments. The propagating and localized surface plasmons can be distinguished easily, yet both are excited by the interaction of light and matter.

In 1902, the anomalous diffraction from metal gratings was discovered by Wood (31), his work can be considered as a milestone in the research on propagating plasmons. Ritchie (32) in 1957 was the first to predict the existence of surface plasmons in metallic thin films. Powell and Swan (33) in 1959 demonstrated the characteristic of electron energy loss in metal which

corresponds to the generation of surface plasmons. In 1968 Ritchie et al connected the phenomena of surface plasmons with Woods anomaly, described the surface plasmon resonance effect in grating diffraction (34). The prism coupled optical excitation of surface plasmon was experimentally performed by Kretschmann and Raether (6) and then by Otto (35) in 1968.

First theoretical investigation of localized surface plasmons was carried out by Lorenz (36) in 1898 and then by Mie in 1908 (37). In 1970, Kreibig and Zacharias (20) has demonstrated the excitation of resonances in small noble metal particles. The first surface enhanced Raman spectroscopy (SERS) experiment in 1974 (38) has demonstrated the Raman spectra of pyridine adsorbed at a silver electrode for sensing application.

Liedberg et al (39) in 1983 have demonstrated the use of SPR phenomena for detecting the antibody human Immunoglobulin (IgG) in water solution. Since then, this technique has been used for the detection of biospecific interaction of biomolecules by different groups (40; 41). Wei et al. reported the monitoring of cardiac troponin (cTn I) biomarker for the detection of cardiac muscle injury in serum with in a detection limit range of 2.5 ng/mL using a fiber optic SPR sensor (42). In 2004, the commercial SPR sensor Ibis II has been investigated for the detection of prostate cancer by monitoring prostate-specific antigen (PSA) in PBS buffer solution with a limit of detection of 0.15 ng/mL (43). The commercial SPR sensor Spreeta has been used for the detection of antibodies against human hepatitis B virus (hHBV) in 5 % serum in PBS with a limit of detection of 9.2 nM (44). Detection of Colorectal cancer has been reported by monitoring Carcinoembryonic antigen (CEA) with a detection limit of 0.5 ng/mL using a commercial SPR sensor Autolab Springle (1). In 2006, SPR imaging instrument has been used to detect cystatin C protein biomarker of glomerular filtration rate (GFR) for the measure of proper functioning of kidney with a detection limit of 1 nM range (45). In 2014, Jahanshai et al. reported the detection of anti-dengue virus by monitoring immunoglobulin M (IgM) in serum volume of 1 μl by using BIAcore 3000 SPR system (46).

The LSPR sensors are used for label-free detection of biomolecules. One of the major applications of LSPR biosensors is the detection of small biomolecules, as the dimension

$(2 - 20\ nm)$ of bioreceptors such as enzymes, antibodies, and antigens are dimensionally compatible with the nanostructures of LSPR sensors (26). In 2007, Kim et al. reported a label-free detection of synthetic target DNA with a detection limit of 10 pM by using LSPR coupled with the Interferometry in a porous anodic alumina (PPA) layer chip (47). LSPR based chip has been proposed to monitor insulin and anti-insulin antibody immunoreactions in real-time with a detection limit of 100 ng/mL for detecting insulin level that is required for diagnosis of diabetes (48). Alzheimer disease has also been proposed to detect with LSPR biosensors, where the interaction between amyloid β-derived diffusible ligands (ADDL) and the anti-ADDL antibody are monitored by using Ag nanoparticles (49; 50). In 2014, tumor biomarker i.e., squamous cell carcinoma antigen (SCCa) has been proposed to detect with reusable and label-free LSPR based biosensor (51). The SCCa is used for diagnosis, treatment evaluation, and prognosis predication for cervical cancer. In this work, a triangle-shaped silver nanoparticle array is used in the LSPR system to test buffer and human serum with a detection range of $0.1 - 1000\ pM$ under optimal conditions.

1.3 Objective of the research

The main objective of the research is to theoretically investigate the sensitivity of the optical/plasmonic biosensor for the analysis of small concentrations of biomolecules. The SPR biosensors offer high sensitivity but are not capable of detecting the small concentrations of biomolecules. Whereas, the LSPR biosensors are capable of detecting smaller concentrations of molecules but have less sensitivity. It is useful to combine the properties of SPR and LSPR for biosensing. Therefore, the aim of this thesis is to design a plasmonic biosensor and develop a strategy so that it presents high sensitivity and allows the detection of few molecules.

1.4 Methodology

The Finite Integration Technique (FIT) is used as a numerical method for full 3-D electromagnetic simulations. It gives precise algebraic analogues of Maxwell's equations in their

integral form. The algebraic equations ensure that physical properties of electromagnetic fields are in discrete space, and result in a unique solution (52).

1.5 Outline of the thesis

The purpose of this thesis is to thoroughly investigate the plasmonic devices for biosensing applications. Full 3-D electromagnetic simulations have been performed by using finite integration technique. We study the 3-D electromagnetic properties of the SPPs and LSPs based devices. A novel approach has been given in this thesis for sensing by utilizing the properties of the SPP and LSP based sensors. This thesis is organized as follows. Chapter 2 summarizes the theoretical background of the electromagnetic theory required in this thesis. It starts from the Maxwell's equations to the description of surface plasmons. It also includes the short description of the finite integration technique (FIT). Chapter 3 analyzes the properties of the surface plasmon resonance (SPR) sensor for biosensing applications. The excitation of the surface plasmon polaritons in the Kretschmann configuration is studied. The angular sensitivity of the device is examined for biosensing purpose. Chapter 4 studies the properties SPR sensor by including the magneto-optic (MO) effect for biosensing applications. The magneto-optic SPR (MOSPR) system is formed by sandwiching the ferromagnetic layer in between the two gold layers. External magnetic field is applied to the ferromagnetic medium to modulate the properties of the SPR. The intensity modulation sensitivity technique is utilized for biosensing. Chapter 5 investigates the properties of the plasmonic perfect absorbers (PPA) for biosensing. The PPA consists of three layer which include 2-D periodic array of metallic nanodisks, dielectric spacer, and thick metal layer. The excited modes in the PPA system are analyzed in this chapter for biosensing purpose. Finally, Chapter 6 summarizes the conclusion and give the outlook of the work.

Chapter 2

Theoretical Background

The classical theory of electromagnetics based on Maxwell's equations describes the wave propagation in the optical regime (53). This chapter summarizes the most important theoretical approaches and techniques required in this thesis.

2.1 Maxwell's Equations

Maxwell's equations explain the behavior of electromagnetic fields in physical media. These equations illustrate the induction of electric and magnetic fields by each other and by sources i.e. currents and charges. Here, we show macroscopic behavior of the electromagnetic field.

In Maxwell's equations the field quantities are electric field strength $\underline{\mathbf{E}}(\underline{\mathbf{R}},t)$, magnetic field strength $\underline{\mathbf{H}}(\underline{\mathbf{R}},t)$, electric flux density $\underline{\mathbf{D}}(\underline{\mathbf{R}},t)$, and magnetic flux density $\underline{\mathbf{B}}(\underline{\mathbf{R}},t)$ which are measured in V/m, A/m, As/m^2, and Vs/m^2, respectively. These quantities are vector fields. The source quantities are vectorial electric (volume) current density $\underline{\mathbf{J}}_{\mathrm{e}}(\underline{\mathbf{R}},t)$ and scalar electric (volume) charge density $\varrho_{\mathrm{e}}(\underline{\mathbf{R}},t)$ measured in A/m^2 and As/m^3, respectively. The source and field quantities are function of three spatial $\underline{\mathbf{R}}$ and one time t coordinates.

The four famous equations of Maxwell can be written in integral and differential form.

2.1.1 Differential Form

Differential form of Maxwell's equations provides the interaction of quantities at a fixed point in space and time. It is illustrated by the two vectorial differential operators, curl $\boldsymbol{\nabla}\times$ and divergence $\boldsymbol{\nabla}\cdot$, which explain the strength of the circulation and divergence of a vector field, respectively. Differential form of Maxwells equations is written as (54),

$$\boldsymbol{\nabla}\times\underline{\mathbf{E}}(\underline{\mathbf{R}},t) = -\frac{\partial}{\partial t}\underline{\mathbf{B}}(\underline{\mathbf{R}},t) \quad \text{(Faraday's induction law)}\ , \tag{2.1}$$

$$\boldsymbol{\nabla}\times\underline{\mathbf{H}}(\underline{\mathbf{R}},t) = \frac{\partial}{\partial t}\underline{\mathbf{D}}(\underline{\mathbf{R}},t) + \underline{\mathbf{J}}_{\mathrm{e}}(\underline{\mathbf{R}},t) \quad \text{(Ampère-Maxwell's circuital law)}\ , \tag{2.2}$$

$$\boldsymbol{\nabla}\cdot\underline{\mathbf{D}}(\underline{\mathbf{R}},t) = \underline{\varrho}_{\mathrm{e}}(\underline{\mathbf{R}},t) \quad \text{(Gauss' law of electric charges)}\ , \tag{2.3}$$

$$\boldsymbol{\nabla}\cdot\underline{\mathbf{B}}(\underline{\mathbf{R}},t) = 0 \quad \text{(Gauss' law of magnetic charges)}\ . \tag{2.4}$$

The law of conservation of charges must be contained for all sources of electromagnetic fields. This is described by the continuity equation, which is derived from the Ampere-Maxwells law and from the Gausss law of electric charges. It reads,

$$\boldsymbol{\nabla}\cdot\underline{\mathbf{J}}_{\mathrm{e}}(\underline{\mathbf{R}},t) = -\frac{\partial}{\partial t}\underline{\varrho}_{\mathrm{e}}(\underline{\mathbf{R}},t)\,. \tag{2.5}$$

2.1.2 Integral Form

The integral form of Maxwell's equations describes the relationship of fields and their sources over a volume (V) or through any surface (S). Integral form can be obtained by using the Stoke's theorem on the first two Maxwell's equations. And the Gauss's theorem is used for the third and fourth Maxwell's equations. The integral form of Maxwell's equations for non-moving media (54),

$$\oint\limits_{C=\partial S} \underline{\mathbf{E}}(\underline{\mathbf{R}},t)\cdot\underline{\mathbf{dR}} = -\iint\limits_{S}\frac{\partial}{\partial t}\underline{\mathbf{B}}(\underline{\mathbf{R}},t)\cdot\underline{\mathbf{dS}}\,, \tag{2.6}$$

$$\oint\limits_{C=\partial S} \underline{\mathbf{H}}(\underline{\mathbf{R}},t)\cdot\underline{\mathbf{dR}} = \iint\limits_{S}\frac{\partial}{\partial t}\underline{\mathbf{D}}(\underline{\mathbf{R}},t)\cdot\underline{\mathbf{dS}} + \iint\limits_{S}\underline{\mathbf{J}}_{\mathrm{e}}(\underline{\mathbf{R}},t)\cdot\underline{\mathbf{dS}}\,, \tag{2.7}$$

$$\oiint\limits_{S=\partial V} \underline{\mathbf{D}}(\underline{\mathbf{R}},t)\cdot\underline{\mathbf{dS}} = \iiint\limits_{V}\varrho_{\mathrm{e}}(\underline{\mathbf{R}},t)\,\mathrm{d}V\,, \tag{2.8}$$

$$\oiint\limits_{S=\partial V} \underline{\mathbf{B}}(\underline{\mathbf{R}},t)\cdot\underline{\mathbf{dS}} = 0\,, \tag{2.9}$$

where, $C=\partial S$ is a closed integration contour over the surface S, $S=\partial V$ is a closed surface which encloses the volume V, $\mathrm{d}V$ is a scalar volume element, $\underline{\mathbf{dR}}$ is a vectorial line element and $\underline{\mathbf{dS}}$ is a vectorial surface element.

Continuity equation in integral form is written as,

$$\oiint\limits_{S=\partial V} \underline{\mathbf{J}}_{\mathrm{e}}(\underline{\mathbf{R}},t)\cdot\underline{\mathbf{dS}} = -\frac{\mathrm{d}}{\mathrm{d}t}Q_{\mathrm{e}}(t)\,. \tag{2.10}$$

2.1.3 Time Harmonic Form

Time harmonic form of Maxwell's equation describes the behavior of oscillating electromagnetic field at a particular frequency. It can be obtained by taking the fourier transform of the Maxwell's equations. Time harmonic differential form of Maxwell's equations given as (54),

$$\boldsymbol{\nabla}\times\underline{\mathbf{E}}(\underline{\mathbf{R}}) = j\omega\underline{\mathbf{B}}(\underline{\mathbf{R}})\,, \tag{2.11}$$

$$\boldsymbol{\nabla}\times\underline{\mathbf{H}}(\underline{\mathbf{R}}) = -\,j\omega\underline{\mathbf{D}}(\underline{\mathbf{R}}) + \underline{\mathbf{J}}_{\mathrm{e}}(\underline{\mathbf{R}})\,, \tag{2.12}$$

$$\boldsymbol{\nabla}\cdot\underline{\mathbf{D}}(\underline{\mathbf{R}}) = \varrho_{\mathrm{e}}(\underline{\mathbf{R}})\,, \tag{2.13}$$

$$\boldsymbol{\nabla}\cdot\underline{\mathbf{B}}(\underline{\mathbf{R}}) = 0\,. \tag{2.14}$$

And the time harmonic integral form is (54),

$$\oint\limits_{C=\partial S} \underline{\mathbf{E}}(\underline{\mathbf{R}}) \cdot \underline{\mathbf{dR}} = j\omega \iint\limits_{S} \underline{\mathbf{B}}(\underline{\mathbf{R}}) \cdot \underline{\mathbf{dS}}\,, \tag{2.15}$$

$$\oint\limits_{C=\partial S} \underline{\mathbf{H}}(\underline{\mathbf{R}}) \cdot \underline{\mathbf{dR}} = -\,j\omega \iint\limits_{S} \underline{\mathbf{D}}(\underline{\mathbf{R}}) \cdot \underline{\mathbf{dS}} + \iint\limits_{S} \underline{\mathbf{J}}_{\mathrm{e}}(\underline{\mathbf{R}}) \cdot \underline{\mathbf{dS}}\,, \tag{2.16}$$

$$\oiint\limits_{S=\partial V} \underline{\mathbf{D}}(\underline{\mathbf{R}}) \cdot \underline{\mathbf{dS}} = \iiint\limits_{V} \varrho_{\mathrm{e}}(\underline{\mathbf{R}})\,\mathrm{d}V\,, \tag{2.17}$$

$$\oiint\limits_{S=\partial V} \underline{\mathbf{B}}(\underline{\mathbf{R}}) \cdot \underline{\mathbf{dS}} = 0\,. \tag{2.18}$$

2.2 Constitutive Relations

Maxwell's equations together with constitutive relations represent the behavior of electromagnetic fields in a physical media. The constitutive relations for linear, isotropic and lossless media,

$$\underline{\mathbf{D}} = \varepsilon_0 \varepsilon_{\mathrm{r}} \underline{\mathbf{E}}\,, \tag{2.19}$$

$$\underline{\mathbf{B}} = \mu_0 \mu_{\mathrm{r}} \underline{\mathbf{H}}\,, \tag{2.20}$$

$$\underline{\mathbf{J}}_e = \sigma_{\mathrm{e}} \underline{\mathbf{E}}\,, \tag{2.21}$$

where ε_0 is the permittivity of free space and is approximately equal to the $8.85\times\ 10^{-12}$ F/m, μ_0 is the permeability of free space which is equal to the $1.257\times\ 10^{-6}$ H/m and σ_{e} is the electric conductivity measured in S/m. ε_{r} and μ_{r} are the relative permittivity and relative permeability of a material, respectively.

The permittivity ε and permeability μ are associated with the electric χ and magnetic χ_{m} susceptibilities of the material as given below (55),

$$\varepsilon = \varepsilon_0 \varepsilon_{\mathrm{r}} = \quad \varepsilon_0 (1 + \chi)\,, \tag{2.22}$$

$$\mu = \mu_0 \mu_{\mathrm{r}} = \mu_0 (1 + \chi_{\mathrm{m}})\,, \tag{2.23}$$

the electric and magnetic polarization properties of the medium are measured by the electric χ and magnetic χ_{m}susceptibilities, respectively. The electric flux density takes the following form (55),

$$\underline{\mathbf{D}} = \varepsilon_0 \varepsilon_{\mathrm{r}} \underline{\mathbf{E}} = \varepsilon_0 (1+\chi) \underline{\mathbf{E}} = \varepsilon_0 \underline{\mathbf{E}} + \varepsilon_0 \chi \underline{\mathbf{E}} = \varepsilon_0 \underline{\mathbf{E}} + \underline{\mathbf{P}}\,, \tag{2.24}$$

where $\underline{\mathbf{P}} = \varepsilon_0 \chi \underline{\mathbf{E}}$ is the dielectric polarization of the medium (i.e. the average electric dipole per unit volume). The magnetic flux density is (55)

$$\underline{\mathbf{B}} = \mu_0 \mu_{\mathrm{r}} \underline{\mathbf{H}} = \mu_0 (1+\chi_{\mathrm{m}}) \underline{\mathbf{H}} = \mu_0 (\underline{\mathbf{H}} + \chi_{\mathrm{m}} \underline{\mathbf{H}}) = \mu_0 (\underline{\mathbf{H}} + \underline{\mathbf{M}})\,, \tag{2.25}$$

where $\underline{\mathbf{M}} = \chi_{\mathrm{m}} \underline{\mathbf{H}}$ is the magnetization of the medium (i.e. average magnetic moment per unit volume). The speed of light c in a medium, the characteristic impedance η and the refractive index n of the medium can be defined in terms of permittivity and permeability as

$$c = \sqrt{\frac{1}{\varepsilon \mu}}, \eta = \sqrt{\frac{\mu}{\varepsilon}}, n = \sqrt{\varepsilon_{\mathrm{r}} \mu_{\mathrm{r}}}\,. \tag{2.26}$$

The constitutive relations for inhomogeneous medium where the permittivity depends on the position within the medium (55)

$$\underline{\mathbf{D}}(\underline{\mathbf{R}}, t) = \varepsilon(\underline{\mathbf{R}}) \underline{\mathbf{E}}(\underline{\mathbf{R}}, t)\,. \tag{2.27}$$

In an anisotropic medium, the material property ε depends on the x,y,z direction and the constitutive relation is defined by the tensor form (55)

$$\begin{bmatrix} \mathrm{D}_x \\ \mathrm{D}_y \\ \mathrm{D}_z \end{bmatrix} = \begin{bmatrix} \varepsilon_{xx} & \varepsilon_{xy} & \varepsilon_{xz} \\ \varepsilon_{yx} & \varepsilon_{yy} & \varepsilon_{yz} \\ \varepsilon_{zx} & \varepsilon_{zy} & \varepsilon_{zz} \end{bmatrix} \begin{bmatrix} \mathrm{E}_x \\ \mathrm{E}_y \\ \mathrm{E}_z \end{bmatrix}. \tag{2.28}$$

For nonlinear media, the permittivity depends on the magnitude of the applied electric field (55),

$$\underline{\mathbf{D}} = \varepsilon(E)\underline{\mathbf{E}}\,. \tag{2.29}$$

The constitutive relation for the frequency dependent (dispersive media) is defined as (55),

$$\underline{\mathbf{D}}(\underline{\mathbf{R}},\omega) = \varepsilon(\underline{\mathbf{R}},\omega)\underline{\mathbf{E}}(\underline{\mathbf{R}},\omega)\,. \tag{2.30}$$

2.3 Interface Conditions

Maxwell's equations are valid in the region where the constitutive parameters (ε,μ, or σ) of the medium are uniform. But, at the interface of two different physical media, the material parameters change abruptly which can make changes in the electromagnetic fields. Therefore, we need boundary conditions to enforce at the interface between the media to get a unique solution of Maxwell's equations for all physical regions. They can be obtained easily from the integral form of Maxwell's equations (55). The general transition conditions at the interface of two media are (55),

$$\underline{\hat{\mathbf{n}}} \times (\underline{\mathbf{E}}_2 - \underline{\mathbf{E}}_1) = \underline{\mathbf{0}}\,, \tag{2.31}$$

$$\underline{\hat{\mathbf{n}}} \times (\underline{\mathbf{H}}_2 - \underline{\mathbf{H}}_1) = \underline{\mathbf{J}}_s\,, \tag{2.32}$$

$$\underline{\hat{\mathbf{n}}} \cdot (\underline{\mathbf{B}}_2 - \underline{\mathbf{B}}_1) = 0\,, \tag{2.33}$$

$$\underline{\hat{\mathbf{n}}} \cdot (\underline{\mathbf{D}}_2 - \underline{\mathbf{D}}_1) = \rho_s\,, \tag{2.34}$$

where, $\underline{\hat{\mathbf{n}}}$ is the unit normal vector, and subscripts 1 and 2 relates to medium 1 and medium 2, respectively. Eq. (2.31) and Eq. (2.32) describe the tangential component of the electric field $\underline{\mathbf{E}}$ is continuous, while the magnetic field $\underline{\mathbf{H}}$ is equal to the surface current density $\underline{\mathbf{J}}_s$, across the boundary surface of two media. Eq. (2.33) and Eq. (2.34) state that the normal component of the magnetic flux density $\underline{\mathbf{B}}$ is continuous, whereas the electric flux density $\underline{\mathbf{D}}$ is equal to the surface charge density ρ_s, across the interface between the two media.

In many interface problems, there are no externally applied surface charges or surface currents on the boundary. In such a case, the transition conditions are

$$\underline{\hat{\mathbf{n}}} \times (\underline{\mathbf{E}}_2) = \underline{\hat{\mathbf{n}}} \times (\underline{\mathbf{E}}_1)\,, \tag{2.35}$$

$$\underline{\hat{\mathbf{n}}} \times (\underline{\mathbf{H}}_2) = \underline{\hat{\mathbf{n}}} \times (\underline{\mathbf{H}}_1)\,, \tag{2.36}$$

$$\underline{\hat{\mathbf{n}}} \cdot (\underline{\mathbf{B}}_2) = \underline{\hat{\mathbf{n}}} \cdot (\underline{\mathbf{B}}_1)\,, \tag{2.37}$$

$$\underline{\hat{\mathbf{n}}} \cdot (\underline{\mathbf{D}}_2) = \underline{\hat{\mathbf{n}}} \cdot (\underline{\mathbf{D}}_1)\,. \tag{2.38}$$

2.4 Wave Equations

The wave equation describes the propagation of waves at a speed of light in space. The homogeneous wave equation can be derived from the Maxwell's equations by putting $\underline{\mathbf{J}}_{\mathrm{e}} = \varrho_{\mathrm{e}} = 0$ in Eqs. (2.2) and (2.3). The source-free Maxwell's equations can be written as,

$$\boldsymbol{\nabla}\times\underline{\mathbf{E}} = -\frac{\partial}{\partial t}\underline{\mathbf{B}}\,, \tag{2.39}$$

$$\boldsymbol{\nabla}\times\underline{\mathbf{H}} = \frac{\partial}{\partial t}\underline{\mathbf{D}}\,, \tag{2.40}$$

$$\boldsymbol{\nabla}\cdot\underline{\mathbf{D}} = 0\,, \tag{2.41}$$

$$\boldsymbol{\nabla}\cdot\underline{\mathbf{B}} = 0\,. \tag{2.42}$$

If we apply the curl operator to Eq. (2.39) and by using $\underline{\mathbf{B}} = \mu_0\underline{\mathbf{H}}$, we get

$$\boldsymbol{\nabla}\times\boldsymbol{\nabla}\times\underline{\mathbf{E}} = -\mu_0\frac{\partial}{\partial t}\boldsymbol{\nabla}\times\underline{\mathbf{H}}\,. \tag{2.43}$$

By putting $\boldsymbol{\nabla}\times\underline{\mathbf{H}}$ from Eq. (2.40) and $\underline{\mathbf{D}} = \varepsilon_0\underline{\mathbf{E}}$,

$$\boldsymbol{\nabla}\times\boldsymbol{\nabla}\times\underline{\mathbf{E}} = -\varepsilon_0\mu_0\frac{\partial^2}{\partial t^2}\underline{\mathbf{E}}\,. \tag{2.44}$$

Since the vector identity is given as,

$$\boldsymbol{\nabla}\times\boldsymbol{\nabla}\times\underline{\mathbf{E}} = \boldsymbol{\nabla}(\boldsymbol{\nabla}\cdot\underline{\mathbf{E}}) - \boldsymbol{\nabla}^2\underline{\mathbf{E}}\,, \tag{2.45}$$

By using Eq. (2.41) and Eq. (2.44). The Eq. (2.45) becomes,

$$\boldsymbol{\nabla}^2\underline{\mathbf{E}} = \varepsilon_0\mu_0\frac{\partial^2}{\partial t^2}\underline{\mathbf{E}}\,, \tag{2.46}$$

where $c = \sqrt{\frac{1}{\varepsilon_0\mu_0}}$. The homogeneous wave equation for the electric field $\underline{\mathbf{E}}$ is given as

$$\boldsymbol{\nabla}^2\underline{\mathbf{E}}(\underline{\mathbf{R}},t) - \frac{1}{c^2}\frac{\partial^2}{\partial t^2}\underline{\mathbf{E}}(\underline{\mathbf{R}},t) = 0\,. \tag{2.47}$$

Similarly the wave equation for the magnetic field $\underline{\mathbf{H}}$,

$$\boldsymbol{\nabla}^2\underline{\mathbf{H}} - \frac{1}{c^2}\frac{\partial^2}{\partial t^2}\underline{\mathbf{H}} = 0\,. \tag{2.48}$$

In time harmonic form,

$$\boldsymbol{\nabla}^2\underline{\mathbf{E}} + k^2\underline{\mathbf{E}} = 0\,, \tag{2.49}$$

$$\boldsymbol{\nabla}^2\underline{\mathbf{H}} + k^2\underline{\mathbf{H}} = 0\,, \tag{2.50}$$

where, $k = \frac{w}{c}$ is the wavenumber. Eq. (2.49) and Eq. (2.50) are also known as homogeneous Helmholtz equations for electric and magnetic fields, respectively, which can be used for many scattering and resonance problems.

2.5 Surface Plasmons

The study of plasmonics is related to the behavior of electromagnetic waves when it interacts with free conduction electrons in the metal. The free electrons in the metal oscillate 180° out of phase with the incoming electric field, as predicted by the Drude model (53). Due to which, most metals have a negative permittivity at visible regime. The surface and volume charge oscillations of free conduction of metal excited by optical frequency are known as surface plasmons or plasmons polaritons (53). Surface plasmons are excited at the interface of metal and dielectric. As a consequence, the electromagnetic field is highly enhanced and confined at the interface of metal-dielectric. They can be excited at the interface of metal-dielectric layer and also at the surface of metal-dielectric nanoparticles. Surface plasmons

which are excited at the interface of metal-dielectric layer are known as SPPs; and which are excited at the interface of metal-dielectric nanoparticles are known as LSPs.

2.5.1 Surface Plasmon Polaritons

Surface plasmon polaritons (SPPs) are electromagnetic excitations propagating at the interface between a dielectric and a conductor, evanescently confined in the perpendicular direction. These electromagnetic surface waves arise via the coupling of the electromagnetic fields to oscillations of the conductors electron plasma.

In this section, we study the physical properties of SPPs by applying the Maxwell's equation to the planar interface between metal and dielectric. We start by considering one dimensional planar waveguide geometry(Figure 2.1), where the permittivity ε depends on only one spatial direction i.e. z-direction. The monochromatic plane wave ($\underline{\mathbf{E}}_0\ exp(jwt - j\underline{\mathbf{k}}.\underline{\mathbf{r}})$) explicitly propagates along the x-direction and there is no spatial variation along the y-direction of the waveguide. To find the specific field equations for determining the field profile of the electromagnetic waves, we use Maxwell's curl equations in time harmonic dependence (i.e. $\frac{\partial}{\partial t} = -j\omega$)

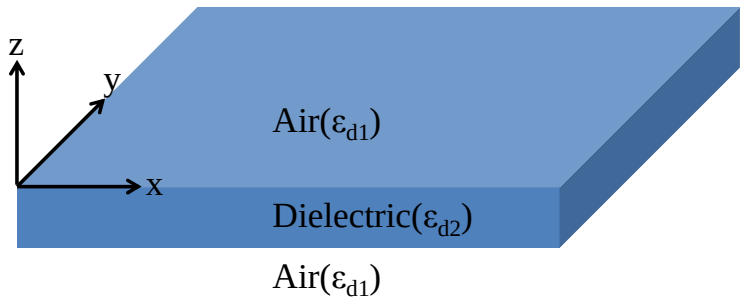

Figure 2.1: Schematic geometry of a planar waveguide. The propagation direction of the wave is along x-direction, no variation along the y-direction (53).

$$\frac{\partial}{\partial z}E_z - \frac{\partial}{\partial z}E_y = j\omega\mu_0 H_x\,, \tag{2.51}$$
$$\frac{\partial}{\partial z}E_x - \frac{\partial}{\partial x}E_z = j\omega\mu_0 H_y\,, \tag{2.52}$$
$$\frac{\partial}{\partial x}E_y - \frac{\partial}{\partial y}E_x = j\omega\mu_0 H_z\,, \tag{2.53}$$
$$\frac{\partial}{\partial y}H_z - \frac{\partial}{\partial z}H_y = -\,j\omega\varepsilon_0\varepsilon E_x\,, \tag{2.54}$$
$$\frac{\partial}{\partial z}H_x - \frac{\partial}{\partial x}H_z = -\,j\omega\varepsilon_0\varepsilon E_y\,, \tag{2.55}$$
$$\frac{\partial}{\partial x}H_y - \frac{\partial}{\partial y}H_x = -\,j\omega\varepsilon_0\varepsilon E_z\,. \tag{2.56}$$

Since the wave propagates along the x-direction (i.e. $\frac{\partial}{\partial x} = j\beta$) and the uniformity in the y-direction (i.e. $\frac{\partial}{\partial y} = 0$), the system of equation becomes

$$\frac{\partial}{\partial z}E_y = -\,j\omega\mu_0 H_x\,, \tag{2.57}$$
$$\frac{\partial}{\partial z}E_x - j\beta E_z = j\omega\mu_0 H_y\,, \tag{2.58}$$
$$j\beta E_y = j\omega\mu_0 H_z\,, \tag{2.59}$$
$$\frac{\partial}{\partial z}H_y = j\omega\varepsilon_0\varepsilon E_x\,, \tag{2.60}$$
$$\frac{\partial}{\partial z}H_x - j\beta H_z = -\,j\omega\varepsilon_0\varepsilon E_y\,, \tag{2.61}$$
$$j\beta H_y = -\,j\omega\varepsilon_0\varepsilon E_z\,, \tag{2.62}$$

This set of equations provides two solutions of the propagating wave with transverse electric (TE) polarization and with transverse magnetic polarization (TM) (53). For TM modes only E_x, E_z and H_y field components are nonzero, while for TE modes only H_x, H_z and E_y components are nonzero. The governing equations for TM modes are

$$E_x = -\, j\frac{1}{\omega\varepsilon_0\varepsilon}\frac{\partial}{\partial z}H_y\,, \tag{2.63}$$

$$E_z = -\,\frac{\beta}{\omega\varepsilon_0\varepsilon}H_y\,, \tag{2.64}$$

and the wave equation for the TM modes becomes

$$\frac{\partial^2}{\partial z^2}H_y + (k_0^2\varepsilon - \beta^2)H_y = 0\,. \tag{2.65}$$

For TE modes the governing equation are given as

$$H_x = j\frac{1}{\omega\mu_0}\frac{\partial}{\partial z}E_y\,, \tag{2.66}$$

$$H_z = \frac{\beta}{\omega\mu_0}E_y\,, \tag{2.67}$$

and the TE wave equation is

$$\frac{\partial^2}{\partial z^2}E_y + (k_0^2\varepsilon - \beta^2)E_y = 0\,. \tag{2.68}$$

With these equations in hand, we can now move to the description of surface plasmon polaritons.

2.5.1.1 Surface Plasmon Polaritons at a Single Interface

We consider a simple geometry for the excitation of SPPs which consists of single planar interface at $z = 0$ between a half space metal ($@z < 0$) and a half space dielectric ($@z > 0$), as shown in Figure 2.2. The material property of the metal is defined by the complex permittivity value $\varepsilon_m(\omega)$ with $Re[\varepsilon_m]$ is negative. The material property of the dielectric is defined by the homogeneous dielectric function ε_d.

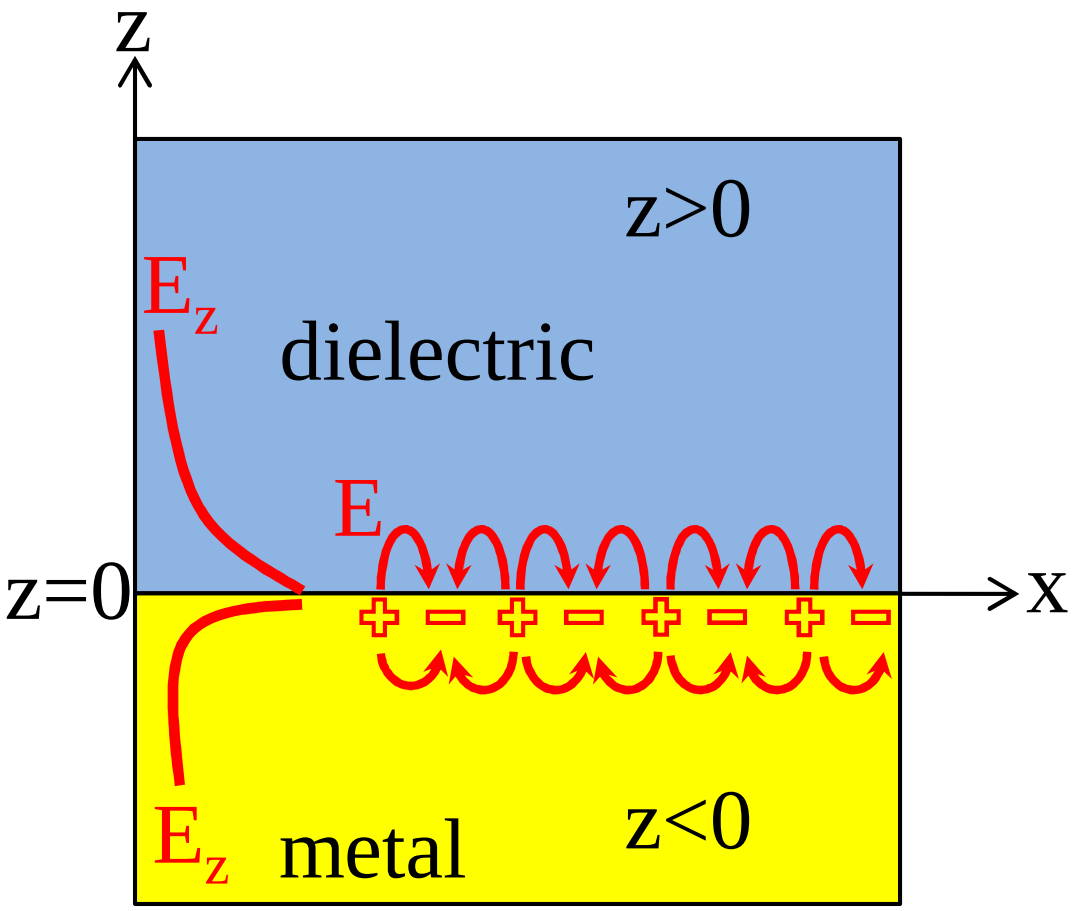

Figure 2.2: The electric field distribution and the excitation of surface plasmon polaritons at the planar interface of metal and dielectric media.

Let's use TE solutions in both half spaces from Eqs. (2.66)-(2.68), we get for $z > 0$,

$$E_y(z) = A_2 e^{j\beta_x x} e^{-k_{z,d} z}\,, \tag{2.69}$$

$$H_x(z) = jA_2 \frac{1}{\omega\mu_0} k_{z,d} e^{j\beta_x x} e^{-k_{z,d} z}\,, \tag{2.70}$$

$$H_z(z) = -A_2 \frac{\beta_x}{\omega\mu_0} e^{j\beta_x x} e^{-k_{z,d} z}\,, \tag{2.71}$$

and for $z < 0$

$$E_y(z) = A_1 e^{j\beta_x x} e^{k_{z,m} z}\,, \tag{2.72}$$

$$H_x(z) = -\,jA_1 \frac{1}{\omega\mu_0} k_{z,m} e^{j\beta_x x} e^{k_{z,m} z}\,, \tag{2.73}$$

$$H_z(z) = -\,A_1 \frac{\beta_x}{\omega\mu_0} e^{j\beta_x x} e^{k_{z,m} z}\,. \tag{2.74}$$

Continuity of the field components E_y and H_x at the interface (i.e.,@$z = 0$) requires the conditions $A_1 = A_2$ and together with,

$$A_1(k_{z,m} + k_{z,d}) = 0\,. \tag{2.75}$$

For the confinement of the surface waves, $Re[k_{z,m}]$ and $Re[k_{z,d}]$ must be greater than 0, and it can only be satisfied if $A_1 = 0$, which makes $A_2 = 0$ (as $A_1 = A_2$). Hence the surface waves do not exist of TE polarization.

Now let's have a look into the TM solutions in both half spaces from Eqs. (2.63)-(2.65), we get for $z > 0$,

$$H_y(z) = A_2 e^{j\beta_x x} e^{-k_{z,d} z}\,, \tag{2.76}$$

$$E_x(z) = jA_2 \frac{1}{\omega\varepsilon_0\varepsilon_d} k_{z,d} e^{j\beta_x x} e^{-k_{z,d} z}\,, \tag{2.77}$$

$$E_z(z) = -\,A_2 \frac{\beta_x}{\omega\varepsilon_0\varepsilon_d} e^{j\beta_x x} e^{-k_{z,d} z}\,, \tag{2.78}$$

and for $z < 0$

$$H_y(z) = A_1 e^{j\beta_x x} e^{k_{z,m} z}\,, \tag{2.79}$$

$$E_x(z) = -\,jA_1 \frac{1}{\omega\varepsilon_0\varepsilon_m} k_{z,m} e^{j\beta_x x} e^{k_{z,m} z}\,, \tag{2.80}$$

$$E_z(z) = -\,A_1 \frac{\beta_x}{\omega\varepsilon_0\varepsilon_m} e^{j\beta_x x} e^{k_{z,m} z}\,, \tag{2.81}$$

where $k_{z,m}$ and $k_{z,d}$ are the components of the wave vectors perpendicular to the interface in the two media. By using $A_1 = A_2$ for the continuity of H_y and E_x at the interface, we get (53),

$$\frac{k_{z,d}}{k_{z,m}} = -\frac{\varepsilon_d}{\varepsilon_m}\,. \tag{2.82}$$

Furthermore the expression for H_y has to satisfy the wave equation, which yields,

$$\beta_x^2 = k_0^2\varepsilon_m - k_{z,m}^2\,, \tag{2.83}$$

$$\beta_x^2 = k_0^2\varepsilon_d - k_{z,d}^2 \quad = k_0^2\varepsilon_d - (-\frac{\varepsilon_d}{\varepsilon_m}k_{z,m})^2\,. \tag{2.84}$$

From Eqs. (2.83) and (2.84), we get,

$$\beta_x = k_0\sqrt{\frac{\varepsilon_m\varepsilon_d}{\varepsilon_m+\varepsilon_d}}\,, \tag{2.85}$$

$$k_{z,m} = k_0\sqrt{\frac{\varepsilon_m^2}{\varepsilon_m+\varepsilon_d}}\,, \tag{2.86}$$

$$k_{z,d} = k_0\sqrt{\frac{\varepsilon_d^2}{\varepsilon_m+\varepsilon_d}}\,. \tag{2.87}$$

where $k_0 = 2\pi/\lambda$ is the wavenumber with λ as the wavelength of free-space. Hence the surface waves only exists for TM solutions. Eq.(2.82) and Eq. (2.85) are also valid for the lossless media representing a guided mode, if the permittivities of both media are of opposite signs. This guided mode is also known as the Fano mode (53). In order to have the Fano mode, the real part of the metals permittivity needs to be negative, as the permittivity of the dielectric medium is normally positive (53). The free-electron model for the metals is (56),

$$\varepsilon_m = \varepsilon_0(1 - \frac{\omega_p^2}{\omega^2 + j\omega\nu}), \tag{2.88}$$

where ν is the collision frequency and ω_p is the plasma frequency given as (56),

$$\omega_p = \sqrt{\frac{Ne^2}{\varepsilon_0 m_e}}, \tag{2.89}$$

where N is the concentration of free electrons, and e and m_e are the charge and mass of electrons, respectively.

In metals, absorption always occurs which can be represented by the nonzero imaginary part of the permittivity of the metals and allow the presence of guided modes even for $\varepsilon_m^{'} > -\varepsilon_d$. These guided modes present a very high attenuation and are also known as evanescent modes. Here, the guided modes represented by Eq.(2.85) are referred as surface plasmon polaritons (SPPs). If the real part of the permittivity of a metal in Eq.(2.85) is less than zero (negative) and its magnitude is quite larger than its imaginary part such as $\varepsilon_m^{'} >> \varepsilon_m^{''}$, the complex propagation constant of the SPPs can be written as,

$$\beta_x^{SPP} = \beta_x^{SPP'} + j\beta_x^{SPP''} = k_0\sqrt{\frac{\varepsilon_m^{'}\varepsilon_d}{\varepsilon_m^{'} + \varepsilon_d}} + jk_0\frac{\varepsilon_m^{''}}{2(\varepsilon_m^{'})^2}(\frac{\varepsilon_m^{'}\varepsilon_d}{\varepsilon_m^{'} + \varepsilon_d})^{3/2}, \tag{2.90}$$

where $\beta_x^{SPP'}$ and $\beta_x^{SPP''}$ express the real and imaginary parts of the propagation constant β_x^{SPP} (56).

2.5.1.2 Propagation Length

The nonzero imaginary part of the propagation constant of SPPs is due to the fact that the metals have a nonzero imaginary part and it causes the attenuation of the SPPs. The attenuation can be specified by the propagation length L, which is defined as the propagation distance of the SPP at which it loses its energy by a factor of $1/e$,

$$L = \frac{1}{[2\beta_x^{SPP''}]} \,. \tag{2.91}$$

The presence of SPPs at the interface of metal and dielectric is restricted to the frequencies smaller than the critical frequency known as plasma frequency and is only appropriate to the metal. This critical frequency lies in the visible or UV region of the spectrum for metals (such as silver, gold and aluminum) (56). The attenuation of the SPPs decreases with the increasing wavelength for gold, silver and aluminum at a wavelength range $400-1000\ nm$ (56). The typical propagation lengths of SPPs along the interface of metal and dielectric (refractive index of 1.32) are $0.6-50\ \mu m$, $4-50\ \mu m$, and $6-14\ \mu m$ for gold, silver and aluminum, respectively (56).

2.5.1.3 Penetration Depth

The electromagnetic field of a SPPs approaches at its highest value at the interface of metal and dielectric, and decays exponentially perpendicular to the interface into both media. The decay of the field is characterized by the penetration depth Lp, which is defined as the distance of field from the interface to the position where the amplitude of the field decreases by a factor of $1/e$ into the media. For nonzero imaginary part of metals with $\varepsilon_m^{'} >> \varepsilon_m^{''}$ and $\varepsilon_m^{'} > -\varepsilon_d$ then $k_{z,m}$ and $k_{z,d}$ are purely imaginary in Eqs.(2.86) and (2.87), respectively (57). The penetration depth (L_p) can be computed as,

$$L_{p,m} = \frac{1}{Re[k_{z,m}]} \,, \tag{2.92}$$

$$L_{p,d} = \frac{1}{Re[k_{z,d}]} \,, \tag{2.93}$$

where $L_{p,m}$ and $L_{p,d}$ are the penetration depths in metal and dielectric, respectively. The penetration depths for a ($700\ nm$) wavelength from the gold ($\varepsilon_m^{'} = -16$)/water ($\varepsilon_{water} = 1.77$) interface are $26\ nm$ along gold film and $238\ nm$ along the water medium (58).

2.5.1.4 Excitation of Surface Plasmon Polaritons

Figure 2.3 shows the dispersion relation of SPPs together with the dispersion relation of light in air and dielectric mediums. As the wavevector of light line in air is smaller than the wavevector of SPP, the light line does not intersect with the SPP curve. Therefore, the SPPs in metals cannot be excited by a light directly incident from the air. Instead SPPs can be excited via some coupling method such as prism or grating coupling by increasing the wavevector of light and matching it with the SPP wavevector (59).

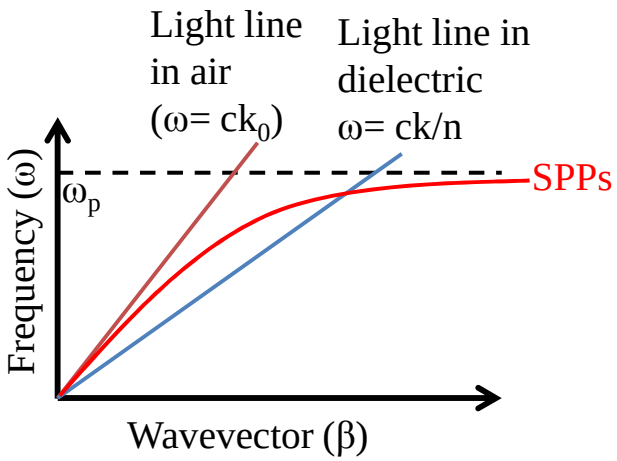

Figure 2.3: Dispersion relation of surface plasmon polaritons and the dispersion relation of light in air and dielectric mediums.

2.5.1.5 Attenuated Total Reflection (ATR) Coupler Method

The prism coupled attenuated total reflection (ATR) method is the most common approach for the excitation of the SPPs. There are two types of ATR configurations one is Kretschmann configuration and the other is Otto configuration. This thesis is based on the Kretschmann configuration method. In Kretschmann setup, a high refractive index prism (n_p) is coupled with a metal-dielectric waveguide consisting of a thin metal (ε_m) film and a semi-infinite dielectric (n_d) medium, as shown in Fig. 2.4. The component of the wavevector of light parallel to the prism-metal interface is given by,

$$k_x^p = k_0\sqrt{\varepsilon_p}sin(\theta_i) = k_0 n_p sin(\theta_i)\,, \tag{2.94}$$

here, θ_i represents the angle of incident light, ε_p and n_p are the permittivity and refractive index of the prism, respectively. In order to excite the SPPs, the component of the wavevector of light (k_x^p) parallel to the interface (prism-metal) needs to match the wavevector component (β_x^{SPP}) of the SPPs. The resonance condition in the Kretschmann configured ATR method can be given as (57),

$$k_x^p = \beta_x^{SPP}\,, \tag{2.95}$$

$$k_0\sqrt{\varepsilon_p}sin(\theta_i) = k_0\sqrt{\frac{\varepsilon_m\varepsilon_d}{\varepsilon_m+\varepsilon_d}}\,. \tag{2.96}$$

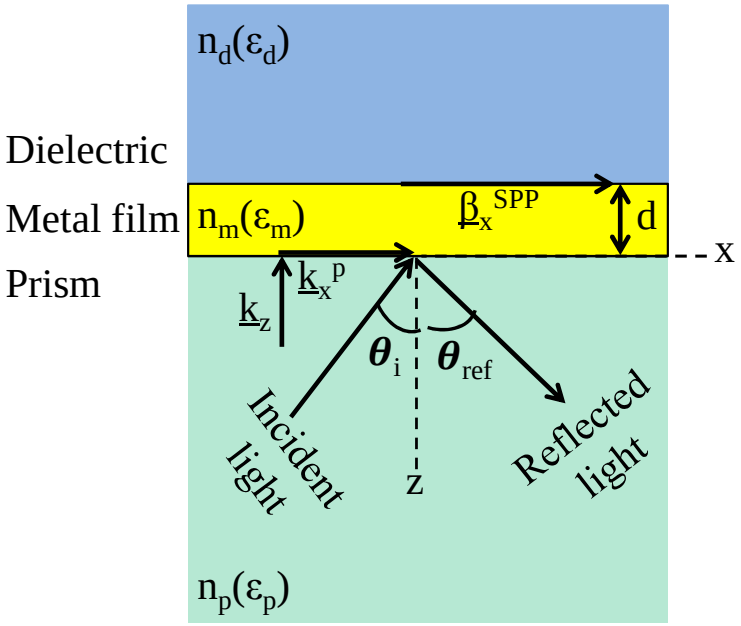

Figure 2.4: Schematic diagram of a light reflection in the Kretschmann configuration of the ATR method.

The total reflection of the light in the ATR configuration can be obtained by the Fresnel's equations for three-layer model ($prism/metal/dielectric$) (57),

$$R = (r^p_{p,m,d})^2 = (\frac{r^p_{p,m} + r^p_{m,d} e^{2ik_{z,m}d}}{1 + r^p_{p,m} r^p_{m,d} e^{2ik_{z,m}d}})^2 \,, \tag{2.97}$$

with,

$$r^p_{p,m} = \frac{cos(\theta_i)/n_p - (\varepsilon_m - n_p^2 sin^2(\theta_i))^{1/2}/\varepsilon_m}{cos(\theta_i)/n_p + (\varepsilon_m - n_p^2 sin^2(\theta_i))^{1/2}/\varepsilon_m} \,, \tag{2.98}$$

$$r^p_{m,d} = \frac{(\varepsilon_m - n_p^2 sin^2(\theta_i))^{1/2}/\varepsilon_m - (\varepsilon_d - n_p^2 sin^2(\theta_i))^{1/2}/\varepsilon_d}{(\varepsilon_m - n_p^2 sin^2(\theta_i))^{1/2}/\varepsilon_m + (\varepsilon_d - n_p^2 sin^2(\theta_i))^{1/2}/\varepsilon_d} \,, \tag{2.99}$$

where, d is the thickness of the metal film.

2.5.1.6 Magneto-Optic Effect

When a linearly polarized light is incident on a surface of a material which is under an applied magnetic field, the polarization plane of transmitted light is rotated by an angle. This angular rotation of the transmitted beam is determined by the real part of the refractive index (n) of the material (60). This magneto-optic effect has been discovered by Faraday in 1845 and is known as Faraday‘s effect (61). In 1877, a similar experiment has been performed by John Kerr, instead of transmission he observed the effect of a magnetic field on the reflection beam from a surface of the magnetized material (61). The rotation of reflected beam is proportional to the imaginary part of refractive index of the medium (i.e. absorption, k) (60). This phenomenon is called after his name as Kerr effect or magneto-optical Kerr effect (MOKE). There are three Kerr effects which are categorized depending on the magneto-optical geometry as longitudinal, transversal, and polar Kerr effect. In the longitudinal Kerr effect, the magnetization (M) is parallel to plane of sample and plane of incidence. In the transverse Kerr effect, the magnetization is also parallel to the plane of sample and is perpendicular to the plane of incidence. In the polar Kerr effect, the magnetization is perpendicular to the plane of sample and is parallel to the incident plane. In general, the longitudinal and polar Kerr effects modify the polarization of the incident

light from plane polarized to elliptically polarized (62). Whereas, for transverse Kerr effect there is no variation in the polarization of the incident light, it only varies amplitude of the reflected light (63). The variation in the amplitude of the reflected intensity of a p-polarized light for the transverse magneto-optical Kerr effect (TMOKE) can be computed from the delta signal (δ) (64),

$$\delta = \frac{R(H+) - R(H-)}{R(0)}\,, \tag{2.100}$$

where $R(H+)$ and $R(H-)$ are the reflected intensity of the light with opposite applied magnetic fields; whereas, $R(0)$ is the reflected intensity without magnetization for a p-polarized incident light.

The macroscopic approach of the magneto-optic effect is analyzed from the dielectric properties of a medium under an applied magnetic field. This effect can be described by antisymmetric, off-diagonal elements in a dielectric permittivity. The permittivity tensor of the medium magnetized along the y-direction in the transverse direction (Fig. 2.5) is given as (63),

$$\varepsilon = \tilde{\varepsilon} \begin{Bmatrix} 1 & 0 & -iQm_y \\ 0 & 1 & 0 \\ iQm_y & 0 & 1 \end{Bmatrix}, \tag{2.101}$$

where

$$\tilde{\varepsilon} = \tilde{n}^2 = (n + jk)^2\,, \tag{2.102}$$

$\tilde{\varepsilon}$ and $\tilde{n}$ are the complex relative permittivity and refractive index of the magnetized material, respectively. Q is the complex magneto-optic parameter known as Voigt constant (65) and m_y is the relative magnetization along y-direction.

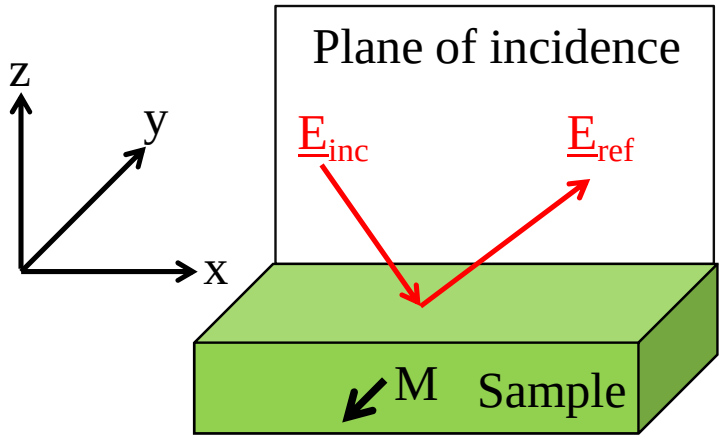

Figure 2.5: Configuration of a transverse magneto-optical Kerr effect (TMOKE). The magnetization (M) is parallel to the plane of sample and is perpendicular to the plane of incidence.

2.5.1.7 Sensitivity

Sensitivity (η) is an important characteristic of a sensor. It describes the computation of the response of an input signal per unit change of the measuring parameter. The sensitivity of an optical biosensor is the measurement of the response of a signal per unit change in the refractive index (n_d) (66). Several methods are used to compute the sensitivity of a plasmonic biosensor (66). In this thesis, the sensitivity is computed by intensity-interrogation method as a function of angle of incidence at a fixed wavelength, defined as (19)

$$\eta_{intensity} = \left(\frac{\partial S}{\partial \theta_i}\right) \times \left(\frac{\partial \theta_r}{\partial n_d}\right), \tag{2.103}$$

where,

$\eta_{intensity}$ is the intensity modulation sensitivity, S is the amplitude of the measuring signal, θ_i is the incident angle, θ_r is the resonance angle for SPPs, and n_d is the refractive index of the sensing medium. The sensitivity from Eq. (2.103) illustrate that it depends on the slope of the measured curve as a function of incident angle (θ_i) and the angular displacement of the resonance angle (θ_r) when refractive index (n_d) of the sensing medium changes.

2.5.2 Localized Surface Plasmons

Localized surface plasmon resonances (LSPRs) are the oscillation of free conduction electrons of metallic nanoparticles. The localized plasmon resonant modes are excited at the small, sub-wavelength metallic nanostructures in an oscillating electromagnetic field (53). The driven electrons by the external field get an effective restoring force due to the curved surface or the edges of the nanoparticles lead to the excitation of resonance (53). This resonance causes an amplification of the near-field inside and outside of the nanoparticles. The LSPRs are highly dependent on the shape, size and the dielectric property of the metallic nanoparticle and its adjacent medium. The later dependence of plasmon resonance on the surrounding medium makes it an active research area for sensing application.

2.5.2.1 Quasi-static Approximation and Mie theory

The quasi-static approximation describes the interaction of nanoparticle with the electromagnetic field if the dimension d of the particle is much smaller than the wavelength of the incident field (53). On this assumption, the phase of the incident oscillating electromagnetic field is constant over the volume of the particle (53). Due to which, the particle can be considered to be in an electrostatic field for calculating the spatial field distribution. After the computation of the field distributions, the time harmonic dependence of the field can then be added to the solution. The quasi-static approximation of the full scattering problem is useful for the description of the optical properties of the nanoparticles well below the dimension of 100 nm for many tasks (53).

The plasmonic oscillation of sphere is shown in Figure 2.6. The simple electrostatic can be used to compute the response of the light-metallic sphere interaction. The polarizability α of the metallic sphere with relative dielectric constant with respect to the medium (53), $\varepsilon_{\mathtt{r}} = \varepsilon_{\mathtt{metal}}/\varepsilon_{\mathtt{medium}}$ and volume V is given as,

$$\alpha = \varepsilon_0 3V \frac{\varepsilon_{\mathtt{r}} - 1}{\varepsilon_{\mathtt{r}} + 2}\,. \tag{2.104}$$

The electromagnetic field associated with plasmonic oscillations has two components, one is the near-field component which evolve into radiative far-field scattering and the other is the non-radiative absorbing component (67). The particle size and dielectric medium determine the contribution of these components (67). The excitation of the plasmonic oscillations in small metallic particles leads to the absorption of light, while scattering becomes dominant when the particle size is comparable to the wavelength of light. The ability of the metallic particle to transform incident light radiation into these components can be measured by the computation of the particle's absorption and scattering cross sections (67). The scattering and absorption cross-sections are then (53)

$$C_{\mathtt{sca}} = \frac{k^4}{16}(3V)^2 \frac{(\varepsilon'_{\mathtt{r}} - 1)^2 + \varepsilon''^2_{\mathtt{r}}}{(2 + \varepsilon'_{\mathtt{r}})^2 + \varepsilon''^2_{\mathtt{r}}}\,, \tag{2.105}$$

$$C_{\mathtt{abs}} = k3V \frac{3\varepsilon''_{\mathtt{r}}}{(2 + \varepsilon'_{\mathtt{r}})^2 + \varepsilon''^2_{\mathtt{r}}}\,. \tag{2.106}$$

The sum of the scattering and absorption cross sections represent the total extinction of light (67). The quasi-static approach is not valid, if the size of the nanoparticle is comparable to the wavelength of the incident field, due to the phase changes of the incident field over the particle volume (53). The electrodynamic approach is needed for the particles with larger dimensions. In this case, the Mie theory can be used by taking into consideration the impact of the particle size (37). Mie in his classical paper in 1908, developed a complete theory of absorption and scattering of electromagnetic radiation by a sphere, to understand the colors of the colloidal gold particles in solution (37). The Mie theory approach is to expand the internal and external scattered fields into a set of normal modes characterized by vectorial harmonics. The power series expansion of the absorption and scattering coefficients are used to recover the valid quasi-static results for subwavelength spheres and keeping only the first term. As reported by Mie, the spherical symmetry offers the use of a multipole extension of the fields, here represented by n. The plasmon resonance corresponds to the dipole mode $n = 1$. The scattering and extinction coefficients in the Mie theory are computed by (53),

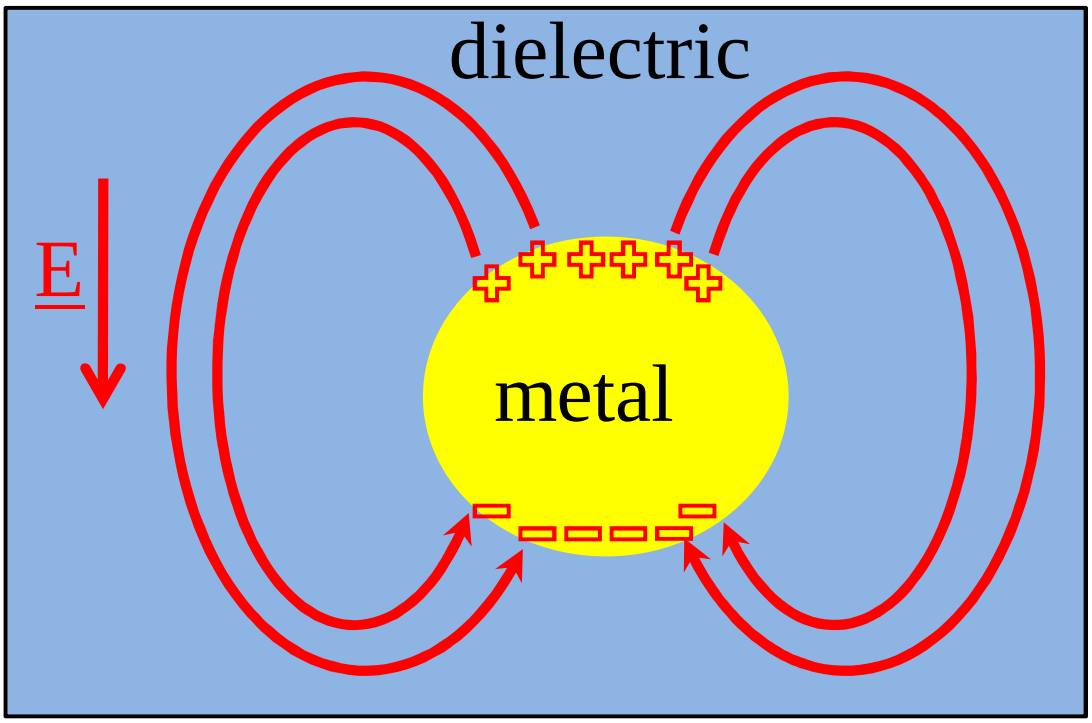

Figure 2.6: Localized surface plasmon resonance of a sphere in presence of external electric field.

$$Q^n_{sca} = \frac{2}{x^2}(2n+1)(|a_n|^2 + |b_n|^2)\,, \tag{2.107}$$

$$Q^n_{ext} = \frac{2}{x^2}(2n+1)Re(a_n + b_n)\,, \tag{2.108}$$

with $x = kr$, where k is the wave vector, r is the nanoparticle radius, and a_n and b_n are the Mie coefficients (68).

2.6 Simulation Method

Computational electromagnetics (CEM) is gaining much interest day by day in the field of engineering and research. Computational machines such as ordinary computers and parallel arrays of processors uses CEM to predict electromagnetic phenomena for different electromagnetic problems such as wave guiding, radiation and scattering phenomena, and design of

optical devices (69). Nowadays, the most commonly used CEM methods is categorized into the differential equation (DE) methods and the integral equation (IE) methods. Different techniques of CEM have been proposed to solve the integral or differential form of Maxwells equations such as Finite Difference (FD) method, Finite Difference Time Domain (FDTD) method, Finite Element Method (FEM), Finite Integration Technique (FIT) (69). In this thesis FIT is used for the simulation of optical plasmonic devices for sensing purpose. FIT was first introduced by Weiland in 1977 (70). FIT is similar to the FDTD method in terms of dicretization method. This technique is feasible in modeling complex geometrical shapes with high accuracy (70).

2.6.1 Finite Integration Technique (FIT)

The Finite Integration Technique (FIT) is a spatial discretization technique that is applied to physical electromagnetic problems under consideration in time domain. It is used to discretize the Maxwell's equations in integral form (see section 2.1.2). It can handle complex geometrical structures with accuracy. The FIT method uses orthogonal dual grid system (G and $\tilde{G}$) also known as staggered grid.

The First step of discretization in the FIT is to restrict the electromagnetic problem in a computational domain that contains the required geometry and region of interest for the computation. The computational domain can be spatially discretized into different grid complexes such as dual-coordinate-based cell complex consisting of cubic cells or dual cell grids consisting of Delaunay triangles and Voronoi polygons (70). Here, as an example, the cubic lattice is used to discretize computational domain for solving Integral form of Maxwell's equations (Eqs. (2.6) and (2.7)), as shown in Fig. 2.7. The computational domain is considered as a homogeneous medium. The cubic lattice is named as a material grid M which is divided into a small grid cells in a dual grid system i.e., a primary grid cells G, and a secondary dual grid $\tilde{G}$, as shown in Fig. 2.8. Both grid cells are orthogonal each to each other. The dimensions of the cell in Cartesian coordinates are $\triangle x$, $\triangle y$ and $\triangle z$. The whole computational domain is filled with the unit cells and a grid point (n_x,n_y,n_z) is defined as ($n_x = 1,...,N_x, n_y = 1,...,N_y, n_z = 1,...,N_z$).

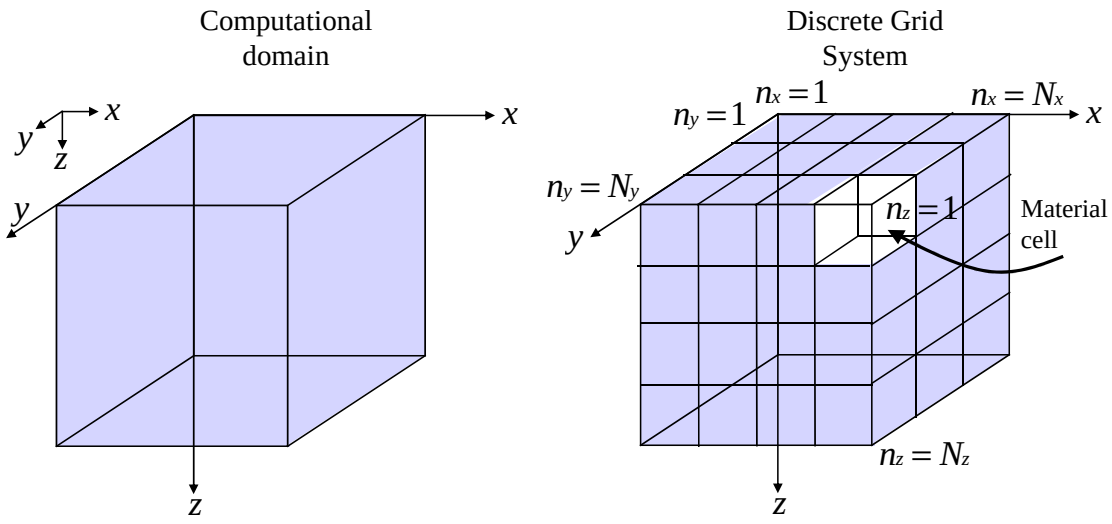

Figure 2.7: Computational domain and its discretization (71).

In the space domain, magnetic fields are sampled in center of the cubic surfaces while electric fields are sampled in the middle of the cubic edges (71). This makes every $\underline{\mathbf{E}}$ component is surrounded by four circulating $\underline{\mathbf{H}}$ components, and every $\underline{\mathbf{H}}$ component is surrounded by four circulating $\underline{\mathbf{E}}$ components.

In the time domain, a half time step difference is used to evaluate electric and magnetic field. For example the electric field is sampled at $t = n_t \triangle t$ while the magnetic field is sampled at $t = (n_t + 1/2) \triangle t$.

The multidimensional midpoint rule is used to approximate the integral appearing in the Maxwell's equations. The approximation of one-dimensional integral can be found by standard Taylor-series expansion,

$$\int_{x_0}^{x_0+\triangle x} \mathrm{f(x)}\, \mathrm{d}x = f(x_0 + \frac{\triangle x}{2}) \triangle x + O[(\triangle x)^3] \approx f(x_0 + \frac{\triangle x}{2}) \triangle x \,, \tag{2.109}$$

where, $O[(\triangle x)^3]$ is the approximation error. This approximation can also be used for the discretization of one-dimensional time integral. Similarly, approximations for two and three-dimensional space integral yield,

$$\int_{y_0}^{y_0+\triangle y}\int_{x_0}^{x_0+\triangle x} \mathrm{f(x,y)}\,\mathrm{d}x\mathrm{d}y \approx f(x_0+\frac{\triangle x}{2}, y_0+\frac{\triangle y}{2})\ \triangle x\triangle y\,, \tag{2.110}$$

$$\int_{z_0}^{z_0+\triangle z}\int_{y_0}^{y_0+\triangle y}\int_{x_0}^{x_0+\triangle x} \mathrm{f(x,y,z)}\,\mathrm{d}x\mathrm{d}y\mathrm{d}z \approx f(x_0+\frac{\triangle x}{2}, y_0+\frac{\triangle y}{2}, z_0+\frac{\triangle z}{2})\triangle x\triangle y\triangle z\,. \tag{2.111}$$

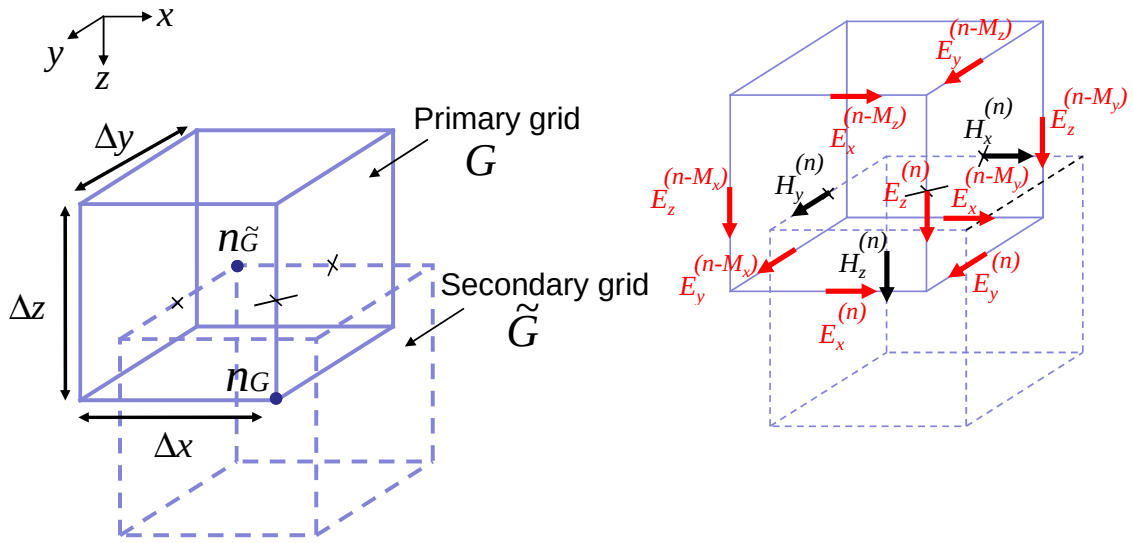

Figure 2.8: Dual orthogonal grid system in space (71).

For a three-dimensional simulation, the magnetic and electric field components are composed of H_x,H_y,H_z and E_x,E_y,E_z, respectively, as shown in Fig. 2.8. Then, updating equations for Eq. (2.6) and Eq. (2.7) are,

$$H_x^{(n,n_t+1/2)} = H_x^{(n,n_t-1/2)} - \frac{\triangle t}{\mu_0}\left[\frac{E_y^{(n-M_z,n_t)} - E_y^{(n,n_t)}}{\triangle z} + \frac{E_y^{(n,n_t)} - E_z^{(n-M_y,n_t)}}{\triangle y}\right], \tag{2.112}$$

$$H_y^{(n,n_t+1/2)} = H_y^{(n,n_t-1/2)} - \frac{\triangle t}{\mu_0}\left[\frac{E_x^{(n,n_t)} - E_x^{(n-M_z,n_t)}}{\triangle z} + \frac{E_z^{(n-M_x,n_t)} - E_z^{(n,n_t)}}{\triangle x}\right], \tag{2.113}$$

$$H_z^{(n,n_t+1/2)} = H_z^{(n,n_t-1/2)} - \frac{\triangle t}{\mu_0}\left[\frac{E_x^{(n-M_y,n_t)} - E_x^{(n,n_t)}}{\triangle y} + \frac{E_y^{(n,n_t)} - E_y^{(n-M_x,n_t)}}{\triangle x}\right], \tag{2.114}$$

$$E_x^{(n,n_t+1)} = E_x^{(n,n_t)} + \frac{\triangle t}{\varepsilon_0}\left[\frac{H_y^{(n,n_t+1/2)} - H_y^{(n+M_z,n_t+1/2)}}{\triangle z} + \frac{H_z^{(n+M_y,n_t)} - H_z^{(n,n_t)}}{\triangle y}\right], \tag{2.115}$$

$$E_y^{(n,n_t+1)} = E_y^{(n,n_t)} + \frac{\triangle t}{\varepsilon_0}\left[\frac{H_x^{(n+M_y,n_t+1/2)} - H_x^{(n,n_t+1/2)}}{\triangle z} + \frac{H_z^{(n,n_t+1/2)} - H_z^{(n+M_x,n_t+1/2)}}{\triangle x}\right], \tag{2.116}$$

$$E_z^{(n,n_t+1)} = E_z^{(n,n_t)} + \frac{\triangle t}{\varepsilon_0}\left[\frac{H_x^{(n,n_t+1/2)} - H_x^{(n+M_y,n_t+1/2)}}{\triangle y} + \frac{H_y^{(n+M_x,n_t+1/2)} - H_y^{(n,n_t+1/2)}}{\triangle x}\right]. \tag{2.117}$$

These updating equations can be easily modified to model different types of complex objects and materials such as dielectrics, metals and anisotropies (72).

The updating equations are used in the following manner to calculate the time evolution of electromagnetic fields. Electric and magnetic field values are set with zero values at initial time period. In the computation domain, a time domain excitation signal is then introduced. The excitation can be a lumped voltage source for an antenna problem, or a distributed plane wave source for scattering problems (72). Then, the electric field values are computed at $t = n_t \triangle t$ and magnetic field values are computed at $t = (n_t + 1/2)\triangle t$. These field values require to be updated on all grid points, which are the major consumptions of computational time and memory storage. The time iteration is required to run until the desired time response for the electromagnetic problem is found. As time increases, all radiated energy goes to infinity for an antenna or scattering problems therefore the field values are decayed to zero (72). The FIT computational domain is terminated for eigenvalue problems when a stable resonant signal is observed (72). Similarly, like FDTD, the above time-stepping procedure is fully explicit; hence no need to do matrix inversion. Which makes it easy to implement. The calculation variables electric voltages and magnetic fluxes

are located alternatively in time, as shown Fig. 2.9 in leap-frog scheme (52). The stability limit for the time step $\triangle t$ is given by Courant-Friedrichs-Levy(CFL) condition (70)

$$\triangle t \leq \frac{\sqrt{\mu\varepsilon}}{\sqrt{\left(\frac{1}{\triangle x}\right)^2+\left(\frac{1}{\triangle y}\right)^2+\left(\frac{1}{\triangle z}\right)^2}}, \tag{2.118}$$

which is needed to be satisfied in every single mesh cell.

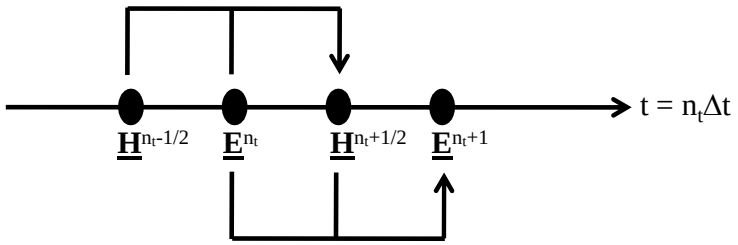

Figure 2.9: Leap-frog scheme (52)

2.6.1.1 Boundary Conditions

In order to solve numerical problems, it is necessary to limit the area of the computation to save memory and computation time. This can be done by applying boundary conditions at the artificial boundaries of the computational domain. These boundary conditions not only save memory and time of the computation, but also reduce the reflections coming from the artificial boundaries.

A plane wave can be decomposed into transverse electric (TE) polarized wave and the TM polarized wave. For TE-polarized wave, the Dirichlet boundary condition need to be imposed along the polarization direction of the electric field; which prescribes the tangential component of the field vector vanishes at the boundary of the computational domain,

$$\hat{\mathbf{n}} \times (\underline{\mathbf{E}}) = 0\,. \tag{2.119}$$

Similarly, for the TM-polarized wave, the Neumann boundary condition to be imposed along the polarization direction of the magnetic field; which described the vanishing of the normal component of the magnetic field at the boundary of the computational domain,

$$\hat{\mathbf{n}} \cdot (\underline{\mathbf{H}}) = 0 \,. \tag{2.120}$$

Absorbing boundary conditions are used to absorb the outgoing $\underline{\mathbf{E}}$ and $\underline{\mathbf{H}}$ fields that strike it without reflecting back into the problem space. There are two types of the absorbing boundary conditions (73). The one which is based on the traveling wave equations called radiation boundary condition. The other absorbing boundary condition is known as the perfectly matched layer (PMLs) (73). In PMLs an artificial layer is designed to absorb the electromagnetic waves without significant reflection. When a wave enters the absorbing layer, it is attenuated by the absorption and starts decaying through the layer, even when it reflects back from boundary, hence after one round trip, the returning wave is negligibly small. At the end of the PML, the computational domain can be truncated by Dirichlet boundary conditions. The PMLs are matched with the medium they terminate, hence, there would not be any reflection coming from the boundary between the terminating medium and the PML. When the considered electromagnetic problem include semi-infinite media than the PMLs are used to truncate the computational domain.

Photonic structures possess repeating nature with a constant periodicity between them, they can be represented by periodic boundary conditions. PBCs are used for the analysis of infinite structures that have periodicity in one or two dimensions. Due to the limited computation resources it is not possible to simulate infinite structure directly; therefore only a single unit cell of the structure is simulated by using PBCs at the boundary of the computational domain. They are used to approximate infinite array of any object (72).

Now consider a two dimensional infinite periodic structure with periodicity p in the x-direction. Hence, only E_y, H_x, H_z fields are non zero. Due to the periodicity in the geometry, only the fields in unit cells are needed to determine. Dashed lines in Fig. 2.10 denote the

unit cell edges. The field components that can be updated using the fields in the unit cell are denoted by solid blue symbols, while the fields that cannot be updated are denoted by solid white symbols. The field components that cannot be updated can be determined by using periodic boundary conditions that relate the fields on one side of the unit cell to the other side.

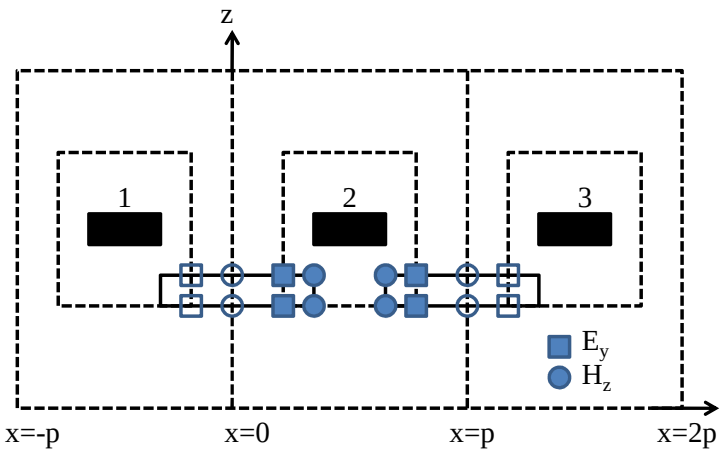

Figure 2.10: Infinite periodic structures with periodicity p in x-direction

The following equations in the frequency domain are satisfied by electromagnetic fields as

$$\underline{\mathbf{E}}(x=0,z) = \underline{\mathbf{E}}(x=p,z)e^{jk_x p}\,. \tag{2.121}$$

$$\underline{\mathbf{H}}(x=0,z) = \underline{\mathbf{H}}(x=p,z)e^{jk_x p}\,. \tag{2.122}$$

where, k_x is the wave vector component in x-direction and p is the periodicity used to determine propagation phase delay, which is represented by the exponential term.

The propagation constant k_x can be found by dispersion relation for a waveguide problem. But for scattering problem, it is known and can be determined by incident angle and frequency (72)

$$k_x = k_0 sin(\theta) = 2\pi f \sqrt{\varepsilon_0 \mu_0} sin(\theta)\,. \tag{2.123}$$

where k_0 is the wave number in free space. The above field equations can be converted to the time domain by using inverse Fourier transformation, which yields

$$\underline{\mathbf{E}}(x = 0,z,t) = \underline{\mathbf{E}}(x = p,z,t + psin\theta/c)\,. \tag{2.124}$$

$$\underline{\mathbf{H}}(x = 0,z,t) = \underline{\mathbf{H}}(x = p,z,t + psin\theta/c)\,. \tag{2.125}$$

where $c = \frac{1}{\sqrt{\varepsilon_0 \mu_0}}$ is the wave velocity in free space. Hence, field data in the future time $(t + psin\theta/c)$ are needed to update electric and magnetic fields in the current time t.

For a normal incident plane wave the value of k_x and θ becomes zero (72). Therefore the equations (2.124) and (2.125) can be simplified to

$$\underline{\mathbf{E}}(x = 0,z,t) = \underline{\mathbf{E}}(x = p,z,t)\,. \tag{2.126}$$

$$\underline{\mathbf{H}}(x = 0,z,t) = \underline{\mathbf{H}}(x = p,z,t)\,. \tag{2.127}$$

In this periodic boundary condition, no data for the future time is needed. Hence, this periodic boundary conditions can be implemented easily in finite integration technique.

2.6.1.2 Source and Detector

A plane wave source has been used in this thesis for simulation. It can be modeled by using the plane wave expression ($\underline{\mathbf{E}}_0\ exp(jwt - j\underline{\mathbf{k}}.\underline{\mathbf{r}})$). In order to excite a perfect plane wave source, then the source boundary must be taken carefully for the infinite extension of the source over the plane. This can be done by implementing PBCs along the boundary of the source plane. PBCs apply the infinite repetition condition along the plane of the source that will make the expression of the plane wave mathematically correct.

In CST MWS Studio solver, source is excited by using a waveguide port, which also absorbs and measures the reflected amplitudes. In order to excite a plane wave, the waveguide port at the boundary before PML boundary conditions along the z-direction and is extended in the x and y-directions of the computational domain, where PBCs are applied, as shown in Fig 2.11. After the excitation of the plane wave source from the waveguide port, it measures the transmission wave amplitude and travels along the propagation direction. If there is any reflecting object in the computational domain, then the wave reflects back to the waveguide port, where it absorbs all the reflected power and measures it. By this way, the waveguide port is used as for transmission of waves and also works as a detector.

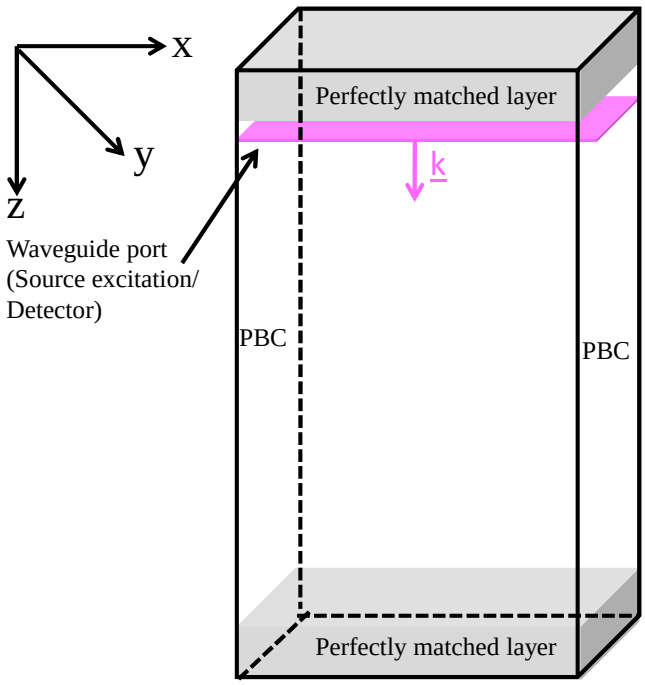

Figure 2.11: Simulation domain is bounded by perfectly matched layers (PML) boundary conditions on top and bottom and periodic boundary condition along x and y-directions. Waveguide port is used to excite plane wave source and it also works as a detector.

Chapter 3

Surface Plasmon Resonance (SPR) Sensor for Biosensing Applications

3.1 Introduction

Surface plasmon resonance (SPR) biosensors are widely used for label-free analysis of biomolecular interaction. SPR sensors are associated with the surface plasmon polaritons (SPPs) which are excited at the interface between the thin metal-dielectric layers and propagates along the interface (see section 2.5.1.1). With the excitation of propagating SPPs, the highly enhanced electromagnetic field is bounded by the metal-dielectric interface. The enhanced electromagnetic field decays exponentially in the perpendicular direction from the interface (see section 2.5.1.3). The energy bound to the interface leads to the sensitivity of SPR to changes in the refractive index of the dielectric medium. The excitation condition of the SPPs can be determined from the dispersion relation and the resonance condition given in Eq. (2.94).

The Kretschmann configuration (Fig. 3.1) is the most commonly used approach for the angle-resolved SPR biosensors (6). Optical excitation of surface plasmon is achieved with the use of a prism coupler and the attenuated total reflection method (ATR)(see section 2.5.1.5). Here, a high refractive index prism is coupled with a metal-dielectric waveguide consisting of thin metal film and a dielectric medium in a fluid cell. The thickness of the metal film

determines the coupling of SPPs with maximum of almost 100% efficiency and a sharp minimum in the reflected intensity curve is observed. The dielectric medium consists of a matrix which contains immobilized ligand to interact with the other biomolecules called analyte flowing through the fluid cell. The interaction of analyte with the ligand causes a variation in the refractive index of the dielectric medium (matrix) which is monitored with SPR sensor. When a *p*- polarized light wave is incident through a prism with changing incident angles on the metal film, a dip in the reflected spectrum is observed at a resonance angle. The resonance angle is highly dependent on the optical properties of the dielectric medium in the vicinity of the metal film. The changes in the refractive index of the dielectric medium shift the resonance angle at the reflected spectrum.

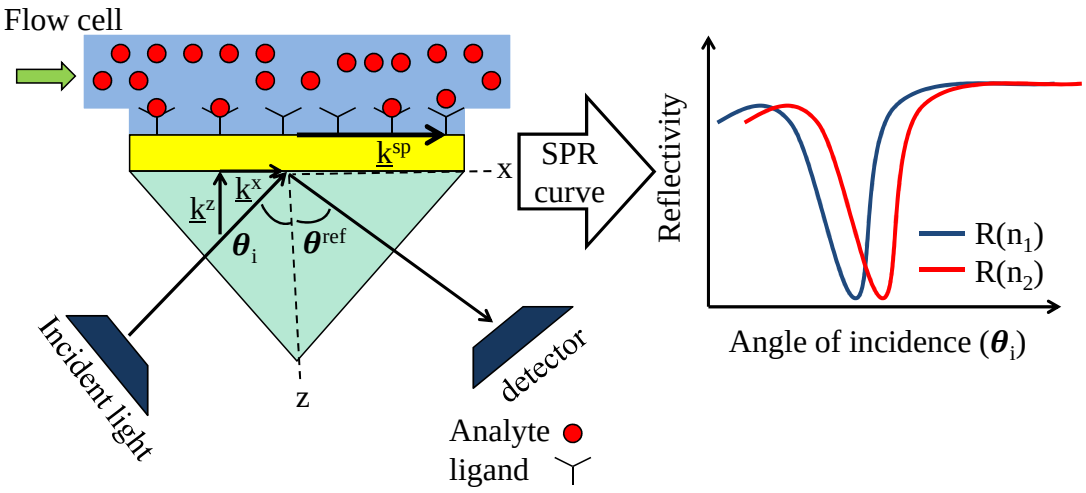

Figure 3.1: Principle of a SPR based biosensor in Kretschmann configuration. The refractive index (n) of the medium above the gold (Au) film is detected by using the *p*-polarized incident light.

This chapter studies the design features of a SPR sensor such as the film thickness, field enhancement, field penetration depth, and sensitivity.

3.2 Simulation Setup

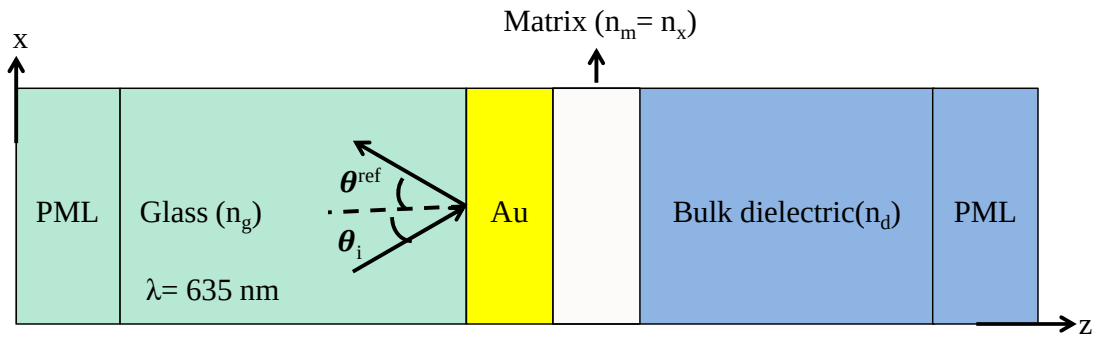

Figure 3.2: Electromagnetic simulation model of a Kretschmann configured SPR biosensor with matrix.

Electromagnetic simulations are performed for a Kretschmann configured SPR biosensor (Fig. 3.1) by using FIT employed in CST MWS solver. The simulation setup of the SPR biosensor is shown in Fig. 3.2. The fluid cell and the prism are modeled as a semi-infinite bulk dielectric medium with a refractive index of $n_d = 1.33$ and a glass medium with a refractive index of $n_p = 1.515$, respectively. The semi-infinite media are mimicked by using perfectly matched layer (PML) boundary conditions interfacing with the glass and bulk dielectric media in the computational domain, which absorbs all the waves entering into it (see section 2.6.1.1). Fluid cell contains a layer of ligands where a change of the refractive index is observed for biosensing. The layer of ligands is modeled as matrix layer with a finite thickness in the simulation setup. The gold layer is used in a simulation as a functional metal layer for the generation of SPPs in the SPR biosensor. The complex frequency-dependent optical property of the gold medium is taken as $\tilde{n}_{Au} = 0.2973 + 3.3299i$ at a wavelength of 635 nm (19). In order to save the time and memory of the simulation, the problem is restricted to 2 D by applying periodic boundary conditions (PBCs) along the x and y-directions of the computational domain (see section 2.6.1.1). The width of the computational domain is taken as 200 nm and 10 nm along the x and y-directions, respectively. The source is excited by using a waveguide port, which also absorbs and measures the reflected

amplitudes(see section 2.6.1.2). In order to excite a plane wave, the waveguide port is placed in the glass prism medium before PML boundary conditions along the z-direction and is extended in the x and y-directions of the computational domain, where PBCs are applied. The material property of the waveguide port is taken similar to the prism (i.e. $n_p = 1.515$) so that there would not be any reflection coming from the boundary of the waveguide port itself. The system is excited with a p-polarized (TM-wave) light having a wavelength of $\lambda = 635\ nm$ in vacuum propagating along the z-direction. For the illumination of the plane wave source, the waveguide port is placed at a distance of two wavelength in the prism medium (i.e. $2\lambda_p = 838.28\ nm$) above the gold film. The reflected intensities are computed for the incident wave at several oblique angles. The mesh is discretized to 1 nm in the gold film and at the interfaces of the medium.

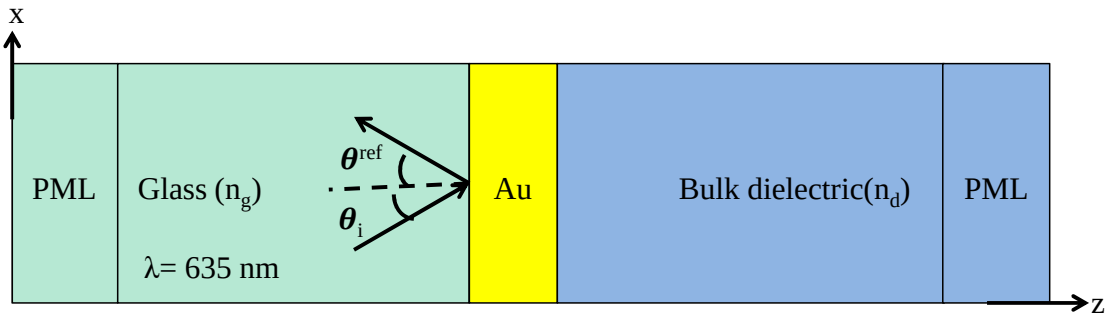

Figure 3.3: Simulation model of a Kretschmann configured SPR sensor without matrix.

3.3 Results and Discussion

3.3.1 Benchmark

As a benchmark, the simulation result of a $3D$ FIT is compared with the analytical solution (obtained from Eq. (2.97)) of a Kretschmann configured SPR system (glass/metal/dielectric (n_d)). The analytical solution is obtained from a Fresnel‘s equations for three-layer model in the ATR configuration (see section 2.5.1.5). The thickness of glass and the bulk dielectric

medium are taken as semi-infinite whereas the thickness (d) of sandwiched metal film is 50 nm (see Fig. 3.3). The material parameters are chosen as $n_p = 1.515$ ($\varepsilon_p = 2.295$), $\tilde{n}_{Au} = 0.2973 + 3.3299i$ ($\varepsilon_m = -11.0 + 1.98i$) and $n_d = 1.0$ ($\varepsilon_d = 1.0$) for prism, metal and dielectric, respectively. The incident source is a p-polarized light having a wavelength of (635 nm). The reflected intensity of a light is computed as a function of angle of incidence (θ_i) between $40 - 50°$. A dip in the reflected intensity is observed at $\theta_i = 44°$(Fig. 3.4). This dip corresponds to the generation of surface plasmon polaritons with air as a bulk dielectric medium. For comparison, the simulation is performed for the similar setup with FIT. The plane wave source ($\lambda = 635\ nm$) is incident from a waveguide port on SPR system by sweeping the incident angles from $40 - 50°$. The reflected waves are absorbed and measured by the same waveguide port. Simulated angular reflectivity curve shows an excellent agreement with the analytical result, as shown in Fig. 3.4.

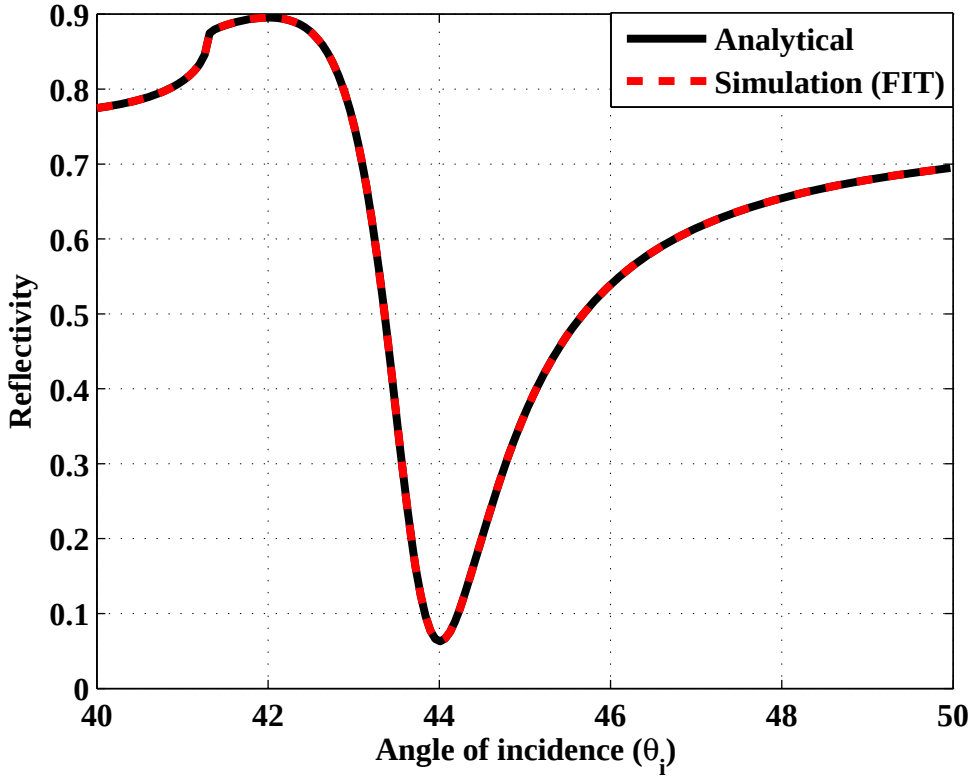

Figure 3.4: Reflectivity as a function of angle of incidence(θ_i) for glass/Au (50 nm)/dielectric ($n_d = 1.0$) structure obtained by FIT simulation (red curve) and by analytical solution (dotted blue curve).

3.3.2 Optimization of metal layer

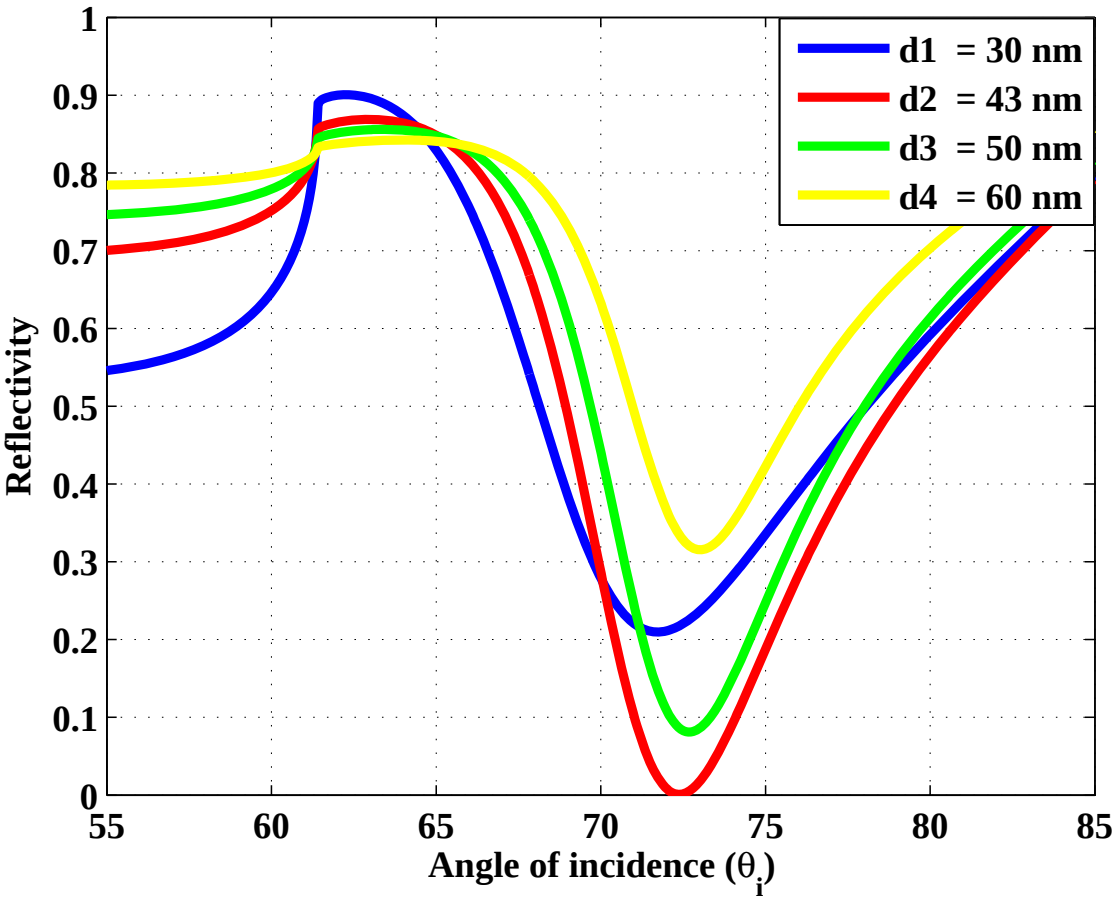

Figure 3.5: Angular reflectivity curves for four different metal film thicknesses (i.e. 30 nm, 43 nm, 50 nm and 60 nm) with water (n_d=1.33) as a bulk dielectric medium by using 635 nm incident light in a SPR setup.

Thickness of the metallic layer in the SPR system plays a significant role in the performance of the sensor in terms of sensitivity (74; 75). When a light wave is illuminated on the interface of a prism-metal in ATR configuration (see section 2.5.1.5), part of the wave is reflected and the other part is penetrated through the metal film. The penetrated wave couples with the SPPs at the metal-dielectric interface. At a resonance angle (θ_r), the SPPs also radiate back into the prism due to the leakage radiations. The light wave which reflects back from the prism-metal interface and the wave which is radiated from the SPPs

destructively interfere with each other at an optimum thickness of the metal layer. This destructive interference cause a sharp dip in the reflected intensity of the light. Sharp dip means high sensitive sensor, which can be obtained from the optimum thickness of the metal layer. The effect of the thickness of metal film on the resonance angle (θ_r) of the SPR system (glass/Au/dielectric (n_d)) is analyzed for a bulk dielectric with a refractive index n_d of 1.33 by varying the thickness of gold layer (see Fig. 3.3). The angular reflectance of SPR system is calculated for different metal thicknesses from $30\ nm - 60\ nm$. As an explanation, Fig. 3.5 depicts the angular reflectivity curve for only four different metal thicknesses (i.e. 30 nm, 43 nm, 50 nm, and 60 nm). As shown in Fig. 3.5, the full width at half minimum (FWHM) of the reflectivity curve becomes narrow with the increase of the film thickness. It is observed that the small amplitude of the reflectivity curve depends on the thickness of a metal layer. The dip in the angular reflectivity corresponds to the transfer of incident light energy into SPPs and then its dissipation in the planar metal. The strongest coupling of surface plasmons ($R \to 0$) occurs with a metal thickness of 43 nm. Therefore, the optimum thickness of metallic gold layer for the specified SPR setup is found to be 43 nm.

3.3.3 Field analysis

Fig. 3.6 shows the magnetic field distribution of a p-polarized light along the glass/Au (43 nm) /water (n_d=1.33) at resonant angle (θ_r= 72.38°). It depicts the property of an SPP's which is a TM-wave traveling along the interface between gold and water. The electric field is enhanced 2.57 times the incident field from the glass above the gold layer. Most of the field is concentrated in the dielectric medium. The high concentration of the electric field in the dielectric medium shows a way to use SPR setup for sensing purpose.

The intensity distribution of the electric and magnetic fields perpendicular to the interface along glass/gold/water (n_d=1.33) is shown in Fig. 3.7. The intensity is highly enhanced at resonance angle (θ_r = 72.38°) at the interface between gold and water and decays exponentially perpendicular towards both media. The electric field intensity enhancement is computed as 16.57 times higher than the intensity of the incident electric field. The magnetic field intensity is enhanced to 6.638 times. The propagation length L specifies the attenua-

tion of a SPP which measures the energy decay of SPP along the propagation direction (see section 2.5.1.2). It is computed from Eq. (2.91), and is given as 2.03 μ m along the interface of gold and water (n_d=1.33). The penetration depth measures the decay of the field in the metal and dielectric medium (see section 2.5.1.3). The penetration depth Lp is computed from Eq. (2.92) and Eq. (2.93) for metal and dielectric, respectively. It is given as 28 nm and 174 nm for gold and water (n_d=1.33), respectively. This specifies the interface sensitivity of an SPR sensor, as the electromagnetic field is present close to the interface. Hence, the change in the material property of the dielectric medium is only measurable within the range of the penetration depth of the SPP field in an SPR sensor.

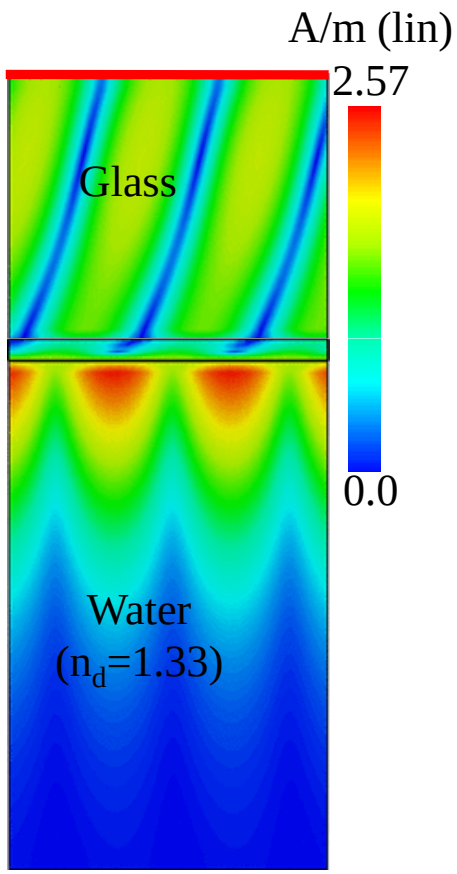

Figure 3.6: Magnetic field distribution along X and Z-directions of glass/Au (43 nm)/water (n_d=1.33) at resonance angle (θ_r) = 72.38°.

a)

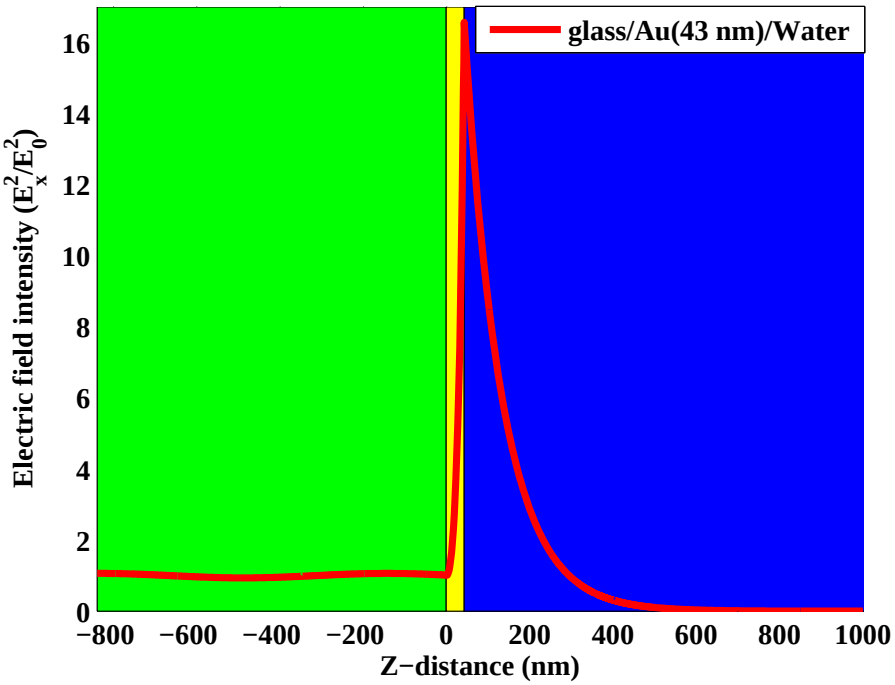

b)

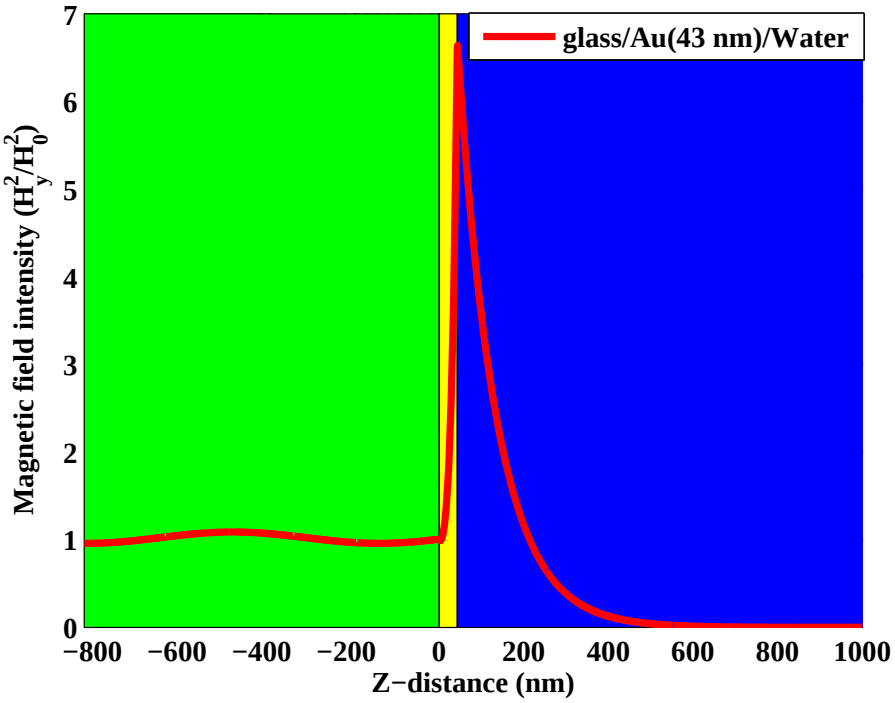

Figure 3.7: (a) Electric field intensity distribution along the Z-direction of glass/ Au(43 nm)/ water(n_d=1.33) at resonance angle (θ_r) = 72.38°. (b) Magnetic field intensity distribution along the Z-direction of glass/ Au(43 nm)/ water(n_d=1.33) at resonance angle (θ_r) = 72.38°.

3.3.4 Sensitivity

To compute the bulk sensitivity of a SPR sensor, the refractive index of a bulk dielectric medium is changed from $n_d = 1.33$ to $n_d = 1.34$ (see Fig. 3.3). Then the angular reflected intensity is computed for a SPR system (glass/Au (43 nm)/dielectric (n_d)), as shown in Fig. 3.8. The resonance angle (θ_r) of both media is given by the angular position of the dip in the reflectivity curve. The intensity modulation sensitivity ($\eta_{intensity}$) of a SPR sensor is computed from Eq. (2.103). Here, S is the amplitude of the reflectivity curve, the angle of incidence ($\theta_i = 69.81°$) at which the angular slope of the reflectivity is maximum, and the resonance angle (θ_r) takes the displacement of 1.43° for a change of the bulk refractive index from 1.33 to 1.34. The intensity sensitivity is then given as 33 RIU^{-1} with a refractive index change of 0.01 (1.33 − 1.34) for a given SPR sensor at a fixed wavelength (635 nm).

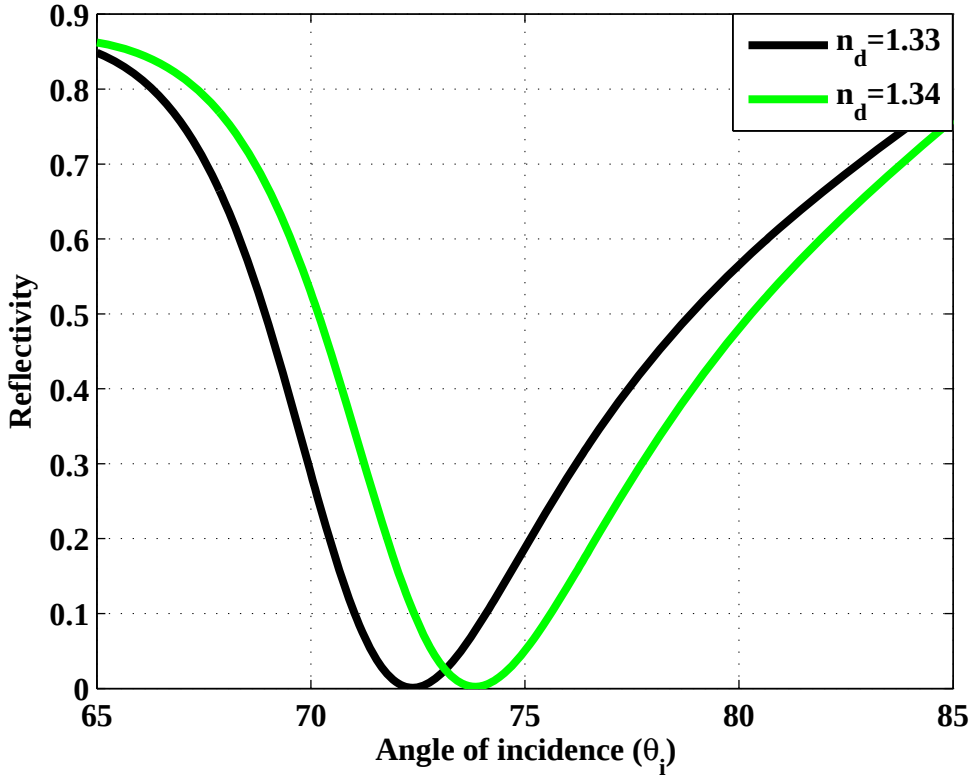

Figure 3.8: Angular reflectivity curves for bulk dielectric media (n_d) of 1.33 and 1.34 in a SPR configuration (glass/Au(43 nm)/dielectric(n_d)) with λ=635 nm.

3.3.5 SPR as a biosensor

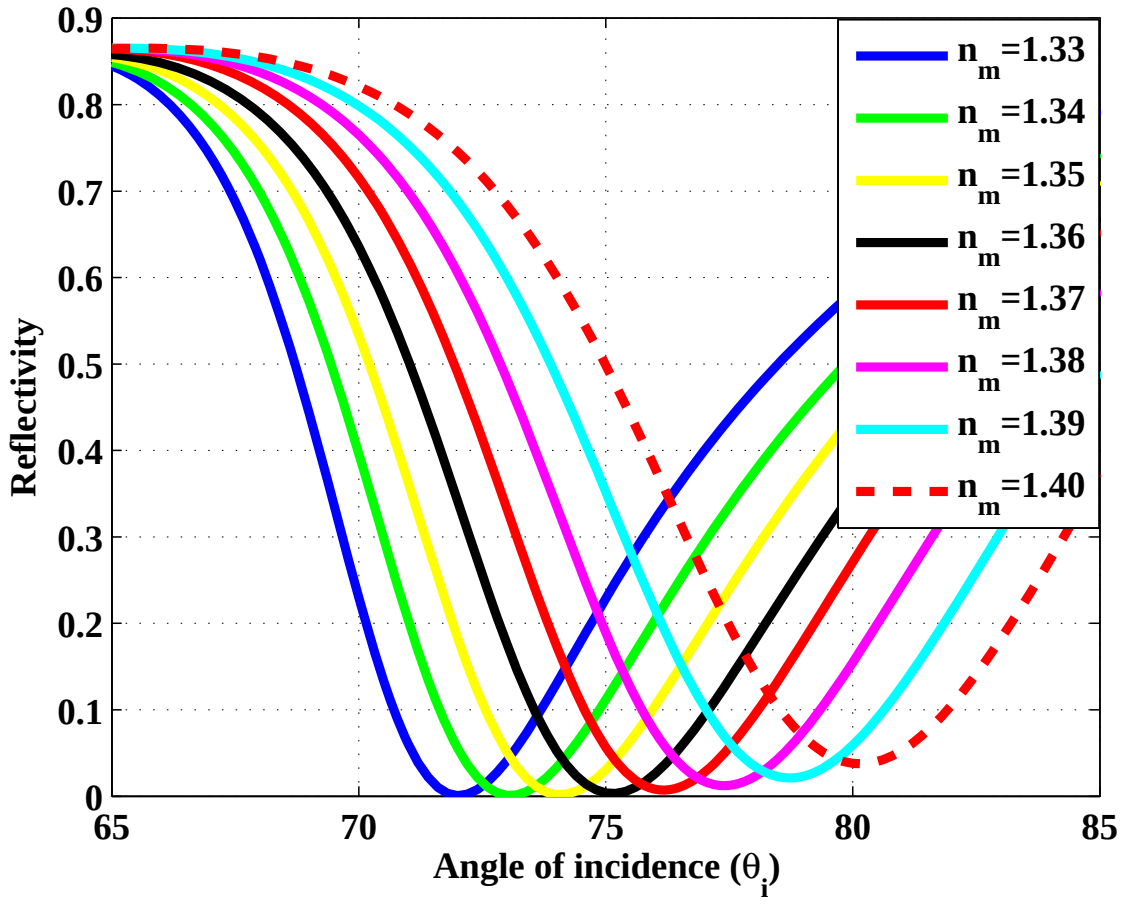

Figure 3.9: Angular reflectivity curves for the glass/Au(43 nm)/matrix(100 nm)/dielectric(n_d) SPR system as a function of incident angles ($65-85^{\circ}$) by varying the refractive index of the matrix (n_m) from $1.33-1.37$ with a variation of 0.01.

In SPR biosensors, the biomolecules are detected, when such biomolecule bind to the receptors (ligands). The interaction of biomolecules with the ligands varies the refractive index of the medium adjacent to the metal layer. This change in the refractive index of the adjacent medium causes a change in the propagation constant of SPPs. Due to this, momentum matching occurs between the propagation constant of the incident light and the SPPs at different angle. As a result, the resonance angle (θ_r) appears at position in angular reflectivity curve. Therefore, biomolecules can be detected from the position of the resonance angle (θ_r)

at the angular reflectivity curve for a given SPR setup.

For a biosensing approach, the refractive index of a matrix layer is varied from $n_m = 1.33$ to $n_m = 1.40$ with a change of $\Delta n_m = 0.01$ in Fig 3.2. The angular reflectivity is computed from $65 - 85^\circ$ as shown in Fig. 3.9. The angular reflectivity curves show that the resonance angle (θ_r) shifts to the right with the increasing refractive index of the matrix (n_m). Hence, the coupling of surface plasmon occurs with the light at higher incident angles (θ_r) for high refractive index mediums at a wavelength of 635 nm. It is also observed that the full width at half minimum (FWHM) of the reflectivity curve is increased at high refractive indices (e.g. FWHM for a reflectivity curve with $n_m = 1.33$ is 6.1 and for $n_m = 1.40$ is 7.7). An increase in the FWHM leads to a decrease in the sensitivity of an SPR sensor, as it depends on the slope of the measuring signal (76). The change in the FWHM is small (1.26 $times$) for a refractive index change from 1.33 to 1.40, hence it would not put influence in the sensitivity of a SPR sensor. Therefore, the SPR sensor is proved to be a good tool to detect given biomolecules (i.e. proteins).

Chapter 4

Magneto-Optic Surface Plasmon Resonance (MOSPR) Sensor for Biosensing Applications

4.1 Introduction

Surface plasmon polaritons (SPPs) are transverse magnetic (TM) waves propagating along the interface of metal and dielectric medium (77) (see chapter 3). They are excited by the interaction of incident light and the free conduction electron of metal. Highly confined electromagnetic field is generated at the metal-dielectric interface. SPPs have been thoroughly investigated in SPR sensors for biosensing applications (78). SPR sensors have many advantages which include low cost, simplicity, and high performance for the label-free and real-time sensing (13). To increase the sensitivity of SPR sensors for sensing of few concentrations of molecules (e.g., in the range of pM-fM) or single-molecule (i.e., nucleotide polymorphisms in DNA), Sepúlveda et al. (19) in 2006 proposed a modulation technique to use the SPR system with the magneto-optic Kerr effect (MOKE) (see section 2.5.1.6), known as magneto-optic SPR (MOSPR) biosensor. This technique is relied on the variation of wave vector of SPPs with an external magnetic field (13). The MOSPR sensor consists of multilayer structure which contains the ferromagnetic and noble metals such as

Au/Fe/Au (64) and Au/Co/Au (13) to generate large magneto-optic modulation. The gold (Au) noble metal is used due to its chemical stability (13). The ferromagnetic medium Co provide magneto-optic (MO) activity up to 3.2 for $Au(3\ nm)/Co(2.8\ nm)/Au(20\ nm)$ trilayer configuration (79) and trilayer $Au(2\ nm)/Fe(3\ nm)/Au(30\ nm)$ with Fe layer provide MO activity up to 0.01 (64), hence the multilayer configuration with Co layer has larger MO effects. For sensing applications, In (64) reported two fold increment in the sensitivity of the MOSPR sensor with Au/Fe/Au trilayer and (13) reports four fold increment for Au/Co/Au trilyer system as compared to the standard SPR sensor.

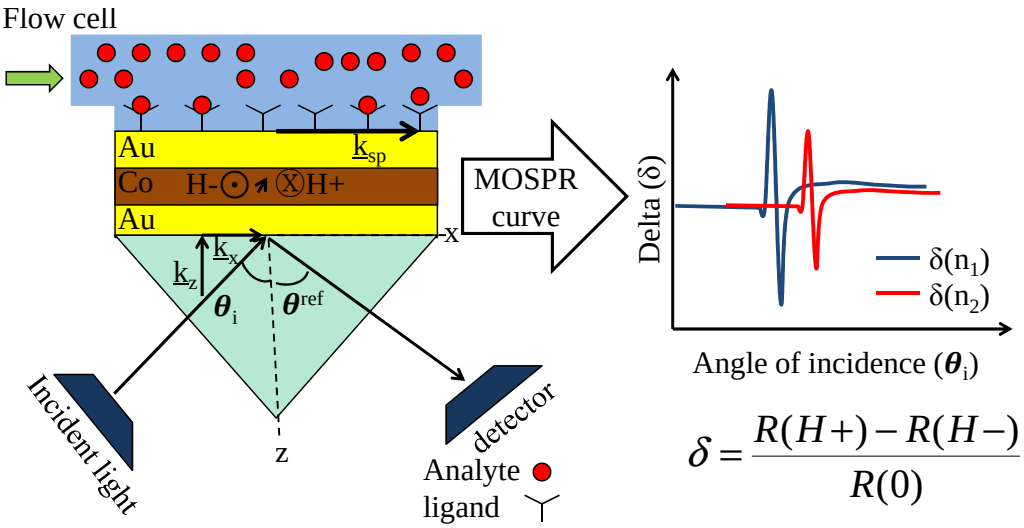

Figure 4.1: Principle of the magneto-optic SPR (MOSPR) based biosensors in Kretschmann configuration. In the MOSPR sensor, the Co layer is magnetized by the external fields $H+$ and $H-$ and the normalized difference of the angular reflectivity ($\delta = R(H+) - R(H-)/R(0)$) is detected as a function of the refractive index (n) of the dielectric (flow cell) (86).

The SPP dispersion relation can be modulated by applying the external magnetic fields to the magnetic layer in a SPR system, perpendicular to the direction of the SPP vector along the surface. By this way, the SPP wave vector can be varied by the magnetic field along transverse geometry. This has been realized for both bounded SPP modes (80) and for symmetric leaky SPP modes (81). The latter SPP modes are of great interest for sensing applications as they excite highly enhanced electromagnetic field at the interface and therefore are sensitive to the interface conditions. The leaky SPP modes can be generated in the Kretschmann setup, where the metallic layers are optically coupled to the

glass prism, as shown in Fig. 4.1. These modes are then excited, when a light is shone on the metal layer through the prism at an angle such that the in-plane propagation constant ($k_{x,glass} = k_0\sqrt{\epsilon_g}sin\theta$) is in agreement with the propagation constant of SPP (k_{SPP}) (See Eq. (2.96)). The leaky SPP modes lose energy because of the absorption in the metals and also because of the leakage radiations which are emitted into the coupled prism. The ferromagnetic metals have high absorption losses (for example absorption coefficient of Co at 635 nm is $8.27 \times 10^5 cm^{-1}$ (82)) compared to the noble metals (for example absorption coefficient of gold at 635 nm is $6.8 \times 10^5 cm^{-1}$ (82)). Therefore, the propagation length of the SPP in the MOSPR configuration($L = 0.92\ \mu\ m$) is 2.2 times smaller than the SPP propagation length obtained with the SPR system($L = 2.03\ \mu\ m$) (See section 4.3.3). Which results in low EM enhancement at the metal-dielectric interface in the MOSPR system as compared to the SPR system. Minimum in reflected intensities are achieved by destructive interference of the leakage radiation and the incident light at boundary of the prism and metal layer (77). The minimum dies out for a particular metal thickness depending on the absorption losses which are related to the 100% efficient SPP excitation and leading to the highly enhanced EM fields. Thus in Kretschmann configuration by incorporating ferromagnetic metals, SPP excitation conditions is changed with the external magnetic field. As a result, a strong variation in the reflectivity curve is observed due to the applied external magnetic field producing enhancement in the transverse magneto-optic Kerr effect (TMOKE) (81; 83; 84) (see section 2.5.1.6). The magneto-optic (MO) effect can be combined with SPPs in the SPR system by introducing a ferromagnetic film in between the two noble metal layers (i.e. Au/Co/Au). The sensor based on the MO and SPP phenomenon is known as magneto-optic surface plasmon resonance (MOSPR) sensor (Fig. 4.1). The delta signal (δ) describes the field dependent variation of the reflected intensity of the system given by Eq. (2.100).

This chapter presents the electromagnetic study of the optimized magneto-optic SPR (MOSPR) sensor and compares it with the SPR sensor (see chapter 3). K*ä*mpf et al. have optimized the MOSPR system (Au (10.75 nm)/Co (6 nm)/Au (20.25 nm)) by using transfer matrix method (TMM) (85). The optimized thickness is obtained when the minimum in the reflected intensity becomes zero at resonance angle with water as a dielectric medium

($n_d = 1.33$), as shown in Fig. 4.5. Following results have been published in (86).

4.2 Simulation Setup

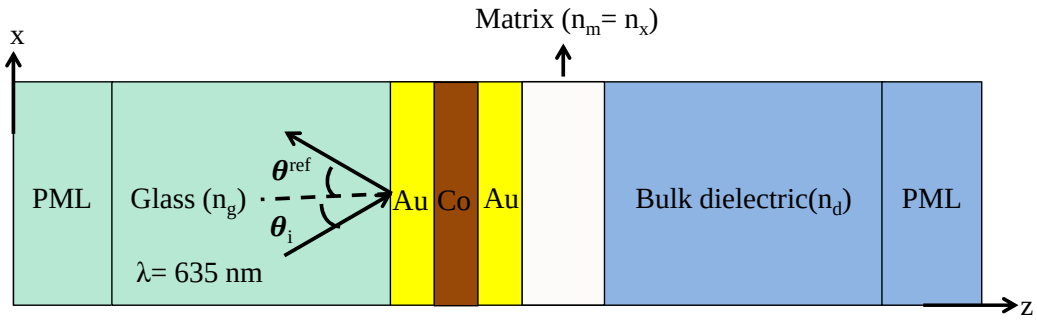

Figure 4.2: Electromagnetic simulation model of a MOSPR biosensor in Kretschmann configuration with matrix (86).

The $3D$ electromagnetic computational model of the optimized magneto-optic surface plasmon resonance (MOSPR) system in the Kretschmann configuration is shown in Fig. 4.2. The MOSPR system replaces the single gold layer in the SPR system with the gold (Au)/ Cobalt (Co)/ gold (Au) layer for the magneto-optic effect. The simulation model of the optimized MOSPR system consists of glass/Au/Co/Au/matrix/dielectric film. The glass and dielectric layers are chosen to be semi-infinite layers whereas the thickness of the matrix layer is chosen to be finite (i.e. 100 nm). The simulation study is performed for the optimized Au (10.75 nm)/Co (6 nm)/Au (20.25 nm) layer system. The system is excited by a p-polarized light with a wavelength of $\lambda = 635$ nm for various incident angle (θ_i). The infinite computational domain is restricted with periodic boundary conditions along x- and y-directions for saving computational memory. Absorbing boundary condition known as perfectly matched layer (PML) is applied along z-direction of the computational domain. The semi-infinite glass and the dielectric (i.e. water) layer are selected with a refractive index (RI) of n_g=1.515 and n_d=1.33, respectively. The complex frequency dependent dielectric property of the gold medium is obtained from the Drude model (19). Hence, the complex refractive index of the

gold (Au) medium is given as $\tilde{n}_{Au} = 0.2973 + 3.3299i$ ($\varepsilon_m = -11.0 + 1.98i$) at a wavelength of 635 nm (19). The anisotropic material parameters for the cobalt (Co) medium magnetized in y-direction is acquired by using the tensor formula along the transverse geometry given in Eq. (2.101). The material parameters i.e. $\tilde{n}_{Co} = 2.2382 + 4.0546i$ ($\varepsilon_{Co} = -11.43 + 18.15i$) and the Voigt constant $Q = 0.043 + 0.007i$ are taken from (19; 61). The relative magnetization of the Co layer i.e. m_y is selected to be $+1$ and -1 for the magnetization along the opposite y-directions. Any variations in the RI of the matrix layer is detected in a bulk environment with a constant RI (i.e. n_d=1.33) for biosensing applications.

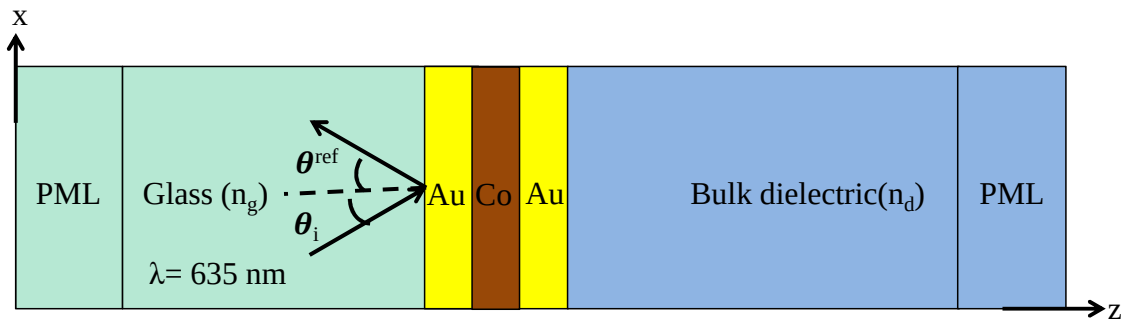

Figure 4.3: Simulation model of a MOSPR sensor in Kretschmann configuration without matrix.

4.3 Results and Discussion

4.3.1 Air as a dielectric medium

The simulation is performed for an optimized MOSPR system (glass/ Au(10.75 nm)/ Co(6 nm)/ Au(20.25 nm)/ dielectric (n_d)) in Kretschmann setup by using $3D$ FIT (see Fig. 4.3). The bulk dielectric medium (n_d) is chosen to be air (n_d= 1.0). The system is excited with a p-polarized light having a wavelength of 635 nm for incident angles ranging from $38-50°$. First, The MOSPR system is simulated with Co having no applied external magnetic field i.e. m_y = 0. Due to this, the Co tensor has only diagonal components in the tensor formula given in Eq. (2.101). It means there is no magnetic component in the Co material. Then, the angular

reflectivity $R(0)$ is computed without including magnetization component. After that, the magnetic effect is included in the Co film by using $m_y = +1$ in the positive y-direction. With this, the off diagonal elements are also included in the Co tensor for transverse geometry. The angular reflectivity $R(H+)$ curve is simulated which include the effect of external magnetic field in one direction along say positive y-direction. The angular reflectivity $R(H-)$ curve is computed which include the effect of applied external magnetic field in the opposite direction say negative y-direction. The external magnetic field is included in the simulation by putting $m_y = -1$ in the tensor formula. We calculate the delta signal as a function of angle of incidence from the angular reflectivity information with and without magnetization by using Eq. (2.100). The angular reflectivity curves ($R(0)$,$R(H+) and R(H-)$) are shown in Fig. 4.4(a), the inset plot shows the zoomed curves for angular reflectivity obtained in the normal plot for MOSPR system (Au(10.75 nm)/Co(6 nm)/Au(20.25 nm)) with air (n_d=1.0) as a dielectric medium (n_d) from $38 - 50°$.

The reflectivity curves (R(0), R(H+) and R(H-)) are also obtained from the experiment for the MOSPR system with air as a dielectric medium (Fig. 4.4(b)). Experiments are performed by our experimental partners at the physics lab of the University of Kassel (86). In the experimental setup, the Au (10.75 nm)/Co (6 nm)/Au (20.25 nm) layer system is deposited on a $BK7$ glass ($n_g = 1.515$) substrate with RF sputtering with a base pressure in the range of 10^{-4} Pa. The gold and cobalt layers are deposited at the rate of 1.1 nm/min and 0.3 nm/min, respectively. The Kretschmann configured MOSPR measurements are performed by using a home built setup with a p-polarized light from a diode laser. The glass substrate is coupled to a half-cylindrical prism ($BK7$) by refractive index matching liquid and mounted on a rotation stage with an angular step size of 0.01°. The Co layer is magnetized by applying the external fields $H+ = 40$ mT and $H- = -40$ mT.

The results for the delta (δ) signal obtained from the reflectivity informations of experiments and simulation are compared as shown in Fig. 4.4(c). The typical shape and angular position of the experimental delta (δ) signal is in agreement with the simulated one, whereas, the amplitude of the signal differs by approximately three times. This can be due to the fact that surface (or interface) roughness is not considered in the simulations for metallic layers.

a)

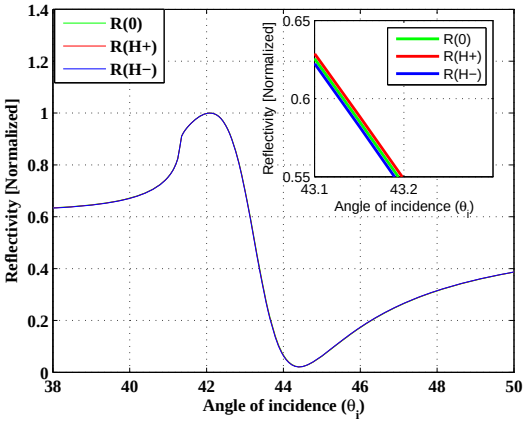

b)

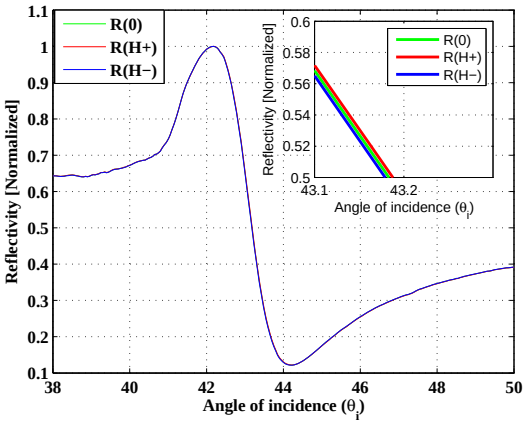

c)

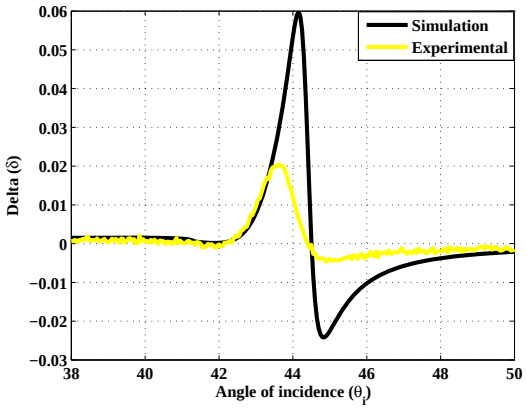

Figure 4.4: MOSPR system (Au(10.75 nm)/Co(6 nm)/Au(20.25 nm)/air($n_d = 1$)): Angular reflectivity curves R(H+), R(H-) and R(0) (a) FIT simulations and b) Experimental (insets are the zoomed plot in (a) and (b)).(c) Comparison of the δ-signals: experimental (yellow) and FIT simulations (green) (86).

4.3.2 Water as a dielectric medium

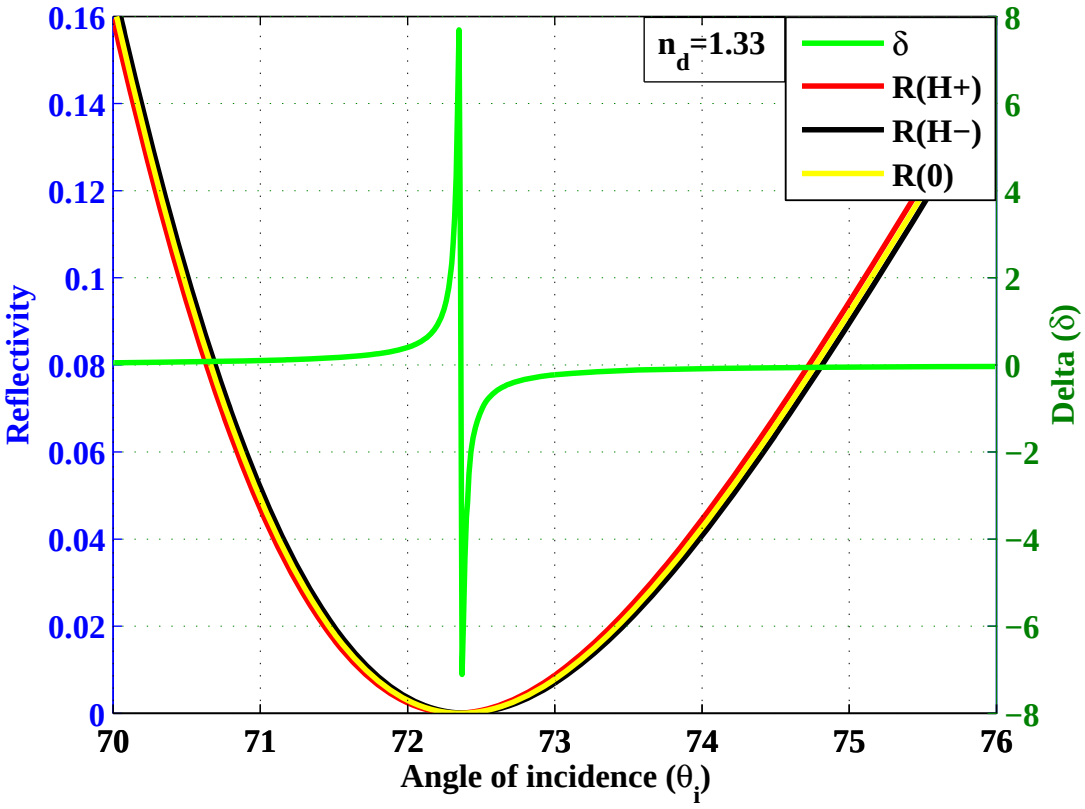

Figure 4.5: Simulation of the optimized MOSPR system (Au(10.75 nm)/ Co(6 nm)/ Au(20.25 nm)) as a function of angle of incidence(θ_i) with water ($n_d = 1.33$) as a bulk dielectric medium: (left y-axis) Reflectivity curves with and without magnetization; (right y-axis) δ-signal (86).

The refractive index of the bulk dielectric medium is changed from air ($n_d = 1.0$) to water ($n_d = 1.33$) in the prism coupled Kretschmann configuration in Fig. 4.3. The optimized thickness of the MOSPR system Au (10.75 nm)/Co (6 nm)/Au (20.25 nm) is obtained, when the reflected intensity is minimum and the magneto-optic effect (i.e., δ-signal) is maximum with water as a bulk dielectric medium ($(n_d = 1.33)$) (85). The optimized MOSPR system is simulated for range of angle of incidence from $70 - 76°$, as shown in Fig 4.5. The reflected intensities are computed with magnetization in opposite directions (i.e., R(H+) and R(H-)) and without magnetization (i.e., R(0)). The drop in the reflected intensities ($R \rightarrow 0$)

are obtained at the resonance angle ($\theta_r = 72.38°$), which corresponds to the generation of SPPs. Due to the magneto-optic effect in the transverse direction, there is a variation in the amplitude of the reflected intensity of an incident light with opposite magnetizations at the ferromagnetic layer, this effect is called transverse magneto-optic Kerr effect (TMOKE) (see section 2.5.1.6). The delta signal (δ) which measures the variation in the amplitude of the reflected intensities with and without magnetization is computed from Eq. (2.100). The sharp δ-signal gives a maximum value of 7.6 for the optimized thickness of MOSPR system (Au (10.75 nm)/Co (6 nm)/Au (20.25 nm) /water ($n_d = 1.33$), which is 2.3 times greater than the reported work of Clavero et al. (79). It is also observed here that the refractive index of the dielectric medium also contribute to the enhancement of the δ-signal. For the same thickness with air as a bulk dielectric medium ($n_d = 1.0$), the maximum value of the amplitude of the δ-signal is 0.06 (Fig. 4.4c), which is 126 times smaller than the δ-signal obtained with water as a bulk dielectric medium (Fig. 4.5).

4.3.3 Field analysis

In the Kretschmann configured SPR system, SPPs are excited at the interface of single metal layer and dielectric medium at the resonance angle, as shown in Fig. 3.6. Similarly, SPPs can also be excited for the trilayer MOSPR system (Fig. 4.3) in Kretschmann configuration. Fig. 4.6 shows the magnetic field distribution of a p-polarized light along the MOSPR system with water as a dielectric medium (n_d=1.33)) at resonant angle (θ_r= 72.38°). It depicts the excitation of SPPs at the interface of bottom Au layer which is 20.25 nm thick and the water. The field is highly concentrated along the water medium. The magnetic field is enhanced 2 times the incident field from the glass above the trilayer (Au/Co/Au). The magnetic field enhancement of the MOSPR trilayer is 1.29 times lesser than the magnetic field enhancement of the SPR system (Fig. 3.6). The reduction in the field can be explained by the fact that the Co has high absorption than the gold layer, which can be obtained from the imaginary part of the refractive index of the complex dielectric medium (see section 4.2).

The intensity distribution of the electromagnetic fields perpendicular to the interface along MOSPR system (glass/Au(10.75 nm)/Co(6 nm)/Au(20.25 nm)/water (n_d=1.33)) are

shown in Fig. 4.7. Like in the SPR system (Fig. 3.7), the intensity of the field is highly enhanced at resonance angle ($\theta_r = 72.38°$) along the interface between bottom Au (20.25 nm) and water medium, and it decays exponentially along trilayer and water medium. The electric field intensity enhancement is computed as 10.7 times higher than the intensity of the incident electric field (Fig. 4.7(a)) and the magnetic field intensity is enhanced to 4.15 times (Fig. 4.7(b)). The electric and magnetic field intensity of the MOSPR system is 1.56 and 1.6 times lower than the SPR system (see section 3.3.3). In order to compute propagation length L of a SPP in a trilayer system, the trilayer system is converted to an effective medium with the effective optical constant retrieved from scattering parameters (87). The retrieved optical constant of the effective medium is $\tilde{n}_{eff} = 0.634 + j3.364$ ($\varepsilon_{eff} = -10.915 + j4.2656$) at a wavelength of 635 nm. The propagation length L is then evaluated from Eq. (2.91), and is given as 0.92 μ m along the interface of effective medium of trilayers and water (n_d=1.33). It is 2.2 times smaller than the propagation length along interface of gold and water (n_d=1.33), which therefore corresponds to the higher attenuation in the trilayer system(see section 3.3.3). The penetration depth Lp (see section 2.5.1.3) is computed as 19.5 nm and 134 nm along the trilayer system (Au/Co/Au) and water (n_d=1.33), respectively. Just as the SPR configuration, the optimized MOSPR setup can also be utilized for effective sensing in the range of approximately 100 nm from the bottom gold layer of the trilayer system. Hence, the maximum magnitude of the δ-signal is not due to the field enhancement at the interface, but it is due to the magneto-optic effect (see section 2.5.1.6).

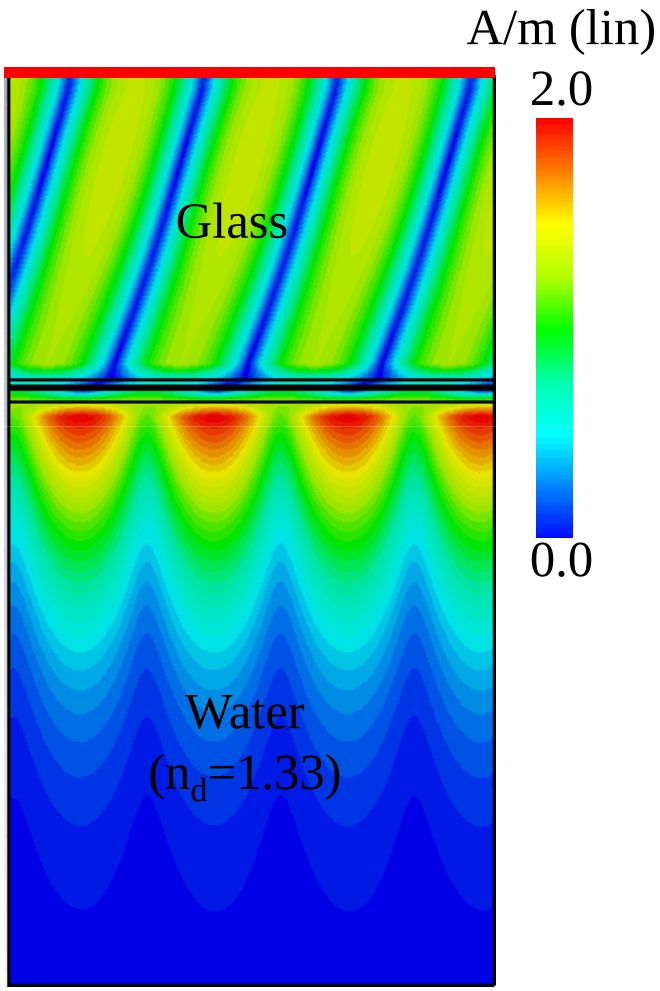

Figure 4.6: Magnetic field distribution along X and Z-directions of the glass/Au(10.75 nm)/ Co(6 nm)/ Au(20.25 nm)/ water (n_d=1.33) at resonance angle (θ_r) = 72.38° (86).

a)

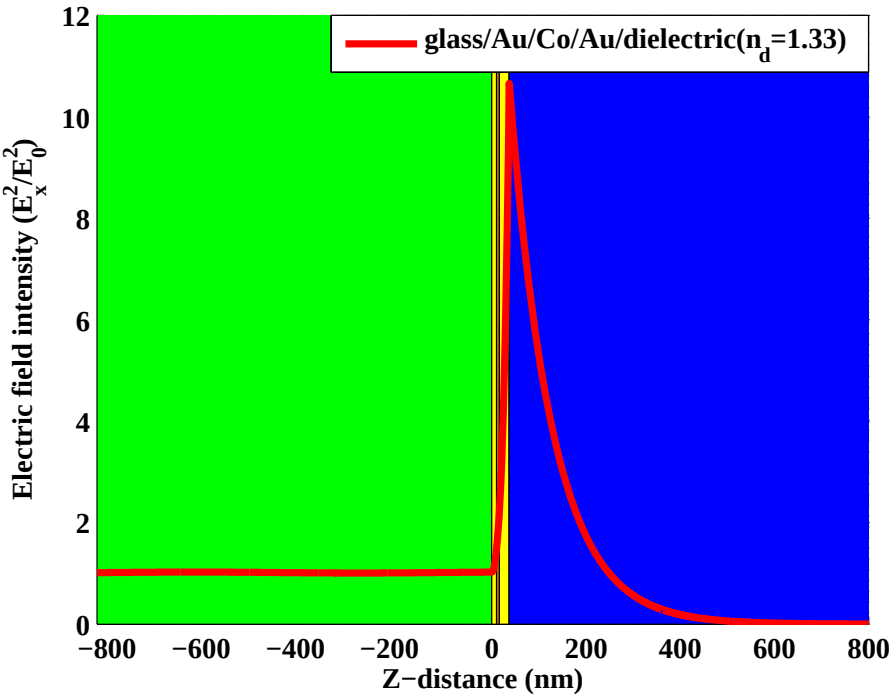

b)

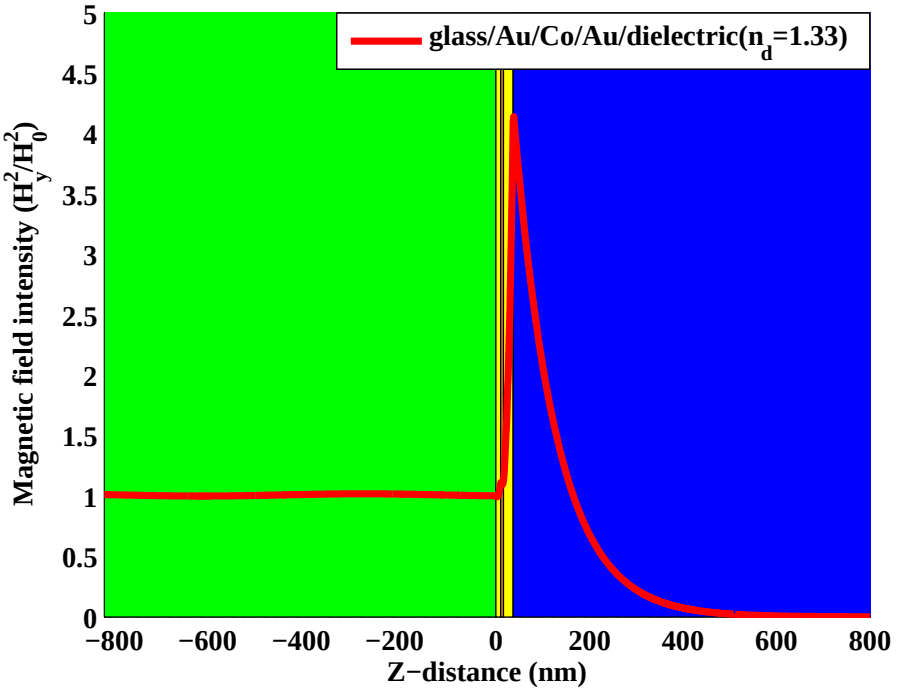

Figure 4.7: (a) Electric field intensity distribution along the Z-direction of glass/Au(10.75 nm)/ Co(6 nm)/ Au(20.25 nm)/ water(n_d=1.33) at resonance angle (θ_r) = 72.38°. (b) Magnetic field intensity distribution along the Z-direction of glass/ Au(10.75 nm)/ Co(6 nm)/ Au(20.25 nm)/ water (n_d=1.33) at resonance angle (θ_r) = 72.38° (86).

4.3.4 Sensitivity

For the calculation of the bulk sensitivity of a MOSPR system (Au(10.75 nm)/ Co(6 nm)/ Au(20.25 nm)/ dielectric(n_d)), simulations are performed for the refractive index of $n_d = 1.33$ and $n_d = 1.34$ (see Fig. 4.3). Angular reflectivity without magnetization (i.e. R(0)) (dashed curve) and the angular delta (solid curve) curves from $(65 - 85°)$ for $n_d = 1.33$ (red curve) and $n_d = 1.34$ (black curve) are shown in Fig. 4.8. Both curves are shifted in the angular position with the change of the refractive index from 1.33 to 1.34, due to the shift of the resonance angle (θ_r). The δ-signal not only shifts in angular position but its amplitude is also reduced 4.3 times with a change of refractive index (1.33-1.34). The intensity modulation sensitivity ($\eta_{intensity}$) of an MOSPR sensor is computed from Eq. (2.103). The ($\eta_{intensity}$) for the δ-signal is then given as 270.6 RIU^{-1} and for reflectivity curve is evaluated as 28.14 RIU^{-1} with a refractive index change of 0.01 $(1.33 - 1.34)$ for a given MOSPR sensor at a fixed wavelength (635 nm). The sensitivity of the optimized MOSPR system for the δ-signal is 8 times higher and for reflectivity is 1.18 times lower than sensitivity of a SPR sensor at 635 nm(see section 3.3.4). Hence the sensitivity of the δ-signal is dependent on the magneto-optic effect.

4.3.5 Biosensing approach

For biosensing experiment of the MOSPR biosensor, the refractive index of a matrix layer is varied from $n_m = 1.33$ to $n_m = 1.40$ with a change of $\Delta n_m = 0.01$ in Fig 4.2. The angular reflectivity is computed from $70 - 85°$ as shown in Fig. 4.9 (a). The angular reflectivity curves show that the resonance angle (θ_r) shifts to the right with the increasing refractive index of the matrix (n_m). Unlike to the SPR biosensor (see section 3.3.5), the full width at half minimum (FWHM) of the reflectivity curve is not changing with the increase of the refractive indices from $n_m = 1.33$ to $n_m = 1.40$. Therefore, ($\eta_{intensity}$) of the reflectivity will be similar from this range of observed refractive index of the matrix ($n_m = 1.33$ to $n_m = 1.40$).

The δ-signal is computed from $70 - 85°$ as shown in Fig. 4.9(b). The δ-signal depicts the decay of amplitude and shift of the resonance angle (θ_r) to the right with the increasing

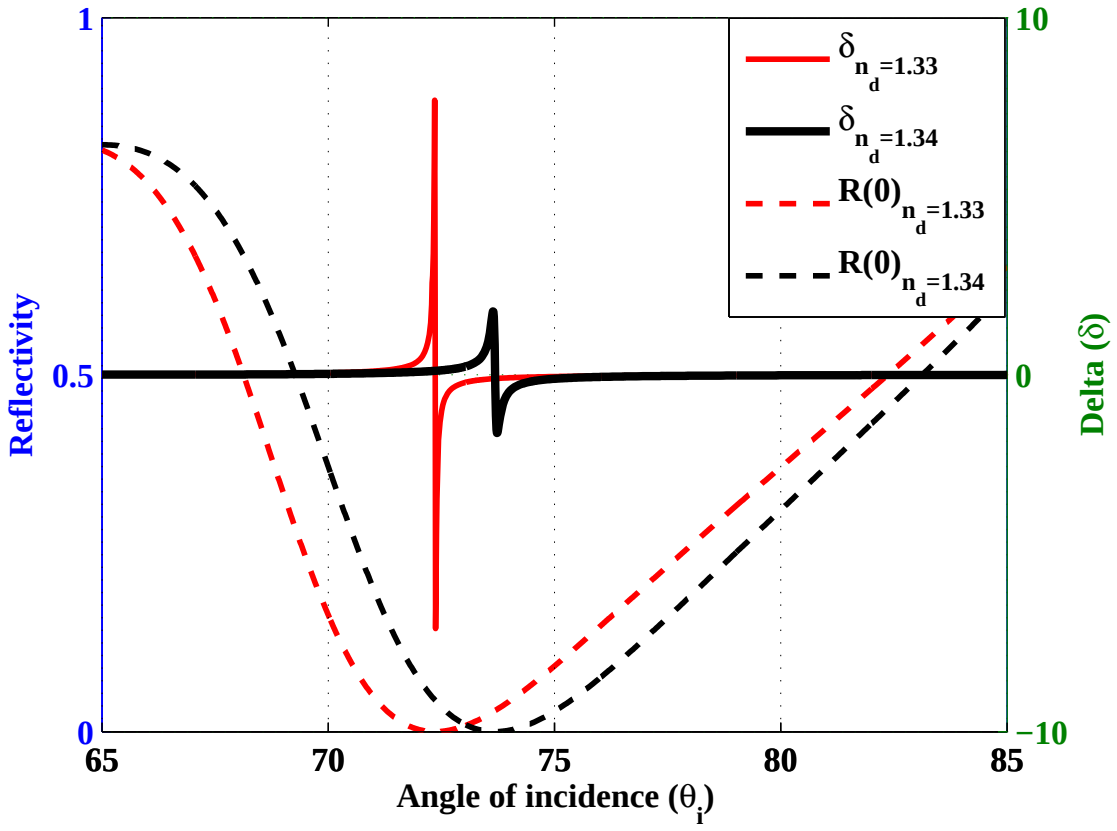

Figure 4.8: Simulation of the glass/Au(10.75 nm)/ Co(6 nm)/ Au(20.25 nm)/ dielectric(n_d) MOSPR system as a function of incident angles ($65 - 85°$) with a bulk dielectric media of $n_d = 1.33$(red) and $n_d = 1.34$ (blue): (left y-axis) Reflectivity curve (R(0)); (right y-axis) Delta(δ) signal (86).

refractive index of the matrix (n_m). The amplitude of the delta signal decays by a factor of 38 for the change of refractive index of the matrix from $n_m = 1.33$ to $n_m = 1.40$. The rapid reduction in the magnitude of the δ-signal limits its usage to short range of refractive index change. Its FWHM is also increasing and as the sensitivity includes the measure of the slope of the signal, therefore, the sensitivity of the δ-signal may also decrease at higher refractive indices. Due to the high sensitivity of the MOSPR it can be used for the lower concentrations of molecule ($<$ 500 g/mol) as an analyte, but is not suitable for longer range of refractive index variation applications.

a)

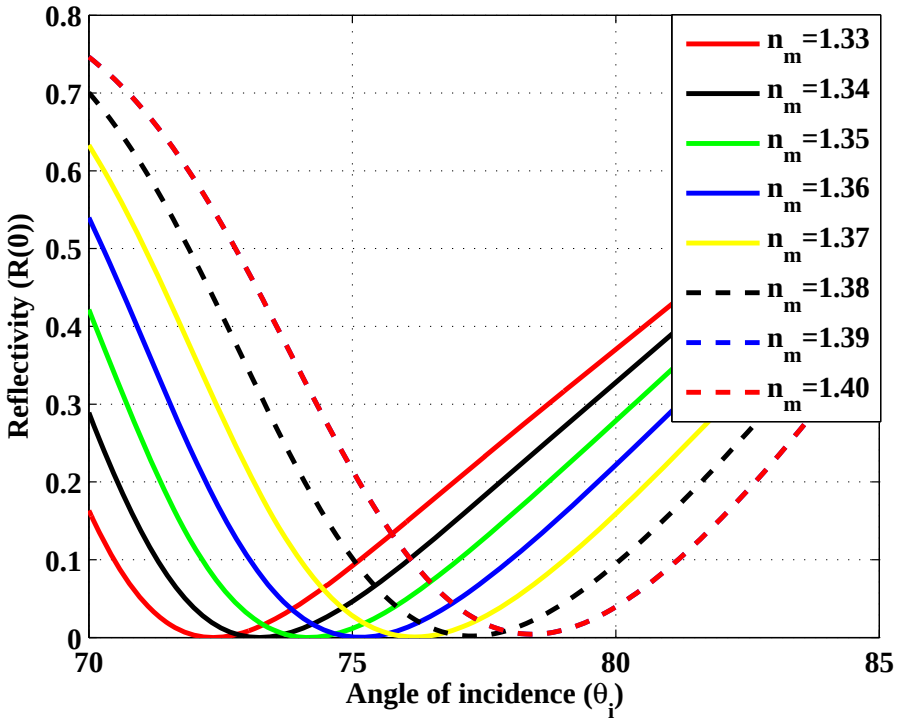

b)

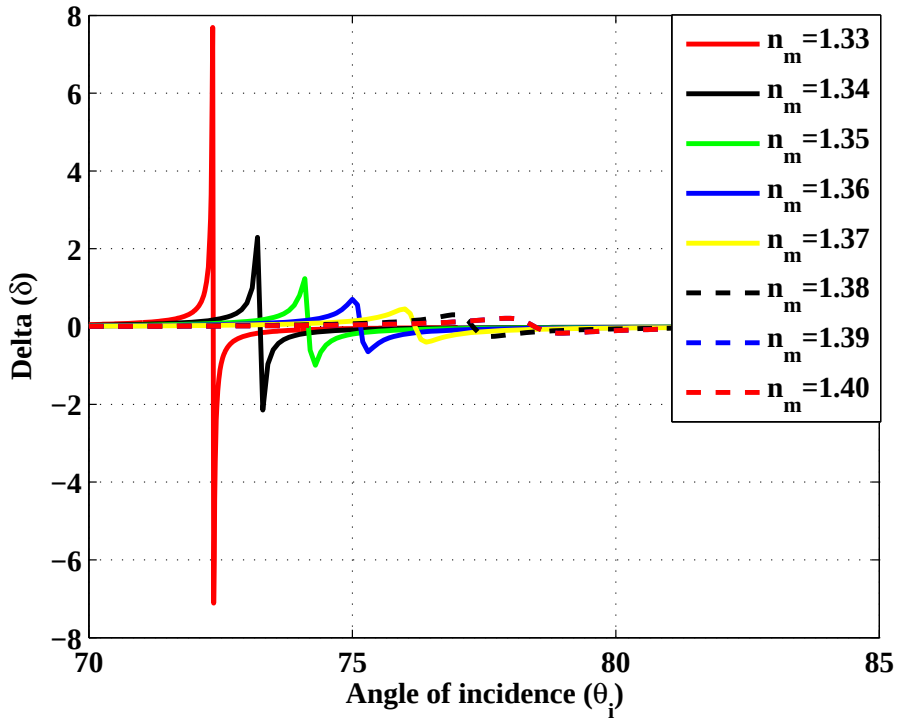

Figure 4.9: Simulation results for the glass/ Au(10.75 nm)/ Co(6 nm)/ Au(20.25 nm)/ matrix(100 nm)/ dielectric(n_d) MOSPR system as a function of incident angles ($70 - 85°$) by varying the refractive index of the matrix (n_m) from $1.33 - 1.34$ with a variation of 0.01: (a) Reflectivity (R(0)); (b) Delta(δ) signal (86).

Chapter 5

Plasmonic Perfect Absorbers (PPA) for Biosensing Applications

5.1 Introduction

As mentioned in the previous chapters, the excitation of the propagating surface plasmons (PSPs) and the localized surface plasmons (LSPs) are highly dependent on the adjacent dielectric medium of the plasmonic systems. The change in the refractive index of the adjacent dielectric medium is analyzed for biosensing purpose.

Plasmonic absorbers are devices used to efficiently absorb electromagnetic energy at the operating wavelengths. They are based on the phenomena of metal-insulator-metal (MIM) waveguide cavity arrays. The MIM waveguide cavity consists of an array of metallic nanoparticles on top and a thick bottom metallic layer separated by a dielectric spacer. When in resonance, the localized surface plasmon resonances (LSPRs) are excited at the nanoparticles. In addition to the localization of the electromagnetic field of single nanoparticle, the field of the other nanoparticles of the array can also interact together and result in a highly localized field in between the nanoparticles. Similarly, the strongly trapped localized electromagnetic field exists if the metallic nanoparticle is placed above the metallic surface. The metallic surface works as a mirror and the localized modes (such as dipole) interact with the induced image in the mirror influencing the resonance. The dielectric spacer between

the metallic nanoparticles and the metallic film acts a cavity to trap the electromagnetic energy caused due to plasmonic and cavity resonances. The devices with MIM waveguide configuration in THz region also known as plasmonic perfect absorbers (PPAs). The PPAs provide high absorption insensitive of polarization directions and angles of the incident light.

Different plasmonic and resonant modes of the cavity can be excited in the PPA system. The first order mode of the system is reported to provide more than 90 % absorption for a wide angle of incidence with both TE and TM polarizations (29). The higher order modes are also excited at shorter wavelengths (88). The plasmonic modes are highly dependent on the adjacent dielectric medium above the nanoparticles (89; 90). The operating resonance wavelength can be obtained by properly engineering the geometry of the PPA structure (29). Thus, the PPA can be utilized for choice of wavelength by modifying the geometrical parameters. The analysis of the existing modes in the PPA system can be exploited for biosensing purpose. Following results have been published in (91).

5.2 Simulation Setup

The geometrical representation of a plasmonic perfect absorber (PPA) biosensor for a wavelength range of $700 - 1400\ nm$ is shown in Fig. 5.1(a). The PPA consists of three operative layers h_1, h_2, and h_3 on a glass substrate with thicknesses 30 nm, 40 nm and 200 nm, respectively. The top layer is made up of a periodically ordered metallic gold nanodisks in two-dimensional having radius ($\Phi = 200\ nm$) and periodicity ($d = 390\ nm$) (See Fig. 5.1(b)). The bottom layer is a thick metallic film used to totally vanish the transmission in the whole spectrum. Thin dielectric spacer film is introduced as a cavity in between the top and the bottom films for the confinement of the electromagnetic field (88). Geometry of the system explains the resonance and angular performance of the structure (89). High absorption can be realized by designing the geometry of the structure accordingly. In this configuration, the electromagnetic field partly lies above the metallic gold nanodisks and in the dielectric spacer region. A change in the refractive index is observed above the metallic gold nanodisk arrays for biosensing purpose.

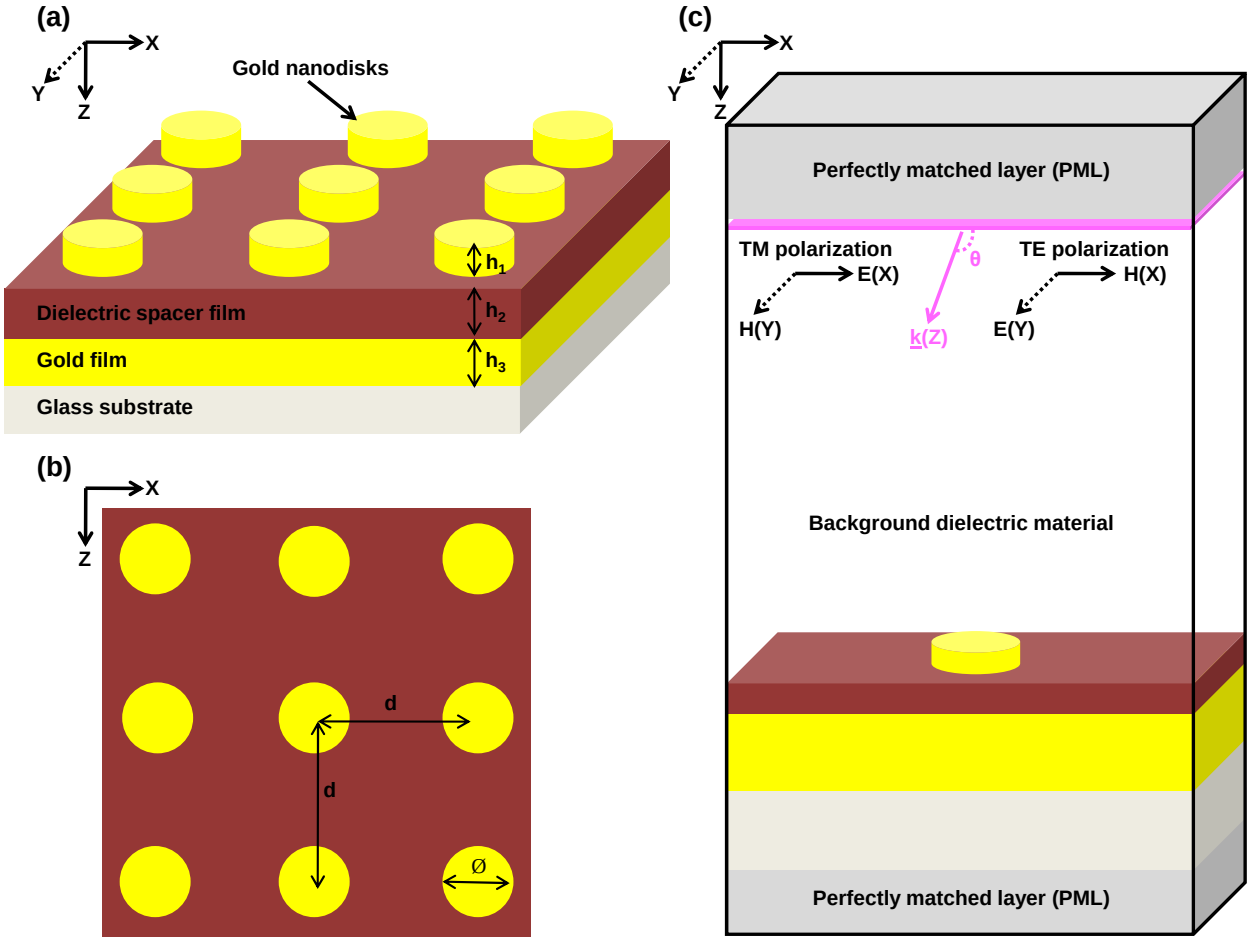

Figure 5.1: (a) Schematic diagram of a plasmonic perfect absorber (PPA) system composed of a $2-D$ periodic array of gold nanodisks ($h_1 = 30\ nm$), dielectric spacer film ($h_2 = 40\ nm$) and gold film ($h_3 = 200\ nm$) on a glass substrate. (b) Top view of gold nanodisks illustrating periodicity ($d = 370\ nm$) and diameter of nanodisks ($\Phi = 200\ nm$). (c) Simulation setup consists of a unit cell of a PPA system with perfectly matched layer (PML) boundary condition along the propagation direction and periodic boundary conditions (PBC) along X and Y- directions (Images are not scaled) (91).

The PPA system is simulated by using 3 D finite integration technique (FIT) to analyze and compute the resonant properties of the structure for biosensing applications. To mimic the periodic arrangement of the gold nanodisks, periodic boundary conditions (PBCs) (2.6.1.1) are applied along the X and Y directions of a single unit cell in the computational domain as shown in Fig. 5.1(c). The perfectly matched layers (PMLs) (2.6.1.1) are used

as an absorbing boundary condition along the propagating direction of the field (i.e. Z-direction). The incident electric field is polarized along the X-direction and the magnetic field is polarized along the Y-direction for transverse magnetic (TM) polarization. Similarly, for transverse electric (TE) polarization the electric field is polarized along the Y-direction and the magnetic field is polarized along the X-direction of the computational domain. The source is placed at $\lambda_{max} = 1400\ nm$ away from the nanoparticles. The dispersive complex dielectric feature of the gold material is obtained from a Drude model with plasma frequency $\omega_p = 1.04 \times 10^{16}\ rad/s$ and collision frequency $\omega_c = 4.89 \times\ 10^{14}\ 1/s$ (19). The dielectric film in between the top and bottom layer uses the material with permittivity (ϵ_r) value of 1.9. In the computational domain, finer mesh (1 nm) is used for modeling objects and their interfaces, while for all other region of computational domain coarser meshes are used to save memory.

5.3 Results and Discussion

5.3.1 Absorption at normal incidence

The plasmonic perfect absorber (PPA) is simulated for a wavelength range of $700 - 1400\ nm$ with the air ($n = 1.0$) as a background dielectric medium above the gold nanoparticles. The unit cell of a PPA is illuminated with TE and TM polarized waves separately at normal incidence propagating along the Z-direction. The response of the PPA for both polarizations at normal incidence is analyzed by simulating reflection (R), transmission (T) and absorption (A) spectrum of the system as illustrated in Fig. 5.2. The absorption spectra is measured from the knowledge of the transmission and reflection spectrum ($A = 1 - T - R$). Fig. 5.2 shows that the transmission is negligible in the given spectrum (i.e., less than 0.0002 %). A dip in the reflection spectrum is observed below 0.3 % at $\lambda = 1040\ nm$, resulting in 99.7 % absorption at normal illumination. Hence, the reflection signal plays a major contribution for the calculation of the absorption signal. A dip in the reflected spectrum corresponds to the confinement of electromagnetic field at $\lambda = 1040\ nm$ in the dielectric spacer region. This is a fundamental mode of the system. The response of the PPA system at normal incidence

is similar for both TE and TM polarizations. The polarization insensitiveness of the PPA is explained by the geometrical symmetry of the system along X and Y- directions.

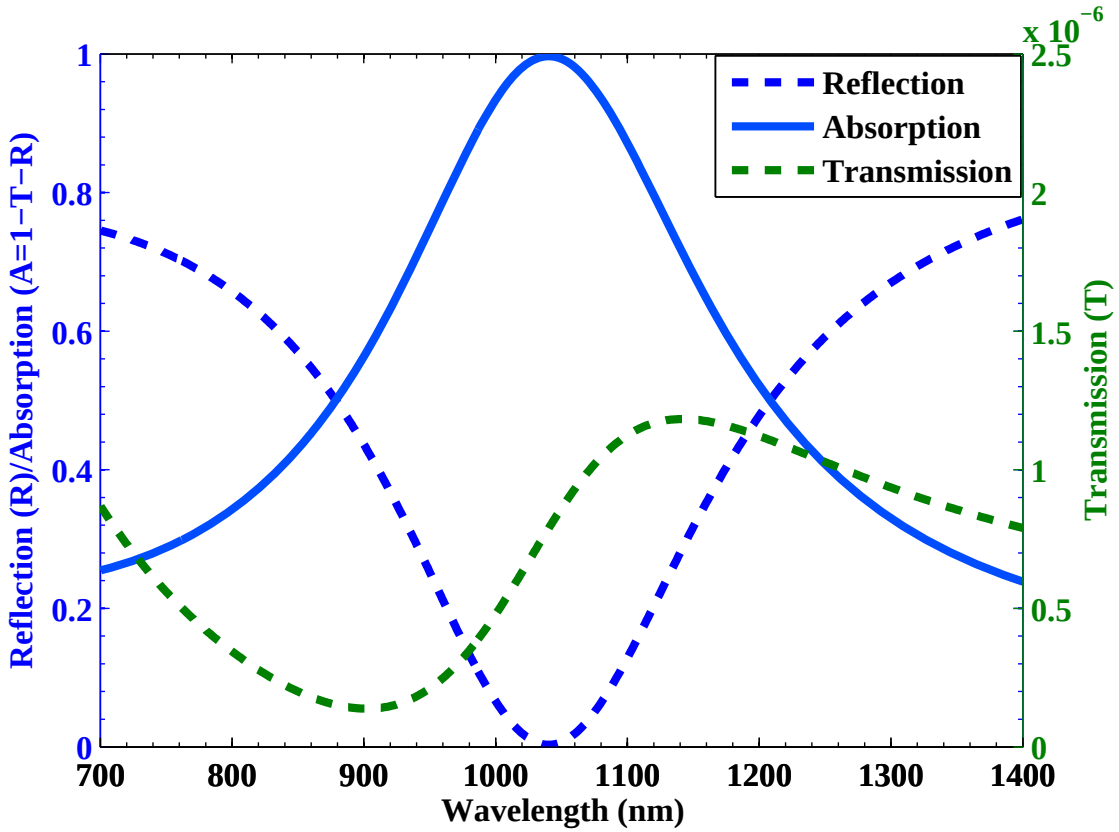

Figure 5.2: Transmission (right, dashed green), Reflection (left, dashed blue) and absorption (left, blue) spectra of a PPA system at normal incidence with air as a bulk dielectric medium for TE and TM polarizations (both polarization have similar characteristics) (91).

5.3.2 Absorption at oblique incidence

The angular feature of the fundamental electromagnetic mode is analyzed at $\lambda = 1040\ nm$ for a wide range of angles of incidence from $0 - 70°$. The PPA system is angularly excited with TE and TM polarized waves in presence of air as a dielectric medium above the nanoparticles. Fig. 5.3 shows the absorption behavior of the fundamental mode at $\lambda = 1040\ nm$ for oblique angles for both polarizations. A nearly perfect absorption is found for TM polarized waves insensitive of incident angles. With TM polarization, the PPA absorbs more than 95 % of the 1040 nm wave for a wide range of incident angles $(0 - 60°)$ and absorbs 92 % of the wave

up to 70°. A high absorption is also observed in the PPA system with TE polarized wave for broad range of angles such as more than 90 % is absorbed till 60° and more than 65 % is absorbed up to 70°. The variation is due to the fact that the magnetic field derives the circulating current efficiently with TM polarization for all angle of incidence, except for TE polarization for wider angles from the normal (28).

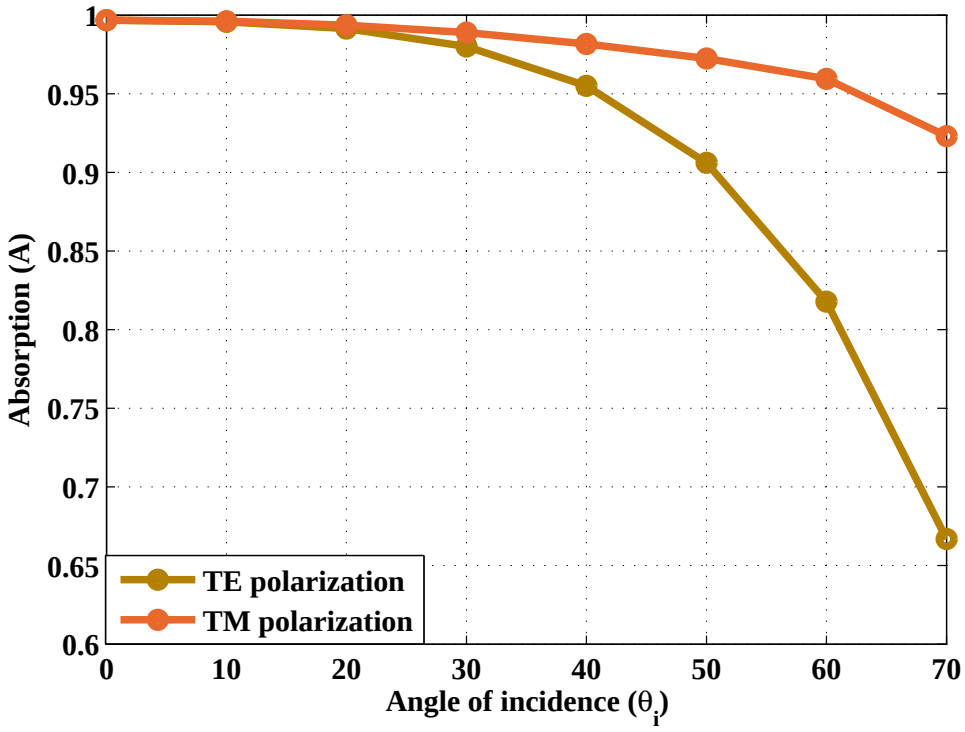

Figure 5.3: Angular absorption of a PPA system from $0 - 70°$ at $\lambda = 1040\ nm$ for both polarizations (TE and TM) with air ($n = 1.0$) as a bulk dielectric medium above the nanoparticles (91).

The angular absorption spectra for a wavelength range of $700 - 1400\ nm$ at various incident angles from $0 - 70°$ are illustrated for TM and TE polarized waves in Fig. 5.4(a) and Fig. 5.4(b), respectively. The fundamental mode reveals nearly perfect absorption for TM polarized waves and provides high absorption for TE polarized waves at $\lambda = 1040\ nm$ independent of angles of incidence. Since the fundamental mode is a broad and it is a polarization and angular insensitive, which is a property of LSPR, hence it suggests that it is a LPSR mode (92).

a)

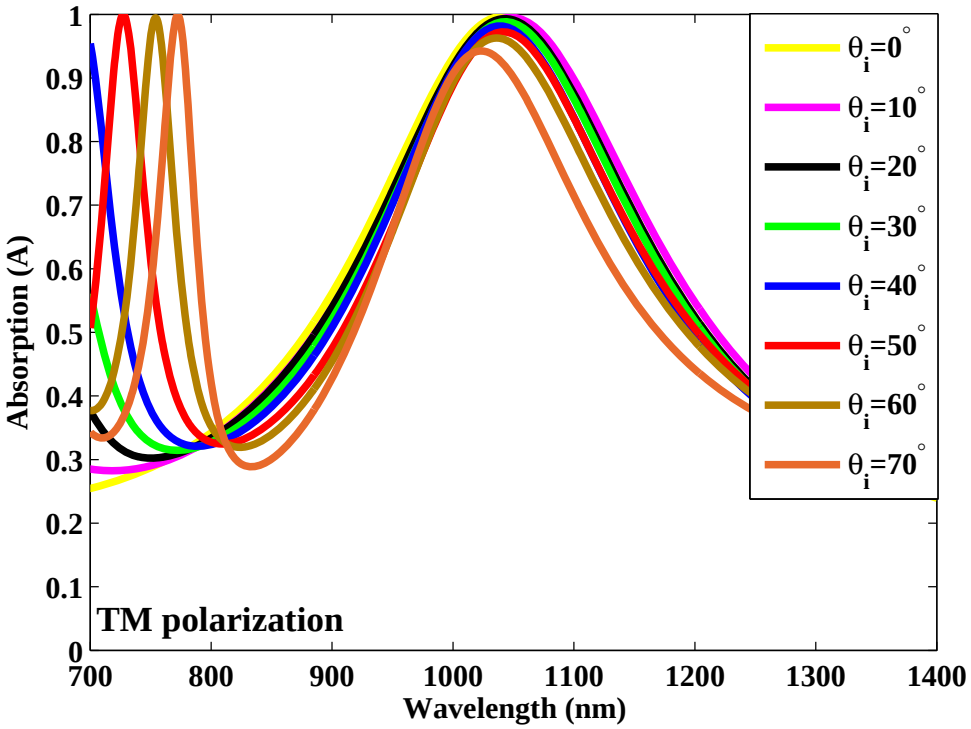

b)

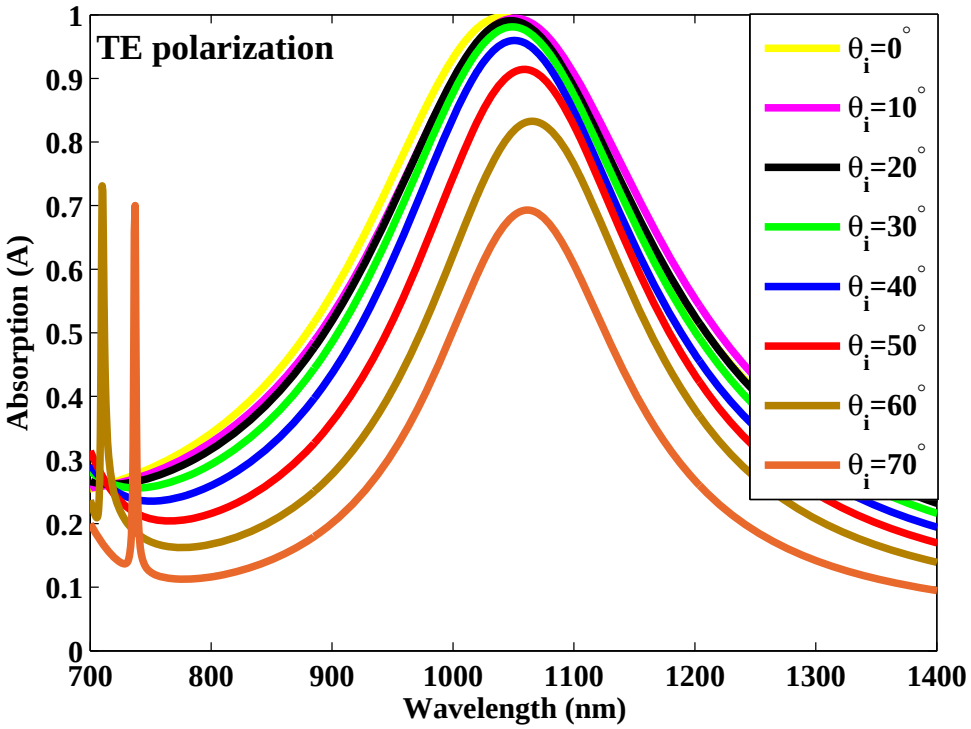

Figure 5.4: Angular absorption spectrum of a PPA system from $700 - 1400$ nm for several incident angles from $0 - 70°$ with air ($n = 1.0$) as a background dielectric medium for (a) TM polarization, (b) TE polarization (91).

The second-order mode can also be stimulated at shorter wavelengths with tilted angles. This mode cannot be excited at normal incidence as it has odd amplitude symmetry and the incident wave is of even symmetry (88). The second-order mode is highly angular dependent unlike the fundamental mode, can be observed in the wavelength range of $700 - 800\ nm$. It also reveals the narrower full width at half maximum (FWHM) as compared to the absorption curve of the fundamental mode of the system. A red shift in the absorption spectra can also be noticed at higher incident angles. Furthermore, it provides perfect absorption at $50 - 70^{\circ}$ incident angles from a wavelength range of $726 - 772\ nm$, respectively. The angular dependent property of the second-order mode reveals that it is SPP type mode (92). The eigen modes of the PPA are theoretically examined. These understandings of the resonant modes are utilized for sensing purpose.

5.3.3 Water as a dielectric medium above nanoparticles

For the analysis of PPA system for biosensing, the bulk medium above the nanoparticle arrays is changed from air ($n = 1.0$) to water ($n = 1.33$). The absorption is computed for air ($n = 1.0$) and water medium ($n = 1.33$) at $\theta_i = 54.1^{\circ}$ for a wavelength range of $700 - 1400\ nm$, a shown in Fig. 5.5(a). The absorption curve is red shifted, when the refractive index is altered from $n = 1.0$ to $n = 1.33$. When the bulk refractive index of the medium is $n = 1.33$, the first-order fundamental mode ($m = 1$) and the second-order mode ($m = 2$) is now moved to longer wavelength i.e. at $\lambda = 1145\ nm$ and $\lambda = 950.9\ nm$, respectively. The second order mode presents 100 % absorption at $\theta = 54.1^{\circ}$ due to the critical coupling (88). Fig. 5.5(b) illustrate the spatial magnetic field distribution through the whole structure for the first order mode ($m = 1$) at $\lambda = 1145\ nm$ and for the second-order mode ($m = 2$) at $\lambda = 950.9\ nm$. With the excitation of the plasmonic resonance modes, the electromagnetic field is highly confined in the dielectric spacer medium and also exists in the medium above the nanoparticles. The electromagnetic energy for the second-order mode is also highly confined above the metallic nanoparticle region i.e., the sensing medium. Therefore, this mode at $\lambda = 950.9\ nm$ is proposed to be utilized for biosensing. The second order mode is chosen for biosensing as it provides angular dependence, perfect absorption,

and high field confinement along the sensing medium. Since, the transmission through the complete spectrum is negligibly small so the reflection curve can only be used for sensing experiment.

a)

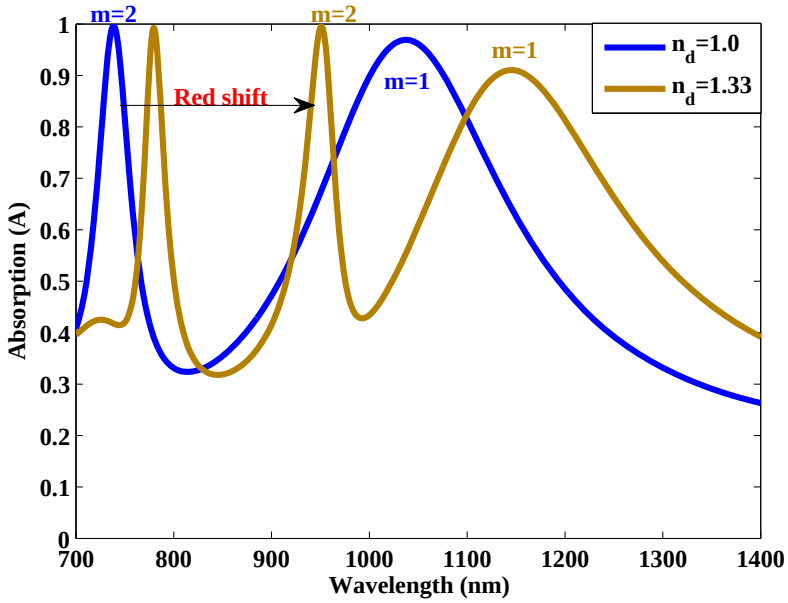

b)

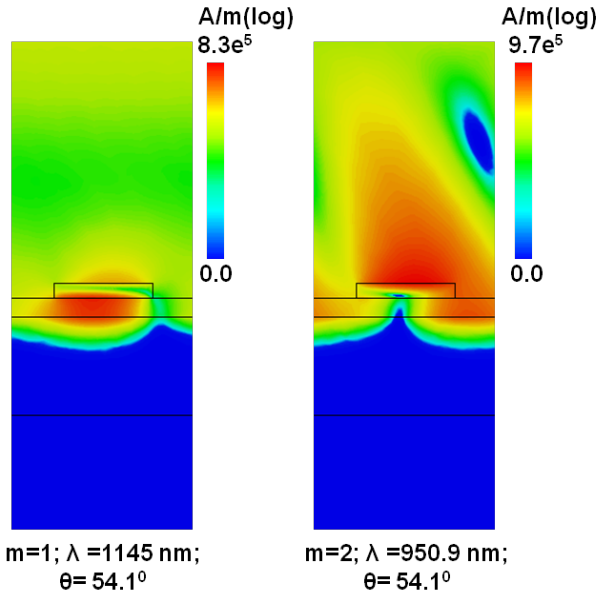

Figure 5.5: (a) Absorption spectra of a PPA system at $\theta_i = 54.1°$ from $700 - 1400\ nm$ with air ($n_d = 1.0$) and water ($n_d = 1.33$) as a bulk dielectric medium (b) Magnetic field distribution along the PPA system. "With kind permission from Springer Science and Business Media: Springer and Plasmonics, 9(6), 2014, 1268, Plasmonic Perfect Absorbers for Biosensing Applications, Abdul Aleem Jamali and Bernd Witzigmann, fig. 5." (91).

5.3.4 Sensitivity

The reflected intensity is simulated for the second-order mode at $\lambda = 950.9\ nm$ with water ($n = 1.33$) as a bulk medium above the nanoparticles for the angle of incidence from $45 - 60°$. A dip in the angular reflectivity curve is observed at $\theta_r = 54.1°$, corresponding to perfect absorption. For the computation of the sensitivity, the angular reflectivity is also computed for the refractive index of 1.34 of the bulk dielectric medium surrounding above the nanoparticle arrays, as shown in Fig. 5.6. The dip of the second order mode is shifted to the left in the angular reflectivity diagram. This shows the high dependence of the second-order resonance on the material above the nanoparticle arrays. Sensitivity is then computed with intensity-interrogation method (see section 2.5.1.7) by using Eq. (2.103). The bulk sensitivity of the PPA is then given as 24.6 RIU^{-1}. The bulk sensitivity of the PPA system is similar to the bulk sensitivity of a SPR sensor which is 33 RIU^{-1} (See section 3.3.4) and is better than the LSPR based biosensors at a fixed wavelength (93). Hence, the PPA has the advantage of SPR sensor providing high sensitivity, and because of the presence of the nanostructures it has the advantage of LSPR sensor being able to determine lower concentrations of biomolecules ($< 1\ ng/mL$).

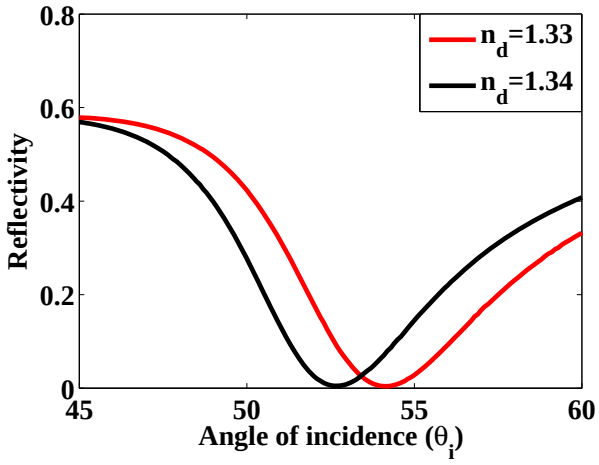

Figure 5.6: Angular reflectivity curves of the PPA system as a function of incident angles ($45 - 60°$) with bulk dielectric(n_d) of 1.33 and 1.34 (91).

5.3.5 Plasmonic perfect absorber (PPA) as a biosensor

In order to have the biosensing experiment, the bulk refractive index above the gold nanoparticle arrays is varied from $n = 1.33$ to $n = 1.40$ with a change of $\Delta\, n = 0.01$. The reflectivity is computed as a function of angle of incidence $40 - 60°$ for refractive index variations. The angular position of the reflectivity dip varies linearly with a linear variation of the refractive index. Unlike the SPR biosensing example (See section 3.3.5), as the refractive index increases the dip moves to the shorter angles. The FWHM for $n_d = 1.33$ is 8.1° and for $n_d = 1.40$ is 5.1°. The reflectivity curve gets narrower at higher refractive indices. As, the sensitivity of a sensor depends also on the slope of the signal, hence the sensitivity of the PPA would becomes higher at higher refractive indices. The results also demonstrate that the PPA system can be used for broader range of refractive indices, as the property of reflectivity curve does not change from $n_d = 1.33$ to $n_d = 1.40$.

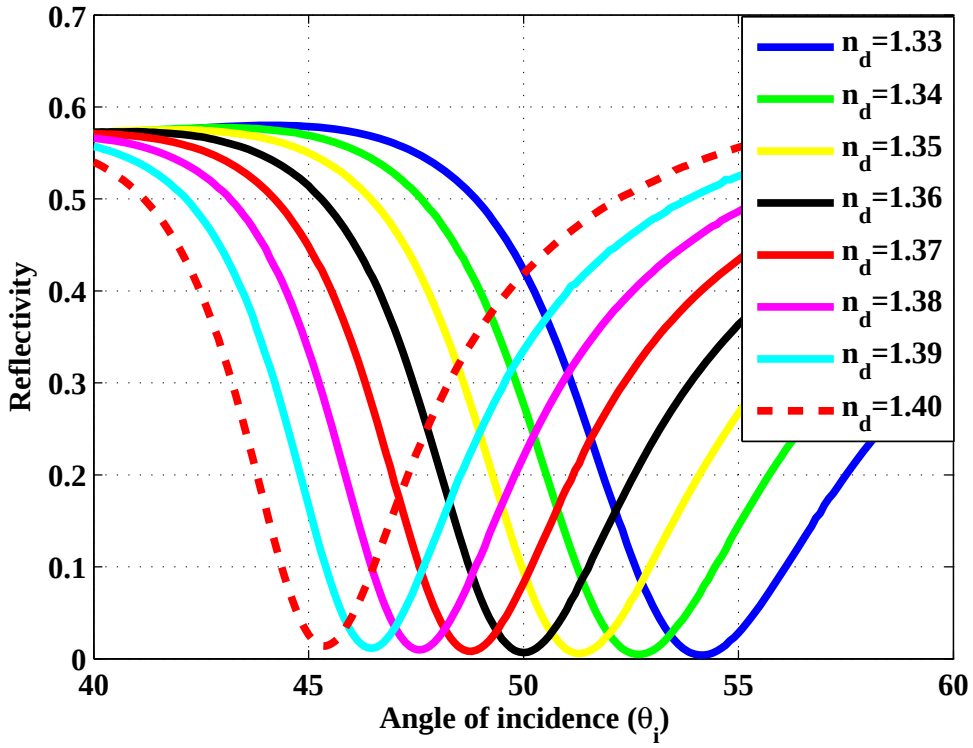

Figure 5.7: Angular reflectivity curves of the PPA system by varying the refractive index above nanodisks (n_d) from $1.33 - 1.40$ with a variation of 0.01 (91).

Chapter 6

Conclusion and Outlook

The objective of this thesis is to study the plasmonic devices thoroughly for biosensing applications. The full 3-D electromagnetic simulations have been performed by using finite integration technique (FIT). The electromagnetic properties of the surface plasmon polaritons (SPPs) and localized surface plasmons (LSPs) are investigated. A novel approach has been given in this thesis for sensing by utilizing the properties of the SPPs and LSPs based sensors.

Chapter 3 analyzes the properties of the surface plasmon resonance (SPR) sensor for biosensing applications. The excitation of the surface plasmon polaritons in the Kretschmann configuration is studied. First, the thickness of the functional gold layer is optimized for the efficient coupling of SPPs at the resonance angle. The optimized thickness of the gold layer is obtained as 43 nm. Then, the field analysis is performed for the optimized thickness of the gold layer with water ($nd = 1.33$) as a dielectric medium. The electric field is highly enhanced (up to 16.5 times) at the interface of gold and dielectric medium. After that, the intensity interrogation sensitivity is computed at a fixed wavelength (635 nm) by changing the refractive index of bulk dielectric medium from 1.33 to 1.34. The sensitivity is computed as 33 RIU^{-1} with a refractive index change of 0.01 $(1.33 - 1.34)$ for a given SPR sensor at a fixed wavelength (635 nm). Then, the biosensing experiment is performed for SPR sensor, where the refractive index of a matrix layer is varied from $n_m = 1.33$ to $n_m = 1.40$ with a change of $\Delta n_m = 0.01$. The angular reflectivity curves show that the resonance angle (θ_r)

shifts to the right with the increasing refractive index of the matrix (n_m). It is also observed that the FWHM of the reflectivity curve is not changing much (only 1.26°) for refractive index range of $n_m = 1.33$ to $n_m = 1.40$.

Chapter 4 studies the properties SPR sensor by including the magneto-optic (MO) effect for biosensing applications. The magneto-optic SPR (MOSPR) system is formed by sandwiching the ferromagnetic layer in between the two gold layers. External magnetic field is applied to the ferromagnetic medium to modulate the properties of the SPR. The results show that the field is also enhanced for MOSPR sensor, but it is 1.5 times lower than the SPR sensor, which can be explained by the high absorption in the Co layer. Similarly like SPR sensor, the bulk sensitivity is computed for MOSPR sensor which is given as 270.6 RIU^{-1}. The MOSPR sensor has 8 times higher sensitivity than the SPR sensor. Due to the high sensitivity, the MOSPR sensor can be able to detect lower concentrations of molecules. The biosensing experiment is also performed for the MOSPR sensor. The refractive index of a matrix layer is varied from $n_m = 1.33$ to $n_m = 1.40$ with a change of $\Delta n_m = 0.01$. The amplitude of the δ- signal is decreasing rapidly with the increase of the refractive index. This drawback of the MOSPR system limits the range of detection of refractive index of a matrix layer.

Chapter 5 investigates the properties of the plasmonic perfect absorbers (PPA) for biosensing. The PPA consists of three layers which include 2-D periodic array of metallic nanodisks, dielectric spacer, and thick metal layer. The excited modes in the PPA system are analyzed. The wavelength of resonance modes can be selected by engineering the geometry of the structure. The first order mode of the PPA provides perfect absorption independent of incident angle and the polarization directions. The first order mode behaves like an LSP mode. The second-order mode of the PPA system is an angular dependent and behaves like SPP mode. The field is analyzed for both modes. The second-order mode gave a high concentrated field along the sensing layer. Hence, this mode is proposed for biosensing applications. Usually, the sensitivity of the nanoparticle-based sensors is computed in the wavelength interrogation scheme, which is an expensive method. Here, we propose a novel method to compute the bulk sensitivity of the PPA system at a fixed wavelength. The sensi-

tivity of the PPA system which is given as 24.6 RIU^{-1} which is comparable to the sensitivity of an SPR sensor (only 1.3 times lesser). The biosensing experiment is also performed for PPA sensor by varying the refractive index of the bulk dielectric medium from $n_d = 1.33$ to $n_d = 1.40$ with a change of $\Delta n_d = 0.01$. Unlike the SPR the reflectivity curve shifts to the right in the angular direction with the change of the refractive index. It is also observed that the FWHM does not change much (only 2°) for the given range of the refractive index ($n_d = 1.33$ to $n_d = 1.40$). Hence, the PPA based biosensors can be used for the long range of wavelength, and also due to the presence of the nanoparticles the localized measurements can be performed. Therefore, the PPA is proposed in this thesis as a suitable candidate for biosensing which provide high sensitivity and can also measure lower concentrations of biomolecules.

As an outlook, the future work may involve the development of the theoretical modeling of the resonance modes for PPA system. As the resonance wavelength of operation is dependent on the geometry of the PPA structure. With the development of the theoretical model, the PPA biosensor can be designed for any wavelength of interest.

List of Publications

- Abdul Aleem Jamali: *Electromagnetic simulation of optical antennas for biosensing.* CEP Seminar, Computational Electronics and Photonics (CEP) Group, University of Kassel, Germany, February 2015 (Oral).

- Abdul Aleem Jamali and Bernd Witzigmann: *Plasmonic Perfect Absorbers for Biosensing.* Plasmonics 9, 1265-1270, 2014.

- Abdul Aleem Jamali and Bernd Witzigmann: *Plasmonic Perfect Absorbers (PPA) for biosensing: a theoretical modal analysis for angular sensitivity.* 5th International Conference on Metamaterials, Photonic Crystals and Plasmonics (META'14), NTU Singapore, 20-23 May, 2014 (Oral).

- Abdul Aleem Jamali; Sebastian Kübler; Nicolas Müglich; Bernd Witzigman and Arno Ehresmann: *Electromagnetic study of magneto-optic surface plasmon resonance effects for biosensing applications.* Proc. SPIE 8774, Optical Sensors 2013, 87741l.1-87741l.12, 2013.

- Abdul Aleem Jamali; Bernd Witzigmann; Rodiga Morarescu; Thomas Baumert; Frank Träger and Frank Hubenthal: *Local near field assisted ablation of fused silica: An experimental and theoretical study.* Appl. Phys. A 110, 743-749, 2013.

- Abdul Aleem Jamali; Sebastian Kübler; Arno Ehresmann and Bernd Witzigmann: *Full-wave electromagnetic simulation of plasmonic perfect absorber (PPA) for biosensing applications.* Center for Interdisciplinary Nanostructure Science and Technology (CINSaT), University of Kassel, Germany, Herbstkolloquium 2013, Nov. 2013(Poster).

- Abdul Aleem Jamali: *Plasmonic Perfect Absorbers (PPAs) for biosensing applications.* CEP Seminar, Computational Electronics and Photonics (CEP) Group, University of Kassel, Germany, November 2013 (Oral).

- Abdul Aleem Jamali; Mufasila Mumthaz Muhammed; Frank Hubenthal and Bernd Witzigmann: *Electromagnetic mode analysis of near field assisted ablation with gold nanoparticles.* International Conference on Fundamental of Laser Assisted Micro-and Nanotechnologies (FLAMN-13), Pushkin, St. Petersburg, Russia, 24-28 June 2013 (Poster).

- Abdul Aleem Jamali; Sebastian Kübler; Arno Ehresmann and Bernd Witzigmann: *Full-wave electromagnetic simulation of plasmonic biosensors.* Center for Interdisciplinary Nanostructure Science and Technology (CINSaT), University of Kassel, Germany, Herbstkolloquium 2013, 28 Feb.-01 March, 2013 (Poster).

- Abdul Aleem Jamali: *Electromagnetic study of magneto-Optical surface plasmon resonance effects for bio-sensing.* CEP Seminar, Computational Electronics and Photonics (CEP) Group, University of Kassel, Germany, January 2013 (Oral).

- A. A. Jamali; S. Maag; L. Englert; B. Witzigmann; T. Baumert; F. Träger and F. Hubenthal: *Parallel nanostructuring of fused silica exploiting the near fields of highly ordered triangular gold nanoparticles.* Center for Interdisciplinary Nanostructure Science and Technology (CINSaT), University of Kassel, Germany, Herbstkolloquium 2011, 20 October, 2011 (Poster).

- Abdul Aleem Jamali: *Magneto-Optical Surface Plasmon Resonance (MOSPR).* CEP Seminar, Computational Electronics and Photonics (CEP) Group, University of Kassel, Germany, December 2011 (Oral).

- A. A. Jamali and R. Marklein: *Design and optimization of ultra-wideband TEM horn antenna for GPR applications.* URSI, IEEE 2011, Istanbul, 13 - 20 August, 2011 (Oral).

- Abdul Aleem Jamali: *Study of Triangular Gold Nanoparticles.* University of Kassel, Germany, August 2011 (Oral).

Bibliography

[1] Tang, D. P.; Yua, R.; Chai, Y. Q.: *Novel immunoassay for carcinoembryonic antigen based on protein A-conjugated immunosensor chip by surface plasmon resonance and cyclic voltammetry.* Bioprocess Biosyst. Eng. 28(5), 315-321 (2006). Link 23, 28

[2] Chung, T.; Lee, S. Y.; Song, E. Y.; Chun, H.; Lee, B.: *Plasmonic nanostructures for nano-scale bio-sensing.* Sensors 11, 10907-10929 (2011). Link 23, 26

[3] Bharadwaj, P.; Deutsch, B.; Novotny, L.: *Optical Antennas.* Optical Society of America, Advances in Optics and Photonics 1, L438-L483 (2009). Link 23

[4] Dorfmller, J.; Vogelgesang, R.; Khunsin, W.; Rockstuhl, C.; Etrichs, C.; Kern, K.: Cubukcu, E.; Capasso, F.: *Plasmonic Nanowire Antennas: Experiment, Simulation, and Theory.* American Chemical Society, Nano Letters 10, L3596-L3603 (2010). Link 15, 23, 24

[5] Stewart, M. E.; Anderton, C. R.; Thompson, L. B.; Maria, J.; Gray, S. K.; Rogers, J. A.; Nuzzo, R. G.: *Nanostructured plasmonic sensors.* Chem. Rev. 108, 494-521 (2008). Link 24

[6] Kretschmann, E.; Raether, H.: *Radiative decay of nonradiative surface plasmons excited by light.* Z. Naturforsch. A 23, 2135-2136 (1968). Link 24, 28, 65

[7] Homola, J.: *Surface plasmon resonance sensors for detection of chemical and biological species.* Chem. Rev. 108, 462-493 (2008). Link 25

[8] Homola, J.; Koudela, I.; Yee, S. S.: *Surface plasmon resonance sensors based on diffrac-*

tion gratings and prism couplers: sensitivity comparison. Sensors and Actuators B: Chemical 54, 16-24 (1999). Link 25

[9] Jensen, T. R.; Malinsky, M. D.; Haynes, C. L.; Duyne, R. P. V.: *Nanosphere Lithography: Tunable Localized Surface Plasmon Resonance Spectra of Silver Nanoparticles.* J. Phys. Chem. B 104 (45), 10549-10556 (2000). Link 25

[10] Mitchell, J. S.; Wu, Y.; Cook, C. J.; Main, L.: *Sensitivity enhancement of surface plasmon resonance biosensing of small molecules.* Anal. Biochem. 343 (1), 125-135 (2005). Link 25

[11] Guo, Y.; Ye, J. Y.; Huang, B.; McNerny, D.; Thomas, Baker, J. R.; Norris, T. B.: *Real-time small molecule binding detection using a label-free photonic crystal biosensor.* Proc. SPIE 7553, (2010). Link 25

[12] Sepúlveda, B.; Calle, A.; Lechuga, L. M.; Armelles, G.: *Magneto-optic sensitivity enhancement in plasmonic sensors.* Bioworld 01, 12-14 (2008). Link 25, 26

[13] Regatos, D.; Sepúlveda, B.; Fariña, D.; Carrascosa, L. G.; Lechuga, L. M.: *Suitable combination of noble/ferromagnetic metal multilayers for enhanced magneto-plasmonic biosensing.* Optics Express 19 (9), 8336-8346 (2011). Link 25, 77, 78

[14] Armelles, G.; González-Díaz, J. B.; García-Martín, A.; García-Martín, J. M.; Ceballada, A.; González, M. U.; Acimovic, S.; Cesario, J.; Quidant, R.; Badenes, G.: *Localized surface plasmon resonance effects on the magneto-optical activity of continuous Au/Co/Au trilayers.* Opt. Express 20(16), 16104-16112 (2008). Link 25

[15] Sepúlveda, B.; González-Díaz, J. B.; García-Martín, A.; Lechuga, L. M.; Armelles, G.: *Plasmon-Induced Magneto-Optical Activity in Nanosized Gold Disks.* Phys. Rev. Lett. 104 (14), 147401.1 - 147401.4 (2010). Link 25

[16] González-Díaz, J. B.; García-Martín, J. M.; García-Martín, A.; Navas, D.; Asenjo, A.; Vázquez, M.; Hernández-Vélez, M.; Armelles, G.: *Plasmon-enhanced magneto-optical*

activity in ferromagnetic membranes. Appl. Phys. Lett. 94(26), 263101.1 - 263101.3 (2009). Link 25

[17] González-Díaz, J. B.; Sepúlveda, B.; García-Martín, A.; Armelles, G.: *Cobalt dependence of the magneto-optical response in magnetoplasmonic nanodisks.* Appl. Phys. Lett. 97(4), 043114.1 - 043114.3 (2010). Link 25

[18] Wei, C. M.; Chen, C. W.; Wang, C. H.; Chen, J. Y.; Chen, Y. C.; Chen, Y. F.: *Magnetically tunable surface plasmon resonance based on a composite consisting of noble metal nanoparticles and a ferromagnetic thin film.* Opt. Lett. 36 (4), 514.1-514.6 (2011). Link 25

[19] Sepúlveda, B.; Calle, A.; Lechunga, L. M.; Armelles, G.: *Highly sensitive detection of biomolecules with the magneto-optic surface-plasmon-resonance sensor.* Optics Lett. 31(8), 1085-1087(2006). Link 25, 52, 67, 77, 80, 81, 96

[20] Kreibig, U.; Zacharias, P.: *Surface plasma resonances in small spherical silver and gold particles.* Z. Phys. A 231 (2), 128-143 (1970). Link 26, 28

[21] Jin, R.; Cao, Y.; Mirkin, C. A.; Kelly, K. L.; Schatz, G. C.; Zheng, J. G.: *Photoinduced Conversion of Silver Nanospheres to Nanoprisms.* Science 294 (5548), 1901-1903 (2001). Link 26

[22] Kim, F.; Song, J. H.; Yang, P.: *Photochemical Synthesis of Gold Nanorods.* J. Am. Chem. Soc. 124 (43), 1431614317 (2002). Link 26

[23] Hao, E.; Kelly, K. L.; Hupp, J. T.; Schatz, G. C.: *Synthesis of Silver Nanodisks Using Polystyrene Mesospheres as Templates.* J. Am. Chem. Soc. 124 (51), 15182-15183 (2002). Link 26

[24] Petroski, J. M.; Wang, Z. L.; Green, T. C.; El-Sayed, M. A.: *Kinetically Controlled Growth and Shape Formation Mechanism of Platinum Nanoparticles.* J. Phys. Chem. B 102, 3316-3320 (1998). Link 26

[25] Millstone, J. E.; Park, S.; Shuford, K. L.; Qin, L.; Schatz, G. C.; Mirkin, C. A.: *Observation of a quadrupole plasmon mode for a colloidal solution of gold nanoprisms.* J. Am. Chem. Soc. 127 (15), 5312.1-5312.3 (2005). Link 26

[26] Hammond, J. L.; Bhalla, N.; Rafiee, S. D.; Extrela, P.: *Localized surface plasmon resonance as a biosensing platform for developing countries.* Biosensors 4, 172-188 (2014). Link 26, 29

[27] Haes, A. J.; Duyne, R. P. V.: *A unified view of propagating and localized surface plasmon resonance biosensors.* Anal. Bioanal. Chem. 379, 920-930(2004). Link 26

[28] Liu, N.; Mesch, M.; Weiss, T.; Hentschel, M.; Giessen, H.: *Infrared perfect absorber and its application as plasmonic sensor.* Nano Lett. 10 (7), 2342-2348 (2010). Link 26, 98

[29] Li, G.; Chen, X.; Li, O.; Shao, C.; Jiang, Y.; Huang, L.; Ni, B.; Hu, W.; Lu, W.: *A novel plasmonic resonance sensor based on an infrared perfect absorber.* J. Phys. D: Appl. Phys. 45 (20), 205102.1-205102.5 (2012). Link 26, 94

[30] Rycenga, M.; Cobley, C. M.; Li, Weiyang, MOran, C. H.; Zhang, Q.; Qin, D.; Xia, Y.: *Controlling the synthesis and assembly of silver nanostructures for plasmonic applications.* Chem. Rev. 111(6), 3669-3712(2011). Link 27

[31] Wood, R. W.: *On a remarkable case of uneven distribution of light in a diffraction grating spectrum.* Philosophical Magazine 4 (21), 396-402 (1902). Link 27

[32] Ritchie, R. H.: *Plasma losses by fast electrons in thin films.* Phys. Rev. 106 (5), 874-881 (1957). Link 27

[33] Powell, C. J.; Swan, B. J.: *Origin of the characteristic electron energy losses in aluminum.* Phys. Rev. 115 (4), 869-875 (1959). Link 27

[34] Ritchie, R. H.; Arakawa, E. T.; Cowan, J. J.; Hamm, R. N.: *Surface-plasmon resonance effect in grating diffraction.* Phys. Rev. Lett. 21 (22), 1530-1533 (1968). Link 28

[35] Otto, A.: *Excitation of nonradiative surface plasma waves in silver by the method of frustrated total reflection.* Z. Phys. A 216, 398-410 (1968). Link 28

[36] Lorenz, L.: *Lysbevaegelsen i og uden for en hal plane lysbôlger belyst kulge.* Vidensk. Selk 6, 1-62 (1898). Link 28

[37] Mie, G.: *Beitrage zur Optik trüber Medien, speziell kolloidaler Metallsungen.* Ann. Phys. 25, 377-445 (1908). Link 28, 54

[38] Fleischmann, M.; Hendra, P. J.; McQuillan, A. J.: *Raman spectra of pyridine adsorbed at a silver electrode.* Chem. Phys. Lett. 26(2), 163-166 (1974). Link 28

[39] Liedberg, B.; Nylander, C.; Lundstroem, I.: *Surface plasmon resonance for gas detection and biosensing.* Sensors and Actuators 4, 299-304 (1983). Link 28

[40] Flangan, M. T.; Pantell, R. H.: *Surface plasmon resonance and immunosensors.* Electron. Lett. 20(23), 968-970 (1984). Link 28

[41] Kooyman, R. P. H.; Kolkman, H.; Gent, J.-v.; Greve, J.: *Surface plasmon resonance immunosensors: sensitivity considerations.* Anal. Chim. Acta 231, 35-45 (1988). Link 28

[42] Wei, J.; Mu. Y.; Song, D.; Fang, X.; Liu, X.; Bu, L.; Zhang, H.; Zhang, G.; DIng, J.; Wang, W.; Jin, Q.; Luo, G.: *A novel sandwich immunosensing method for measuring cardiac troponin I in sera.* Anal. Biochem. 321 (2), 209-216(2003). Link 28

[43] Besselink, G. A: J.; Kooyman, R. P .H.; Os, P. J. H. J.-v; Engbers, G. H. M.; Schasfoort, R. B. M.: *Signal amplification on planar and gel-type sensor surfaces in surface plasmon resonance-based detection of prostate-specific antigen.* Analytical Biochemistry 333(1), 165-173 (2004). Link 28

[44] Chung, J. W.; Kim, S. D.; Bernhardt, R.; Pyun, J. C.: *Application of SPR biosensor for medical diagnostics of human hepatitis B virus (hHBV).* Sensors and Actuators B: Chemical 111-112, 416-422(2005). Link 28

[45] Lee, H. J.; Nedelkov, D.; Corn, R. M.: *Surface plasmon resonance imaging measurements of antibody arrays for the multiplexed detection of low molecular weight protein biomarkers.* Anal. Chem. 78(18), 6504-6510(2006). Link 28

[46] Jahanshahi, P.; Zalnezhad, E.; Sekaran, S. D.; Adikan, F. R. M.: *Rapid Immunoglobulin M-based dengue diagnostic test using surface plasmon resonance biosensor.* Scientific Reports 4(3851), 1-7(2014). Link 28

[47] Kim, D. K.; Kerman, K.; Saito, M.; Sathuluri, R. R.; Endo, T.; Yamamura, S.; Kwon, Y. S.; Tamiya, E.: *Label-free DNA biosensor based on localized surface plasmon resonance coupled with interferometry.* Anal. Chem. 79, 1855-1864 (2007). Link 29

[48] Hiep, H. M.; Nakayama, T.; Saito, M.; Yamamura, S.; Takamura, Y.; Tamiya, E.: *A microfluidic chip based on localized surface plasmon resonance for real-time monitoring of antigen-antibody reactions.* Jpn. J. Appl. Phys. 47, 1337-1341 (2008). Link 29

[49] Haes, A. J.; Hall, W. P.; Chang, L.; Klein, W. L.; van Duyne, R. P.: *A localized surface plasmon resonance biosensor: first steps toward an assay for Alzheimer's disease.* Nano Lett. 4, 1029-1034 (2004). Link 29

[50] Haes, A. J.; Chang, L.; Klein, W. L.; Duyne, R. P. V.: *Detection of a biomarker for Alzheimer's disease from synthetic and clinical samples using a nanoscale optical biosensors.* J. Am. Chem. Soc. 127 (7), 2264-2271 (2005). Link 29

[51] Zhao, Q.; Duan, R.; Quan, Y.; Yang, H.; XI, M.: *A reusable localized surface plasmon resonance biosensor for quantitative detection of serum squamous cell carcinoma antigen in cervical cancer patients based on silver nanoparticles array.* International Journal of Nanomedicine 9(1), 1097-1104 (2014). Link 29

[52] Hirtenfelder, F.; Mollet, J.: *Phased array simulations using Finite Integration Technique.* JINA Conference, 1-6 (2004). Link 16, 30, 60

[53] Maier, S. A.: *Plasmonics: Fundamentals and applications.* Springer, Optische Elektronische Materialien (2007). Link 15, 31, 39, 40, 41, 45, 53, 54

[54] Langenberg, K.-J.: *Theory of Electromagnetic waves.* Manuskript, Universität Kassel, Kassel 2003. (in German) 32, 33

[55] Orfanidis, S. J.: *Electromagnetics waves and antennas.* ECE Department, Rutgers University, 94 Brett Road, Piscataway, NJ 08854-8058 (2014). Link 34, 35, 36

[56] Homola, J.: *Surface plasmon resonance based sensors.* Springer Series on Chemical Sensors and Biosensors 4, (2006). Link 45, 46, 47

[57] Yamamoto, M.: *Surface plasmon resonance (SPR) theory: tutorial.* Rev. Polarogr. 48, 209-37(2002). Link 47, 49

[58] Kooyman, R. P. H.: *Physics of surface plasmon resonance.* Handbook of surface plasmon resonance, edited by Richard B. M. Schasfoort and Anna J. Tudos, The Royal Society of Chemistry, 15-34 (2008). Link 47

[59] Zayats, A.V.; Smolyanninov,I.I: *Near-field photonics: surface plasmon polaritons and localized surface plasmons.* J. Opt. A: Pure Appl. Opt. 5, S1-S35 (2003). Link 48

[60] Riem, W.; Schoenes, J.: *Handbook of magnetic materials.* Ferromagnetic Materials, edited by K. Buschow and E. Wohlfarth, Elsevier Science, Amsterdam 5, 134-155 (1990). Link 50

[61] Qiu, Z. Q.; Bader, S. D.: *Surface magneto-optic Kerr effect.* Review of Scientific Instruments 71 (3), 1243-1255 (2000). Link 50, 81

[62] Ali, M.: *Growth and study of magnetostrictive FeSiBC thin films for devices applications.* Department of Physics and Astronomy, The University of Sheffield, PhD Thesis (1999). Link 51

[63] Villa, E.M.; Martin, A. G.; Cuevas, J.C.: *Extraordinary transverse magneto-optical Kerr effect in a superlens.* Physical Review B 90, 085120.1-085120.5 (2014). Link 51

[64] Regatos, D.; Fariña, D.; Calle, A.; Cebollada, A.; Sepúlveda, B.; Armelles, G.; Lechuga, L. M.: *Suitable combination of noble/ferromagnetic metal multilayers for enhanced magneto-plasmonic biosensing.* J. Appl. Phys. 108, 054502.1-054502.6 (2010). Link 51, 78

[65] Carey, R.; Thomas, B. W. J.: *The theory of the Voigt effect in ferromagnetic materials.* J. Phys. D: Appl. Phys. 7, 2362-2368 (2000). Link 51

[66] Johansen, K.; Arwin, H.; Lundstroem, I.; Liedberg, B.: *Imaging surface plasmon resonance sensor based on multiple wavelengths: sensitivity considerations.* Rev. Sci. Instrum. 71, 3530-3538 (2000). Link 52

[67] Evanoff, D. D.; Chumanov, G.: *Size-controlled synthesis of nanoparticles.2. Measurement of extinction, scattering , and absorption cross sections.* J. Phys. Chem. B 108, 13957-13962 (2004). Link 54

[68] Kvasnička, P.; Hommola, J.: *Optical sensors based on spectroscopy of localized surface plasmons on metallic nanoparticles: sensitivity considerations.* American Vauum Society, Biointerphases 3(3), FD4-FD11 (2008). Link 55

[69] Taflove, A.; Hagness, S. C.: *Computational Electrodynamics: The Finite-Difference Time-Domain Method.* Artech House Publishing, 685 Canton Street, Norwood, MA 02062, USA, (2002). Link 56

[70] Marklein, R.: *The finite integration technique as a general tool to compute acoustic, electromagnetic, elastodynamic, and coupled wave fields.* W.R. Stone (Ed.), Review of Radio Science: 1999-2002 URSI, IEEE Press and John Wiley and Sons, Piscataway and New York, 201244 (2002). Link 56, 60

[71] Marklein, R.: *Numerical methods of electromagnetic field theory I(NFTI).* Lecture notes, NFT-I, Computational Electronics and Photonics (CEP), University of Kassel, Lecture 8 (2009). Link 16, 57, 58

[72] Yang, F.; Samii, Y. R.: *Electromagnetic Band Gap Structures in Antenna Engineering.* Cambridge University Press, New York, (2009). Link 59, 61, 62, 63

[73] Johnson, S.G.: *Notes on Perfectly Matched Layer (PMLs).* Lecture notes, Department of Mathematics, Massachusetts Institute of Technology, (2010). Link 61

[74] Liu, C.; Liu, Q.; Hu, X.: *SPR phase detection for measuring the thickness of thin metal films.* Optics Express 22 (7), 7574-7580 (2014). Link 70

[75] Lecaruyer, P.; Canva, M.; Rolland, J.: *Metallic film optimization in a surface plasmon resonance biosensor by the extended Rouard method.* Optical Society of America, Applied Optics 46(12), 2361-2369 (2007). Link 70

[76] Maharana, P. K.; Jha, R.; Padhy, P.: *On the electric field enhancement and performance of SPR gas sensor based on graphene for visible and near infrared.* Sens. and Actuat. B 207, 117-122 (2015). Link 76

[77] Raether, H.: *Surface plasmons on smooth and rough surfaces and on gratings.* Springer Tracts in Modern Physics 111, Springer-Verlag Berlin (1988). Link 77, 79

[78] Yee, S. S.; Homola, J.; Gauglitz, G.: *Surface plasmon resonance sensors: review.* Sensors and Actuators B: Chemical 54, 3-15 (1999). Link 77

[79] Clavero, C.; Yang, K.; Skuzy, J. R.; Lukaszew, R. A.: *Magnetic field modulation of intense surface plasmon polaritons.* Optical Society of America 18, L7743-L7552 (2010). Link 78, 85

[80] Hickernell, R. K.; Sarid, D.: *Long-range surface magnetoplasmons in thin nickel films.* Opt. Lett. 12(8), 570-572 (1987). Link 78

[81] Ferguson, P. E.; Stafsudd, O. M.; Wallis, R. F.: *Enhancement of transverse Kerr magneto-optic effect by surface magnetoplasma waves.* Physica B+C 89, 91-94 (1977). Link 78, 79

[82] Johnson, P.B.; Christy, R. W.: *Optical constants of the noble metals.* Phys. Rev. B 6(12), 4370-4379 (1972). Link 79

[83] Hermann, C.; Kosobukin, V. A.; Lampel, G.; Peretti, J.; Safarov, V. I.; Bertrand, P.: *Surface-enhanced magneto-optics in metallic multilayer films.* Phys. Rev. B 64 (23), 235422 (2001). Link 79

[84] González-Díaz, J. B.; García-Martín, A.; Armelles, G.; García-Martín, J. M.; Clavero, C.; Cebollada, R. A.; Lukaszew, R. A.; Skuza, J. R.; Kumah, D. P.; Clarke, R.: *Surface magnetoplasmon nonreciprocity effects in noble-metal/ferromagnetic heterostructures.* Phys. Rev. B 76 (15), 153402 (2007). Link 79

[85] Kämpf, K.; Kübler, S.; Herberg, F. W.; Ehresmann, A.: *Magneto-optic surface plasmon resonance optimum layers: simulations for biological relevant refractive index changes.* J. Appl. Phys. 112, 034505.1-034505.5 (2012). Link 79, 84

[86] Jamali, A. A.; Kübler, S.; Müglich, N.; Witzigmann, B.; Ehresmann, A.: *Electromagnetic study of magneto-optic surface plasmon resonance effects for biosensing applications.* Proc. of SPIE 8774, 87741l.1-87741l.12(2013). Link 17, 18, 78, 80, 82, 83, 84, 87, 88, 90, 91

[87] Smith, D. R.; Vier, D. C.; Koschny, T.; Soukoulis, C. M.: *Electromagnetic parameter retrieval from inhomogeneous metamaterials.* Phys. Rev. E 71, 036617.1-036617.11(2005). Link 86

[88] Cattoni, A.; Ghenuche, P.; Gosnet, A. M. H.; Decanini, D.; Chen, J.; Pelouard, J. L.; Collin, S.: $\lambda^3/1000$ *plasmonic nanocavities for biosensing fabricated by soft UV nanoimprint lithography.* Nano Lett. 11, 35573563 (2011). Link 94, 100

[89] Liu, N.; Weiss, T.; Mesch, M.; Langguth, L.; Eigenthaler, U.; Hirscher, M.; Sönnichsen, C.; Giessen, H.: *Planar metamaterial analogue of electromagnetically induced transparency for plasmonic sensing.* Nano Lett. 10, 11031107 (2009). Link 94

[90] Becker, J.; Trügler, A.; Jakab, A.; Hohenester, U.; Sönnichsen, C.: *The optimal aspect ratio of gold nanorods for plasmonic bio-sensing.* Plasmon. 5, 161167 (2010). Link 94

[91] Jamali, A. A.; Witzigmann, B.: *Plasmonic Perfect Absorbers for Biosensing.* Plasmonics 9(6), 1265-1270 (2014). Link 18, 19, 94, 95, 97, 98, 99, 102, 103, 104

[92] Agio, M.; Alù, A: *Optical Antennas.* Cambridge University Press, 285-289(2013). Link 98, 100

[93] Svedendahl, M.; Chen, S.; Dmitriev, A.; Käll, M.: *Refractometric sensing using propagating versus localized surface plasmons: A direct comparison.* Nano Lett. 9, 4428-4433 (2009). Link 103